International Journal of Quantum Foundations **12** (2026) 497-589

Original Paper

From Brownian Motion to Black Holes: Chronoscalar Transport via the Hessian Flip

Calvin A. Grant

Chronoscalar Dynamics, USA
E-mail: lotdf9977@gmail.com

Received: 5 January 2026 / Accepted: 20 January 2026 / Published: 24 January 2026

Abstract: We develop a single covariant transport principle that spans nonrelativistic Brownian motion, relativistic dissipative hydrodynamics, heavy–ion anisotropic flow, and black–hole horizon dynamics [1–6]. The framework is built on a physical scalar ordering field $T(x^\mu)$ whose gradient selects preferred directions and whose Hessian governs admissible microscopic support [7–10]. The central mechanism—the *Hessian flip*—maps negative–curvature directions of T (microscopic stabilization corridors) into enhanced macroscopic dissipation channels [11–14]. This yields a covariant anisotropic constitutive law that is hyperbolic, entropy producing, and regularizing, providing a geometric closure for Navier–Stokes–type evolution and its membrane–paradigm dual [15–19]. The same ordering geometry deforms the path–integral measure, producing a "yaw" of propagator weights and an explicit derivation of Tsallis non–extensive statistics ($q > 1$) from diffusion on a curved T background [20–24]. We connect these structures to quantitative heavy–ion observables (CMS $v_2(p_T)$ and ALICE $R_{\mathrm{FB}}(p_T)$) [25–29] and formulate theorem–level horizon results, including a Regular Core Theorem and a Sub–Extremal Spin Theorem [30–34].

Keywords: Chronoscalar Field Theory, Heissan Flip, Black Hole Regularity

1. INTRODUCTION

Irreversible transport, persistent anisotropy, and long–range coherence appear across physical systems that otherwise share no common scale, constituents, or effective

description: a micron–scale tracer undergoing Brownian motion [1,2], a quark–gluon plasma exhibiting sustained anisotropic flow [3–6], a galactic disk maintaining flat rotation curves over decades in radius [7–9], and a black–hole horizon behaving as a viscous, dissipative surface [10–13]. Standard theoretical frameworks treat these phenomena as fundamentally distinct. Brownian motion is modeled as stochastic forcing around isotropic equilibrium [1,2,14]. Relativistic hydrodynamics is closed through isotropic constitutive relations whose parabolic structure produces well–known causality and regularity pathologies [15–18]. Galactic dynamics are reconciled phenomenologically through additional mass components or modified force laws [7,19–21]. Horizon thermodynamics is treated as an analogy or semiclassical limit, introducing entropy, temperature, and the information paradox as emergent constructs [10–13,22–24]. Despite their technical success, these approaches share no common organizing principle.

What recurs empirically across all of these regimes, however, is not merely dissipation or equilibration, but *asymmetric irreversibility*: transport; by "transport" we mean the manner in which motion, influence, and ordering propagate through a system as it evolves in time. In ordinary systems this propagation is isotropic and short-ranged, but in the chronoscalar framework it becomes directionally biased: evolution preferentially proceeds along specific admissible directions set by the ordering field, producing correlations that persist far beyond what would be expected from local interactions or naive causal estimates [3–6,25], statistics that are robustly non–Gaussian [26–29], and harmonic structure that survives averaging over microscopic detail and system size [30–32]. These features are not incidental. They point to a shared constraint that is geometric rather than dynamical, and global rather than emergent.

In this work we identify that constraint as a physically real, asymmetric scalar ordering field $T(x^\mu)$ [42]. Unlike conventional treatments in which time is a passive parameter coordinating evolution [33], the chronoscalar field is an active geometric structure whose gradient ∇T partitions admissible motion in spacetime. The asymmetry of T is primordial: it is not imposed by boundary conditions, entropy production, or coarse graining [14,34], but exists prior to dynamics. Any physical process that unfolds in time must do so along trajectories that are compatible with this ordering geometry. Irreversibility is therefore not a consequence of microscopic randomness; it is the macroscopic expression of admissibility under an asymmetric temporal manifold.

Within this framework, forces do not generate structure. Instead, structure emerges because admissible trajectories are geometrically filtered. At small scales this filtering appears as biased diffusion and non–extensive statistics [26–29]. At intermediate scales it produces anisotropic transport, nematic ordering, and persistent collective flow [3–6,25,35]. At galactic scales it manifests as phase–locked orbital coherence and flat rotation curves [7–9,30,31]. At horizon scales it enforces viscous behavior, finite invariants, and limits on extremal spin [10–13,36–38]. These are not separate mechanisms but

scale–dependent projections of the same chronoscalar geometry.

The decisive object governing these projections is the curvature structure of the ordering field

T through its Hessian. The sign here is not a statement about "negative time." It is the sign of the projected second variation of

T that determines whether nearby admissible continuations focus or defocus when displaced transversely to the ordering advance. In concave sectors of the projected Hessian, neighboring continuations are geometrically focused into a common channel: dispersion is suppressed because offsets are pulled back toward the same admissible track. In convex sectors, neighboring continuations separate and leak into additional degrees of freedom, enabling enhanced relaxation and dissipation along those directions [39–41]. Crucially, this curvature does not act uniformly across scale. A geometric sign inversion—the *Hessian flip*—maps stabilization directions at microscopic scales into dissipation channels at macroscopic scales. This flip is not a dynamical instability and does not introduce new degrees of freedom; it is a projection of an existing ordering structure into orthogonal admissible subspaces as phase accumulation saturates.

A direct consequence of this geometry is the existence of massive, non–propagating standing modes in the longitudinal sector of T. These modes encode a global registry and remain phase-locked across the system. Energetically, they represent a bound reservoir: energy is concentrated and held in constrained form rather than transported or radiated, becoming observable only when coupling or perturbation allows release. Observable dynamics arise only through transverse readout channels activated at Hessian sign reversal. Because corridor occupation is quadratic in amplitude, this projection produces mandatory harmonic doubling, yielding fixed spectral ratios that are independent of scale, composition, or environment [30–32]. The same mechanism underlies the appearance of Tsallis–type heavy tails in diffusion [26–29], persistent v_2 harmonics in collider systems [3–6], and the universal 2:1 frequency structure observed in galactic rotation–curve residuals.

Gravity, in this view, is not a force transmitted by exchange particles nor a curvature of spacetime sourced by stress–energy [19,20]. It is the macroscopic manifestation of admissible motion under chronoscalar ordering. The longitudinal standing sector stores global geometric registry, while transverse excitations act as photon–like phase carriers that transmit orientation updates without transporting the stored data. Apparent attraction, collectivity, and dissipation are all readouts of this geometry rather than primary causes. In the framework, what is conventionally described as attraction is not a primitive interaction. It is the observational read-out of a standing ordering structure. Before any apparent infall or convergence occurs, the system establishes a global registry: a phase-locked standing configuration that defines which continuations remain admissible. Motion then appears to "fall inward" only because transverse continuations are progressively excluded, not because

a force pulls trajectories together. Infall from Hessian mechanics (CFT narrative)

In Chronoscalar Field Theory, infall does not begin with a pull or an acceleration. It begins with ordering advance. The ordering field

T advances all configurations forward, and at each step that advance must be resolved into admissible continuations. These continuations are not arbitrary: they are weighted and filtered by the local curvature structure of

T, encoded in its Hessian.

As mass–energy accumulates in a region, the ordering field does not steepen uniformly. Instead, its second variation develops structure: certain transverse directions become concave under projection. This concavity does not reverse time or halt motion. It changes how nearby admissible continuations respond to displacement. In concave sectors of the projected Hessian, small transverse deviations are not amplified; they are geometrically redirected back toward the same continuation channel.

This is the onset of infall.

What appears macroscopically as inward motion is, at the microscopic level, a progressive loss of transverse admissibility. Trajectories are not pulled inward; rather, the ordering geometry ceases to support lateral continuation. Each step forward in

T offers fewer viable directions than the step before. Motion persists, but it persists only along the remaining longitudinally compatible channels.

As this filtering repeats, configurations appear to converge. Distances shrink not because space is contracting locally, but because the space of admissible futures is collapsing onto a lower-dimensional set. Infall is therefore the observational signature of Hessian focusing: a regime in which the projected curvature of the ordering field causes admissible continuations to align.

Crucially, this process is inherently standing. The concave Hessian sectors establish a phase-locked registry that spans the region. Once established, this registry does not propagate or radiate; it constrains. Energy entering the region populates this standing structure, increasing its stiffness, but does not change the fact that infall is governed by admissibility rather than force.

When the curvature structure flips sign in certain projections—the Hessian flip—this same geometry that previously suppressed dispersion now enables controlled leakage and dissipation. But infall itself begins earlier, at the moment transverse continuations cease to be supported. There is no singular pull, only a narrowing of what futures remain allowed.

Chronoscalar Field Theory therefore replaces a fragmented landscape of force laws, statistical assumptions, and phenomenological fixes with a single, scale–independent ordering principle. Brownian motion, relativistic flow, galactic dynamics, and horizon physics are unified not by analogy but by shared geometry. By treating time itself as an asymmetric physical field whose curvature governs admissibility, the theory provides a common origin for irreversible transport, non–extensive statistics, harmonic locking,

and gravitational phenomenology across the full span of physical scales. Standing is not a special dynamical state but the fundamental condition imposed by global ordering: configurations persist by maintaining phase coherence under temporal advance, and all observed motion, radiation, and collapse arise from how this standing structure is populated, stressed, or partially released.

2. FUNDAMENTAL FRAMEWORK

2.1. Directional Ordering and the Chronoscalar Manifold

Temporal ordering in Chronoscalar Field Theory is not represented by a single parameter nor by a sequence of discrete intervals. The directional component T_4 does not advance in ticks, steps, or gaps, and it should not be interpreted as a clock-like variable that races ahead of physical processes. Instead, T_4 represents a continuously taut ordering advance: an irreducible, ever-present forward constraint under which all configurations are carried. If an analogy is helpful, it is not that of a runner covering distance in stages, but of a string held under near-infinite tension, along which ordering is transmitted without slack. There is no waiting between advances, no meaningful subdivision of the march itself, and no physical process that can overtake or lag the advance as such.

T_4 originates at the asymmetric Machian displacement of the ordering manifold from $T = 0$, initiating the irreducible advance by which admissible configurations first become serially realized. This advance expanded at an effective primordial rate ($\sim 10^6 c$), permitting horizon-scale separation without superluminal transport, as required by the large-angle coherence of the cosmic microwave background. The residual CMB temperature instead reflects subsequent accumulation in $T_{\rm scalar}$, arising from ordering dissipation along long chronoscalar channels: diffusive leakage of ordering drives near-homogeneity below the corridor support scale, such that perturbation amplitudes are exponentially suppressed according to $A_k(\Delta T_4) = A_k(0)\exp[-k^2\ell_D^2]$, consistent with the observed damping tail and diffusion-dominated thermal imprint of the CMB rather than kinematic reheating. The directional component T_4 therefore represents the forward ordering advance in its most primitive form: the condition that admissible futures exist at all. This advance is not generated by matter, radiation, or interaction; rather, it is the organizing principle that renders interaction meaningful. Physical processes do not drive T_4 forward.Physical processes do not drive T_4 forward. Instead, they are resolved into $T_{\rm scalar}$, where interaction, persistence, and dissipation are accumulated as ordering content under the continuous advance imposed by T_4.

Accumulated ordering is encoded in a scalar field $T_{\rm scalar}$, which records the history of interaction and persistence under advance. By construction, $T_{\rm scalar}$ necessarily lags

T_4. The scalar content can never catch the advance without pathological loss of causality or irreversibility. Standing coherence therefore exists only under permanent mismatch: persistence is maintained not by stasis, but by continuous renewal under advance. The apparent stability of structures reflects sustained phase coherence under this condition, not equilibrium with respect to time.

The full ordering structure is represented by the chronoscalar manifold T_{mani}, which encodes both the directional flow and the accumulated registry. Interactions act on this manifold not by halting or segmenting advance, but by loading admissible trajectories and biasing how ordering is resolved locally. Electromagnetic and gravitating interactions contribute to this loading as feedback: they reshape admissibility, rotate local ordering yaw, and modulate persistence, without generating the advance itself.

The local ordering axis is defined by the normalized gradient of the chronoscalar field,

$$n_\mu \equiv \frac{\nabla_\mu T}{\sqrt{\nabla_\alpha T \, \nabla^\alpha T}} \,. \tag{1}$$

This unit covector defines the instantaneous direction of ordering advance with respect to which admissible continuation, persistence, and subsequent geometric projection are resolved.

2.2. Of Space and Standing as Accumulated Persistence

Space is not a primitive arena in Chronoscalar Field Theory. It emerges as the accumulated record of ordering persistence transverse to the direction of advance. As configurations are carried forward by T_4, infinitesimal continuations resolve into components aligned with the ordering axis and components transverse to it. Aligned continuation contributes solely to advance and leaves no persistent residue. Transverse continuation cannot be reabsorbed into pure advance and therefore accumulates, generating separative structure.

Standing coherence arises simultaneously with this accumulation. It is the condition under which transverse persistence remains phase-registered across the system despite continuous advance. Standing is not an equilibrium or frozen configuration, but a dynamically maintained registry sustained under ongoing ordering flow. All observable structure—spatial extent, anisotropy, circulation, and eventual relaxation—arises from how admissible transverse components are supported, filtered, or released under this process.

This separation between advance and persistence is made precise by introducing the transverse projector. Let the ordering axis be defined by the unit covector $n_\mu \propto \nabla_\mu T$. The squared infinitesimal spatial separation is then defined as

$$ds^2_{\mathrm{space}} = P^{\perp}_{\mu\nu}\, dx^\mu dx^\nu, \qquad P^{\perp}_{\mu\nu} = g_{\mu\nu} - n_\mu n_\nu. \tag{2}$$

Here $P^{\perp}_{\mu\nu}$ projects infinitesimal continuation onto directions transverse to the ordering axis. The quantity ds^2_{space} therefore measures accumulated persistence under temporal advance

rather than instantaneous spatial distance. What is identified as "space" is precisely what remains after the advance direction has been factored out.

The geometric meaning of this construction is most transparent in its dynamic trigonometric form. For an admissible continuation making an angle θ with the ordering axis, the decomposition implies

$$ds^2_{\text{space}} \propto \sin^2\theta, \qquad ds^2_{\parallel} \propto \cos^2\theta. \tag{3}$$

The anisotropic and isotropic components are thus not labels but continuously reweighted geometric projections. Because interaction loading, stress, and transport rotate the local ordering axis, the angle θ—and hence the partition between advance and persistence—is dynamically evolving. Spatial geometry is therefore not fixed; it is the cumulative outcome of this evolving projection under sustained advance.

Standing corresponds to the maintenance of coherent transverse registry throughout this evolution. Motion, radiation, dissipation, and collapse are not the creation or destruction of standing itself, but changes in how the transverse sector is populated, redistributed, or released. Standing is preserved so long as transverse persistence remains phase-registered across the system, even as its detailed expression evolves.

Within this framework, early baryonic densities and subsequent galaxy formation are embedded within the long chronoscalar channels established during the primordial T_4 advance. They do not determine the channel reach or coherence scale; instead, they populate and modulate structures that are already geometrically fixed by admissible separation. The effective separation rate of order $10^{16}c$ sets the geometric reach of accumulated persistence, establishing horizon-spanning channels with standing-wave support. Baryons appear later, accumulating in T_{scalar} along these channels and reinforcing coherence locally through gravitational and acoustic feedback.

Galaxy formation is therefore an interposed readout process rather than the generator of large-scale structure. Early baryonic density contrasts modulate channel occupancy and mode amplitudes but do not erase the primordial near-homogeneity established by transverse persistence and diffusion. This ordering explains why large-angle CMB coherence survives despite later structure formation, why acoustic peaks reflect standing modes of pre-existing channels rather than late-time causal contact, and why galaxy filaments align with corridors instead of creating them.

In this way, the projection-based definition of space, the $10^{16}c$ effective separation scale, the diffusion-dominated thermal imprint of the CMB, and the observed architecture of cosmic structure are unified within a single geometric and dynamical framework, without invoking inflationary causality or introducing space as a primitive construct.

2.3. Interaction Load, the Hessian of Ordering, and Admissible Reweighting

The ordering advance defined by T_4 is not generated by interaction, but interaction profoundly affects how admissible continuation is resolved. Electromagnetic radiation and gravitating interactions act as sustained sources of ordering load, imposed not on the ordering advance itself but on the ensemble of admissible trajectories evolving under it. This load alters the local stability of continuation directions and therefore the maintenance of standing registry.

The geometric object that encodes this effect is the Hessian of the ordering field, which measures how the ordering gradient varies across neighboring continuations. The Hessian does not represent curvature of spacetime; it represents curvature of ordering admissibility. Through it, interaction load feeds back into the angular resolution of continuation, dynamically reweighting which directions can persist coherently under advance.

The Hessian of the ordering field is defined as

$$H_{\mu\nu} \equiv \nabla_\mu \nabla_\nu T. \tag{4}$$

The Hessian governs how the local ordering axis n_μ changes across infinitesimal displacements. When projected transverse to the ordering direction, it determines whether nearby continuations converge into registry or separate away from it.

To isolate this effect, we introduce the projected Hessian

$$H^{\perp}_{\mu\nu} \equiv P^{\perp}{}_{\mu}{}^{\alpha}\, P^{\perp}{}_{\nu}{}^{\beta}\, H_{\alpha\beta}, \tag{5}$$

which acts purely on the transverse sector responsible for spatial persistence.

The trigonometric meaning of this construction follows directly from the decomposition introduced in Block II. For a transverse offset ξ^μ satisfying $n_\mu \xi^\mu = 0$, the second variation

$$\delta^2 T = \xi^\mu \xi^\nu H^{\perp}_{\mu\nu} \tag{6}$$

determines how the local projection angle θ evolves under continued advance.

If $\delta^2 T < 0$, transverse deviations are geometrically steered back into phase coherence: admissible continuations align, and standing registry stiffens. If $\delta^2 T > 0$, transverse deviations defocus: admissible continuations separate, and excess ordering is released through relaxation. This sign structure does not describe attraction or repulsion in a force sense; it describes whether transverse components weighted by $\sin^2\theta$ are supported or filtered under continued advance.

Electromagnetic radiation and gravitating interactions enter this framework as sources of sustained ordering load. They increase the rate at which admissible trajectories are sampled and stressed, amplifying the effective magnitude of the projected Hessian without generating ordering advance themselves. In regions of intense radiative or gravitating interaction, the ordering axis rotates more rapidly, and the angular partition between longitudinal and transverse continuation evolves accordingly. What appears

macroscopically as heating, compression, or gravitating influence is, at the ordering level, the cumulative effect of repeated interaction-driven reweighting of admissible directions.

As interaction load accumulates, the projected Hessian generically develops strong eigenvalue contrast across the transverse sector. This prepares the conditions for a qualitative reorganization of admissible continuation, in which directions that previously supported transverse persistence become channels for relaxation. This reorganization—the Hessian flip—is not a new force or instability, but a geometric consequence of sustained ordering load acting on standing registry.

2.4. Chronoscalar Ordering, Persistence, and the Admissibility Functional **Mini Glossary**

(for quick reading). For accessibility, we list the primary chronoscalar terms used in Secs. II.D–II.E:

- *Ordering field* $T(x^\mu)$*:* a physical scalar field encoding temporal admissibility; it is not a coordinate time label but a geometric ordering structure.
- *Ordering axis* n^μ*:* the normalized gradient direction of T, defining the local advance direction: $n^\mu \propto \nabla^\mu T$.
- *Persistence / standing:* the maintenance of phase-registered transverse structure under ordering advance; "standing" is not equilibrium but sustained registry under ongoing advance.
- *Admissibility:* the rule that not all histories/trajectories are equally realizable; histories are *geometrically filtered* by T through a weighting functional.
- *Admissibility functional* $A[\gamma]$*:* the path-weight assigned to a history γ that encodes ordering cost; dominant macroscopic behavior is controlled by the highest-admissibility corridor bundle.
- *Hessian* $H_{\mu\nu} = \nabla_\mu \nabla_\nu T$*:* the curvature structure of ordering (not spacetime curvature), governing focusing/defocusing of nearby admissible continuations.
- *Projected Hessian* $H^{\perp}_{\mu\nu}$*:* the spatial/transverse restriction of $H_{\mu\nu}$ onto the persistence sector orthogonal to the ordering axis.
- *Hessian flip:* the scale-projection inversion in which curvature directions that stabilize microscopic admissible corridors act as enhanced macroscopic dissipation channels after accumulation/loading.
- *Standing registry:* the longitudinally phase-locked corridor structure (non-propagating) that stores global coherence and fixes nodal/harmonic constraints in macroscopic readouts.

These definitions are intended as reading aids only; the formal definitions and operators used in the theory are given below.

The central postulate of Chronoscalar Field Theory (CFT) is that time is not a passive coordinate but a physically real, asymmetric scalar ordering field $T(x^\mu)$ whose gradient defines persistence, admissibility, and thermodynamic directionality [42]. This asymmetry is not imposed by boundary conditions, entropy gradients, or coarse graining; it is required for the existence of macroscopic structure in any system that exists in time, even momentarily [14,43]. In a time-symmetric manifold, microscopic reversibility prevents the formation of long-lived ordered structures without continual fine tuning [14,44]. Persistence itself therefore demands a scalar ordering bias that distinguishes admissible from inadmissible histories [42,45].

In CFT, this bias is encoded in the chronoscalar gradient $\nabla_\mu T$, which selects preferred directions in phase space while remaining compatible with local relativistic kinematics [15,33,46]. The ordering field does not act as a force and does not inject energy into the system. Instead, it geometrically filters trajectories by weighting their admissibility. Histories aligned with ∇T accumulate phase coherently and persist, while those that attempt to explore directions of unfavorable ordering curvature decohere or relax [42,47]. Thermodynamic irreversibility is therefore reinterpreted not as a statistical tendency toward disorder, but as a geometric restriction on which trajectories remain admissible over extended durations [14,45,48].

Although physical motion unfolds in a $(3+1)$-dimensional spacetime, chronoscalar ordering induces an effective dimensional reduction in admissible transport [42,49]. At fixed radius, energy scale, or coarse-graining resolution, admissible motion is confined to a foliated manifold whose dominant ordering directions span a two-dimensional structure: a longitudinal direction aligned with ∇T and a transverse plane orthogonal to it. This reduction is not a projection artifact or a kinematic approximation. It is a direct consequence of persistence constraints [42,50]. Ordered motion must remain phase-coherent along ∇T, while fluctuations transverse to this direction incur increasing admissibility cost as curvature accumulates [39–41]. The resulting hierarchy naturally produces rank-1 longitudinal structure and rank-3 transverse structure in macroscopic response, a pattern that will recur throughout the phenomenology developed below [30–32,42].

Chronoscalar Field Theory is defined by a variational principle in which the ordering field $T(x^\mu)$ is physical. Transport closure and anisotropic stress are not imposed phenomenologically; they follow from an action built from $\nabla_\mu T$ and the projected Hessian geometry. We write

$$S_{\mathrm{CFT}}^{\mathrm{bulk}} = \int_{\mathcal{M}} \mathcal{L}_{\mathrm{CFT}} \sqrt{-g}\, d^4x, \tag{7}$$

with

$$\mathcal{L}_{\rm CFT} = -\Lambda_T - \frac{\alpha}{2}\,\nabla_\mu T \nabla^\mu T - \frac{\beta}{2}\,H_\perp^{\mu\nu} F_{\mu\nu}(H_T), \tag{8}$$

where $H_{\mu\nu} = \nabla_\mu \nabla_\nu T$, $H_\perp^{\mu\nu} = \Delta^\mu{}_\alpha \Delta^\nu{}_\beta H^{\alpha\beta}$, and $F^{\mu\nu}(H_T)$ is the Hessian-flip operator defined from the eigenstructure of $H_\perp^{\mu\nu}$. The field equations and constitutive anisotropic stresses used throughout follow from variation of $S_{\rm CFT}^{\rm bulk}$.

The chronoscalar manifold exists because persistence is observed. Any system that exhibits memory, relaxation, bounded response, or stable bound states implicitly defines an ordering geometry that filters trajectories [14,45]. Conventional theories treat this structure as emergent or statistical; CFT elevates it to a fundamental geometric object [42]. At microscopic scales, the ordering geometry manifests as constrained Brownian motion and non-Gaussian diffusion [1,2,26–29]. At mesoscopic scales, it produces anisotropic transport and nematic response [3–6,25]. At astrophysical scales, it appears as standing registries, bounded rotation curves, and phase-locked coherence [7–9,30–32]. The ordering field itself does not change across scales; only the admissible corridor structure and the manner of readout differ [42].

These considerations motivate the definition of a chronoscalar admissibility functional. For any trajectory γ connecting spacetime events x_1^μ and x_2^μ, we define the admissibility weight

$$\mathcal{A}[\gamma] \;\equiv\; \exp\!\left(-\int_\gamma \mathcal{L}_{\rm adm}(\nabla_\mu T,\, H_{\mu\nu}(T),\, u^\mu)\; ds\right), \tag{9}$$

where u^μ is the tangent to the trajectory, $H_{\mu\nu}(T) = \nabla_\mu \nabla_\nu T$ is the chronoscalar Hessian, and $\mathcal{L}_{\rm adm}$ is a positive-definite local admissibility density [39–41,42]. Trajectories that align with favorable ordering directions minimize $\mathcal{L}_{\rm adm}$ and dominate long-time behavior, while trajectories that probe unfavorable curvature are exponentially suppressed [26–29,39].

Macroscopic observables are determined not by force balance but by extremal or dominant contributions to this admissibility functional [42,51]. Standing modes arise when longitudinal admissibility saturates globally, while transverse response is activated when Hessian curvature changes sign and redistributes admissible support [30–32,42]. In this way, persistence, irreversibility, anisotropy, and large-scale structure emerge as geometric consequences of an asymmetric ordering field, rather than as independent dynamical assumptions [42].

All dynamical responses in CFT are generated by a single admissibility functional, which encodes how ordering curvature, phase, and geometry weight the ensemble of allowed histories [42]. The most general form required for macroscopic systems is

$$A(\chi,\mu,t) = \int_{L_M(T)} \Bigg[(\nabla\kappa\cdot\hat{n})_{\parallel} + \sum_{n=1}^{N} \Big(a_n \cos(n\Delta\phi_{\perp}) + b_n \sin(n\Delta\phi_{\perp}) \Big) (\nabla\kappa\cdot\hat{\chi})_{\perp} \big(1+\beta H_{\text{flip}}(\tilde{H}^{\perp})\big) \Bigg] d\tau \times \left(1-\frac{1}{\sqrt{\mu}}\right) \big(1+\gamma_{\parallel}(t)\big)\,(1+\gamma_{\perp}(t))\,. \tag{10}$$

This functional has the following explicit components:

- $L_M(T)$ is the Machian admissibility path bundle defined by the chronoscalar field, restricting integration to histories compatible with persistence [42].
- $(\nabla\kappa\cdot\hat{n})_{\parallel}$ is the longitudinal ordering response, aligned with ∇T, corresponding to low-cost, gravity-like transport [7–9,42].
- $(\nabla\kappa\cdot\hat{\chi})_{\perp}$ represents transverse ordering curvature, activated by rotation, torsion, or nematic misalignment [25,35,42].
- The cosine–sine expansion in $\Delta\phi_{\perp}$ resolves transverse admissibility into phase-dependent modes. These modes generate standing waves, spiral structure, and nodal locking [30–32,42].
- $H_{\text{flip}}(\tilde{H}^{\perp})$ is the Hessian-flip operator encoding the transition between stabilizing and destabilizing curvature sectors [39–41,42].
- β is a universal dimensionless amplitude set by residual chronoscalar tension [42].
- μ is the mass-scale coupling parameter, ensuring decoupling in the $\mu \to \infty$ limit [42].
- $\gamma_{\parallel}(t)$ and $\gamma_{\perp}(t)$ encode slow temporal modulation of ordering response along longitudinal and transverse directions [42].

2.5. Rank Decomposition and Physical Interpretation

The admissibility functional enforces a kinematically necessary decomposition of response into a rank-1 longitudinal subspace and a rank-3 transverse subspace [43]. This decomposition is not assumed; it follows directly from the geometry of $T(x^{\mu})$ and the structure of $A(\chi,\mu,t)$ [44].

All subsequent results — Brownian non-Gaussianity, nematic ordering, galactic rotation curves, Penrose transitions, and standing-wave locking — are consequences of how this functional is evaluated under different symmetry and curvature regimes [45–48].

The remainder of the paper explores these regimes in increasing scale, without introducing additional dynamical assumptions [43].

Crucially, the chronoscalar structure is *not* an "effective" feature that turns on above some ultraviolet cutoff, and it is *not* a renormalization story [49]. In CFT the ordering field is primordial: it is the physical asymmetry that makes *time* a directed, non-exchangeable ingredient of reality rather than a passive coordinate label [43,50]. The claim is stronger than "systems remember over long durations" and stronger than "boundary conditions select an arrow." The ordering asymmetry is not a late-time convenience; it is the minimal condition for *existence in time at all* [51]. A configuration that cannot be ordered cannot persist even momentarily as a macroscopic object, because without a directed ordering there is no admissible way to define stable succession, no coherent accumulation, and no lawful distinction between "before" and "after" inside the dynamics [43,52].

The physical "scale" of the manifold must therefore be stated carefully. The ultraviolet unit may be used as a *reference*—a conventional yardstick for extremal fineness—but in CFT it is not invoked as a cutoff where the theory changes character [53]. What is fundamental is not a hard ultraviolet wall; what is fundamental is that the ordering field induces a *mesh* of admissible cells [43]: regions of phase space in which trajectories are permitted to remain coherent and regions in which they are forced to decorrelate [54]. The fineness of this mesh can be discussed in ultraviolet-referenced language if one wants a concrete measure of resolution, but the operative concept is not "short distance physics"; it is *admissibility* [43]. The ordering field supplies an orientation and a bias in the measure over histories [55]. That bias is present wherever there is time, regardless of the microscope one uses to look [43]. The universe does not "become ordered" only when one zooms out; the universe is ordered, and macroscopic structure is what happens when that ordering can be *held* [56].

This is why the same chronoscalar geometry appears in settings that mainstream physics keeps separate: diffusion, relaxation, nematic alignment, disks and arms, compact-object anchoring, and horizon-regulated interiors [45–48,57]. These are not different theories stitched together. They are different *expressions* of the same ordering, determined by how much a given system can store as coherent phase rather than dissipating as isotropic noise [43]. "Scale" in CFT is therefore not primarily a length hierarchy; it is a persistence hierarchy [58]: how much of the ordering bias survives into observables before being washed out by isotropization.

The reason the language of subspaces appears is also not a claim of extra dimensions. It is a statement about *kinematic decomposition* once an ordering direction exists [59]. The presence of a physical ordering gradient defines a distinguished unit direction $n^\mu \propto \nabla^\mu T$, and with it an unavoidable splitting of response into a rank–1 longitudinal sector and a rank–3 transverse sector [43]. This is not optional. It is the same mathematical inevitability as defining "parallel" and "perpendicular" once a direction exists in Euclidean

space—except here the direction is not a spatial axis but the physical ordering axis of time [60].

This is the correct interpretation of why Gaussian statistics appear first in experiments [61]. Gaussianity is not the signature of "no structure"; it is the earliest measurable imprint of a constrained ensemble when the ordering bias is present but only weakly resolved [62]. The moment the ordering curvature becomes resolvable—i.e., the moment the admissible measure ceases to be uniform across histories—the distribution departs from Gaussian form [26–29,43]. In CFT, those departures are not arbitrary: they are the footprint of corridor partitioning and non-extensive weighting of admissible paths [26–29,63].

Said plainly: the same ordering field that biases the earliest statistical signatures of motion is the same field that later becomes visible as coherent anisotropy [43]. In collider systems it appears as persistent azimuthal ordering that cannot be reduced to a naive hydrodynamic afterthought [3–6,25]. In galaxies it appears as standing-wave locking of admissibility rather than particle halos [7–9,30–32]. In compact objects it appears as the anchor itself, forcing a Penrose switching zone in which longitudinal and transverse channels become comparable [36–38,64].

Therefore, we do not say "above the ultraviolet cutoff." We say: the chronoscalar ordering is present wherever there is time, and it is measurable wherever a system can retain enough coherence for admissible corridor geometry to imprint itself on observables [43]. The story is not ultraviolet. The story is time.

2.6. Chronoscalar Geometry and the Hessian Flip

We postulate that irreversible physical evolution is governed by a scalar ordering field $T(x^\mu)$ defined on spacetime, whose gradient is everywhere nonvanishing on physical histories [65–67]. Unlike coordinate time, T is a physical field encoding admissible ordering, in the sense that it constrains the set of realizable histories rather than merely parameterizing them [68–70]. Its gradient defines a preferred timelike direction,

$$n_\mu \equiv \frac{\nabla_\mu T}{\sqrt{-\nabla_\alpha T\, \nabla^\alpha T}}, \tag{11}$$

which reduces locally to the thermodynamic arrow in macroscopic systems [71,72] and to the Brownian entropy gradient in stochastic systems [65,66,68]. The projector onto the instantaneous rest frame orthogonal to n^μ is

$$\Delta_{\mu\nu} \equiv g_{\mu\nu} + n_\mu n_\nu. \tag{12}$$

The central geometric object controlling admissibility is the Hessian of T,

$$H_{\mu\nu} \equiv \nabla_\mu \nabla_\nu T, \tag{13}$$

and in particular its spatially projected form

$$H^{\perp}_{\mu\nu} \;\equiv\; \Delta_{\mu}{}^{\alpha}\Delta_{\nu}{}^{\beta}H_{\alpha\beta}. \tag{14}$$

At any point, $H^{\perp}_{\mu\nu}$ admits an orthonormal eigen-decomposition $H^{\perp}_{\mu\nu}e^{(a)\nu} = \lambda_a e^{(a)}_{\mu}$ with $a = 1,2,3$. Negative eigenvalues correspond to directions along which nearby trajectories are geometrically stabilized, while positive eigenvalues correspond to directions of instability or dispersion, as familiar from diffusion on curved manifolds and nonequilibrium stochastic geometry [68–70].

The crucial observation is that the same curvature directions play *opposite roles* at different scales. Microscopic admissibility follows negative-curvature directions of T, while macroscopic dissipation is enhanced along precisely those directions. This sign inversion defines the *Hessian flip*. Closely related scale-dependent reversals between stability and dissipation appear in extended hydrodynamics and kinetic theory when admissibility constraints are imposed [72–74].

We encode the Hessian flip in the dimensionless, covariant operator

$$\mathcal{F}_{\mu\nu}(H_T) \;\equiv\; \sum_{a=1}^{3} \mathrm{sign}(-\lambda_a)\, e^{(a)}_{\mu} e^{(a)}_{\nu}, \tag{15}$$

with the understanding that a smooth regulator (e.g. $\tanh(\lambda_a/\lambda_*)$) may be used when eigenvalues approach zero [73,75]. The operator $\mathcal{F}_{\mu\nu}$ is symmetric, traceless in the projected subspace, and transforms covariantly under diffeomorphisms, ensuring consistency with relativistic transport frameworks [72–74].

Physically, $\mathcal{F}_{\mu\nu}$ acts as a selector of admissible corridors: it assigns positive weight to directions in which ordering curvature suppresses microscopic divergence, and negative weight to directions in which trajectories are geometrically unstable. At small scales this restricts stochastic motion [65,68]; at large scales it enhances dissipation, producing an internally regulated transport law without introducing additional degrees of freedom, analogous in spirit to causal dissipative closures [72–74].

The appearance of $\mathcal{F}_{\mu\nu}$ implies that isotropic quadratic forms are no longer fundamental. In momentum space, any propagator or transport kernel inherits a deformed quadratic form,

$$Q(p;T) \;\equiv\; p_\mu p_\nu \left(g^{\mu\nu} + \varepsilon_1(T)\, n^\mu n^\nu + \varepsilon_2(T)\, \mathcal{F}^{\mu\nu}(H_T)\right), \tag{16}$$

where $\varepsilon_{1,2}(T)$ are scalar response functions fixed by the background ordering. Such anisotropic deformations of quadratic forms are well known to bias transport and response in nonequilibrium systems without altering local microcausality [69,70].

The corresponding scalar propagator takes the form

$$G(p;T) \;=\; \frac{i}{Q(p;T) - m^2 + i\epsilon}. \tag{17}$$

No new interaction vertex is introduced; instead, the admissible phase-space measure is geometrically tilted. We refer to this deformation as a *geometric yaw* of the propagator, in analogy with biased path-integral measures in superstatistical and large-deviation frameworks [70,76].

This yaw does not alter local microcausality or the pole structure of the theory. Rather, it biases the weighting of histories in the ordering-measure formulation. When ensembles of such yawed propagators are coarse-grained over spatially varying T-corridors, the resulting stationary distributions are generically non-extensive, as observed in both stochastic and high-energy systems [67,76–78]. In particular, fluctuations in the effective dissipation functional induce a q-exponential stationary state,

$$f(p_T) \;\propto\; \left[1 + (q-1)\frac{p_T}{T_{\rm eff}}\right]^{-1/(q-1)}, \tag{18}$$

with

$$q - 1 \;=\; \frac{\mathrm{Var}(\beta_T)}{\langle \beta_T \rangle^2}, \tag{19}$$

where β_T is the local ordering-weight conjugate to dissipation. Thus the Tsallis index q is not an empirical deformation parameter but a direct geometric measure of ordering-curvature variance [76,78].

In this sense, Brownian motion already probes the chronoscalar geometry: it is the minimal system in which the Hessian of T constrains admissible paths before any macroscopic structure forms [65,66,68]. The same operator $\mathcal{F}_{\mu\nu}$ that filters microscopic diffusion will reappear in relativistic transport, horizon dissipation, and gravitational dynamics [71–74]. The remainder of this paper develops these projections explicitly.

3. MICROSCOPIC REGIME: BROWNIAN MOTION AND NON-EXTENSIVE STATISTICS

Brownian motion constitutes the minimal physical regime in which irreversible evolution appears without macroscopic structure [79,80]. It is therefore the earliest scale at which the ordering geometry encoded by $T(x^\mu)$ can be detected. In the absence of long-range forces, coherent flows, or horizon effects, any persistent directionality or correlation in the statistics of particle trajectories must originate from background admissibility rather than dynamics, consistent with stochastic and thermodynamic treatments of irreversibility [81,82].

We begin with the nonrelativistic limit of a test particle of mass m embedded in a medium characterized by a slowly varying chronoscalar background. The particle velocity $v_i(t)$ obeys a generalized Langevin equation,

$$m\dot{v}_i = -\Gamma_{ij}(T)\, v_j + \xi_i(t), \tag{20}$$

where Γ_{ij} is an anisotropic friction tensor and ξ_i is a stochastic force with zero mean. Generalized and anisotropic Langevin descriptions of this type are standard when background structure biases admissible trajectories [83,84]. The chronoscalar direction $n_i \propto \partial_i T$ induces the decomposition

$$\Gamma_{ij} = \gamma_\perp \delta_{ij} + (\gamma_\parallel - \gamma_\perp)\, n_i n_j, \tag{21}$$

so that dissipation along the ordering gradient differs from dissipation transverse to it. Such directional friction is known to encode geometric or entropic constraints on diffusion [85,86]. This anisotropy is the nonrelativistic shadow of the Hessian flip operator introduced in Sec. II.

The noise correlator is constrained by a generalized fluctuation–dissipation relation. Because admissible trajectories are geometrically filtered by T-corridors, the stochastic force cannot be assumed Gaussian in the Boltzmann–Gibbs sense [81,87]. Instead, the noise variance itself fluctuates across admissible microhistories,

$$\langle \xi_i(t)\xi_j(t')\rangle_{\beta_T} = 2\,\Gamma_{ij}\,\beta_T^{-1}\,\delta(t-t'), \tag{22}$$

where β_T is a local ordering weight conjugate to dissipation. Fluctuating inverse temperature or dissipation weights of this type arise naturally in superstatistical and large-deviation treatments of nonequilibrium systems [88,89]. Crucially, β_T is not constant: it depends on the local curvature and gradient structure of T.

Averaging over admissible corridors therefore requires integrating over a distribution $f_T(\beta)$ determined by the chronoscalar geometry. The corresponding Fokker–ultraviolet equation for the single-particle distribution $P(v,t)$ becomes

$$\partial_t P = \int d\beta\, f_T(\beta)\, \partial_i \left[\Gamma_{ij}\left(v_j P + \beta^{-1}\partial_j P\right)\right], \tag{23}$$

which generalizes the standard Fokker–ultraviolet description to ensembles with fluctuating dissipation weights [88–90]. For a broad and natural class of corridor-weight distributions—specifically gamma-family distributions generated by quadratic dissipation functionals—the stationary solution is a q-exponential,

The Tsallis index q is thus a direct geometric observable: it measures the relative variance of admissible ordering weights induced by the curvature of T.

The anisotropy of the chronoscalar background further implies that the effective non-extensivity differs by direction. Decomposing velocities into longitudinal and transverse components with respect to n_i, one finds

$$q_\perp > q_\parallel \qquad \Longleftrightarrow \qquad \gamma_\perp > \gamma_\parallel, \tag{24}$$

a directional splitting consistent with anisotropic diffusion and transport in constrained geometries [85,86,90]. The statistical splitting $\Delta q = q_\perp - q_\parallel$ is therefore not a fit artifact but a necessary consequence of anisotropic admissibility.

This result completes the logical arc from geometry to statistics. Brownian motion does not "generate" non-extensive behavior; it *reveals* it. The chronoscalar field constrains the ensemble of admissible paths before any macroscopic structure exists, and the resulting non-Gaussian statistics are the earliest measurable imprint of that constraint [79,81,88]. At higher energies and curvatures, the same ordering geometry will reappear as anisotropic viscosity, modified horizon dissipation, and ultimately as a regulator of gravitational collapse.

4. MESOSCALE: COLLIDER PHENOMENOLOGY AND THE UNIVERSAL EXPONENT

4.1. Empirical Collider Reverse-Zone and Baryonic Gain

The same corridor-switch logic applies in collider "reverse zones," where the effective ordering direction changes sign across rapidity or across strong longitudinal gradients in the produced medium. In such regions, anisotropic corridors can be open at production but close during hadronization (or vice versa), creating a realized gain or suppression in the surviving channel. Because baryons and antibaryons can occupy different corridor supports through spin/chirality-dependent transport and hadronization pathways, a corridor switch can manifest as an apparent baryon enhancement that is not reducible to an equilibrium thermal parameter shift [125–127]. This provides a unified language for (i) persistent anisotropic flow, (ii) non-extensive spectral forms, and (iii) baryonic asymmetries as corridor-weight effects rather than as independent anomalies [125–128].

5. ASTROPHYSICAL SCALE: GALACTIC DYNAMICS AND STANDING-WAVE LOCKING

In Chronoscalar Field Theory (CFT), galactic rotation curves are not interpreted as evidence for missing mass, nor as a modification of the gravitational potential. Instead, they are understood as the macroscopic manifestation of a standing-wave ordering process anchored by the central compact object and regulated by admissible transport in the chronoscalar field $T(x^\mu)$ [188,189].

A key empirical claim in this section is *not* qualitative: the residual structure in $\delta v(\log r)$ contains a phase-locked harmonic pair with a robust 1:2 frequency relationship,

$$\boxed{\begin{aligned} &f_{\sin} \simeq 2 f_{\cos}, \\ &f_{\cos} \approx 0.332, \quad f_{\sin} \approx 0.666 \\ &\qquad \text{cycles per } \log_{10}(\mathrm{kpc}). \end{aligned}} \tag{25}$$

Equivalently, the corresponding wavelengths in $\log_{10}(\mathrm{kpc})$ are $\lambda_{\cos} = 1/f_{\cos} \approx 3.01$

decades and $\lambda_{\sin} = 1/f_{\sin} \approx 1.50$ decades: the "sine" channel is the second harmonic of the "cosine" anchor.

This is *not* asserted by fitting freedom in this manuscript. It is extracted from the uploaded rotation-curve datasets using two independent estimators (FFT and Hilbert phase) and cross-checked against an ensemble stack. The methods are stated explicitly below.

5.1. Black Hole Spin as the Ordering Anchor

The central black hole does not merely supply a deep potential well; it provides a *rotational anchor* that fixes the phase structure of the surrounding chronoscalar mesh. Its spin ω_{BH} defines the reference orientation for admissible transport corridors in the inner galaxy, setting the initial phase of the ordering field. All subsequent orbital dynamics are measured relative to this anchor.

Crucially, the black hole spin does not contribute linearly to acceleration. Instead, it controls the *projection angle* $\theta(r)$ between longitudinal (ordering-aligned) and transverse (ordering-opposed) transport channels. At small radii, strong anchoring forces $\theta \approx 0$, and motion is dominantly longitudinal. At larger radii, progressive yaw of the chronoscalar mesh drives $\theta \to \pi/2$, activating transverse transport [190].

5.2. Cosine–Sine Decomposition of Admissible Acceleration

The total radial acceleration is therefore not a scalar sum but a phase-resolved vector projection,

$$\boxed{a_{\mathrm{tot}}(r) = a_{\mathrm{bar}}(r)\,\cos\theta(r) + a_{\perp}(r)\,\sin\theta(r)\left(1 + \beta H_{\mathrm{flip}}\right)} \tag{26}$$

where $a_{\mathrm{bar}}(r)$ is the Newtonian baryonic contribution, and $a_{\perp}(r)$ is the transverse chronoscalar response generated by residual ordering tension $A_0 \equiv cH_0$ [189].

The cosine channel represents low-cost, long-range longitudinal transport, which dominates in isotropic regimes and reproduces classical gravity in the Euclidean limit. The sine channel represents high-cost transverse transport, activated by rotation, torsion, and nematic ordering. This transverse response is precisely the channel misidentified as "dark matter" in conventional analyses [191,192].

5.3. Penrose Transition as a Phase Boundary

The transition between these regimes is sharp and geometric. At the Penrose radius r_{P}, defined implicitly by

$$a_{\mathrm{bar}}(r_{\mathrm{P}}) = a_{\perp}(r_{\mathrm{P}}), \tag{27}$$

the system reaches $\theta \simeq \pi/4$, and longitudinal and transverse channels carry equal weight. This marks a genuine phase transition in admissible transport, not a smooth interpolation.

Inside $r_{\rm P}$, motion is sliding and Brownian-like, dominated by longitudinal admissibility. Outside $r_{\rm P}$, transverse costs dominate, forcing the system into a collective, ordered response. The rotation curve flattens because the system has entered a standing-wave regime in which additional radius no longer increases effective acceleration [190].

5.4. Aggregate Sine Accumulation and Standing-Wave Cleaning

The sine contribution is not instantaneous. It represents the *aggregate accumulation of admissibility cost* along transverse corridors,

$$\mathcal{S}(r) \;\equiv\; \int^{\tau(r)} \sin\theta(\tau')\, d\tau'. \tag{28}$$

At small radii this accumulation is noisy and dissipative, corresponding to chaotic ejecta and enhanced entropy production, as observed in high-spin merger remnants and correlated many-body systems [193,194].

At specific radii, however, the accumulated phase locks to the background chronoscalar registry. Dissipation collapses into geometry, and the system forms a standing wave. These locking points are the Fibonacci nodes,

$$\boxed{r_n = R_*\,\varphi^n, \qquad \varphi = \frac{1+\sqrt{5}}{2},} \tag{29}$$

which represent relocking of admissible corridors to successive Machian equilibria [195,196].

5.5. Fibonacci Nodes and Baryonic Shell Alignment

At each Fibonacci node, the transverse drift halts and rephases with the longitudinal channel. The consequence is twofold: (i) the rotation curve exhibits a stabilized plateau or mild kink, and (ii) baryonic matter preferentially accumulates at these radii. This explains the observed correspondence between spiral arm loci, ring structures, and subtle features in high-resolution rotation curves.

The galaxy therefore behaves as a macroscopic atom: the black hole acts as the nucleus, the chronoscalar field provides the ordering mesh, and baryons occupy discrete resonance shells. The analogy is structural, not quantum, and persists across scales from stellar systems to galaxy clusters [197].

5.6. Implications for Spin Limits and Superradiance

Because the sine channel represents accumulated transverse cost, it saturates. Increasing spin beyond the saturation threshold does not increase binding but triggers

ejective channels. This mechanism enforces sub-extremal spin bounds for compact objects and explains superradiance as corridor over-occupation followed by selective leakage [198,199].

Incoming wave packets decompose into corridor components; isotropic modes are absorbed, while ordering-aligned modes survive with enhanced normalization. Quasi-normal mode frequencies therefore probe corridor stiffness, and damping rates measure leakage from the standing-wave zone [200,201].

5.7. Data-anchored extraction of the 1:2 *harmonic lock*

This manuscript uses four uploaded data products (CSV outputs) to anchor the harmonic claim:

(i) `UGC12632_FFT_channels.csv` provides direct channel peaks at $f_{\cos} = 0.332$ and $f_{\sin} = 0.666$ cycles per $\log_{10}(\mathrm{kpc})$ and their normalized powers (single-galaxy channelization).

(ii) `SPARC_stack_fft_peak.csv` reports the dominant stacked peak of the SPARC ensemble residual spectrum (stacked estimator).

(iii) `SPARC_stack_hilbert.csv` provides the analytic phase $\phi(x)$ of the stacked residual; instantaneous frequency is obtained by

$$f_{\mathrm{H}}(x) \;=\; \frac{1}{2\pi}\,\frac{d\phi}{dx}, \qquad x \equiv \log_{10}(r/R_{*}). \tag{30}$$

The operational Hilbert estimate used here is the empirical distribution of $f_{\mathrm{H}}(x)$ over the support where the analytic amplitude is non-negligible [202,203]. The lock claim is that the ensemble supports a frequency band consistent with the second harmonic of the single-galaxy cosine anchor.

(iv) `SPARC_Rstar_summary.csv` supplies the actual ensemble size and node counts used in the collective significance estimate below.

Why the 1:2 **relationship is a standing-wave statement (not a fit).** A standing wave in $\log_{10}(r)$ has harmonics at integer multiples of a fundamental frequency. If the fundamental is $f_{\cos} \approx 0.332$, the second harmonic is fixed at $2f_{\cos} \approx 0.664$ *without adjustable parameters*. Thus the observed $f_{\sin} \approx 0.666$ is not an independent fit number: it is the discrete harmonic implied by standing-wave registry on the $\log_{10}(\mathrm{kpc})$ axis.

Power concentration check (non-flat spectrum). A necessary condition for "registry" rather than broadband noise is that the spectral power is concentrated in a narrow band around the harmonic peaks (and not distributed uniformly). This condition is tested directly on the uploaded spectra/peak summaries [202,204].

5.8. Collective σ for phase-lock evidence (explicit methodology)

The collective significance is computed from *node-level* independence rather than "galaxy-level" counting. In the uploaded `SPARC_Rstar_summary.csv`, each galaxy contributes an integer number of independent radial nodes (`n_points`) corresponding to distinct radius samples in the residual structure. The ensemble statistics are:

$$\boxed{N_{\rm gal} = 139, \qquad N_{\rm nodes} = \sum_{\rm gal} n_{\rm points} = 3153.} \tag{31}$$

Null model and per-node chance probability. Under the conservative null hypothesis "random Newtonian residual structure" the event "a node supports the 1:2 harmonic alignment within tolerance" is assigned a per-node chance probability p (the manuscript keeps p explicit; numerical examples below use the conservative $p = 0.01$ advocated in the SPARC-scatter argument). Importantly, p is a *data-side* knob: it is either set conservatively or measured by permutation tests (shuffling residuals across radii) on the same datasets [202,205].

Multiplicative phase-lock logic. If each node is a discrete "chance bit" for registry, the probability of observing the registry across $N_{\rm nodes}$ independent nodes is $p^{N_{\rm nodes}}$. Converting this to a Gaussian-equivalent significance yields the commonly used large-deviation form

$$\boxed{\sigma_{\rm collective} \;=\; \sqrt{2\,N_{\rm nodes}\,\ln(1/p)}.} \tag{32}$$

For the explicit values in the uploaded ensemble and the conservative choice $p = 0.01$,

$$\sigma_{\rm collective} = \sqrt{2 \cdot 3153 \cdot \ln(100)} \approx 170.3\,\sigma. \tag{33}$$

This number is *not* a claim about cosmology; it is a formal statement about how strong the evidence becomes *if* node independence holds and *if* the node-level false-alignment probability is bounded by p.

Additive benchmark (for comparison only). If one instead treats each node as contributing an additive z-score and sums in quadrature, one obtains

$$\sigma_{\rm additive} \;=\; z_p\,\sqrt{N_{\rm nodes}}, \tag{34}$$

where z_p is the one-node Gaussian equivalent for the same p (for $p = 0.01$, $z_p = 2.326$). Using $N_{\rm nodes} = 3153$ gives $\sigma_{\rm additive} \approx 130.6\,\sigma$. The manuscript reports both so the reader can see exactly where the "multiplicative" assumption enters.

Statistical validation checks. The Results explicitly establish (i) the empirical determination of the null probability p via permutation tests applied to the same rotation-curve residuals; (ii) the effective independence of radial nodes at the level required for likelihood accumulation; and (iii) the stability of the identified harmonic band under changes in detrending and radial windowing. These checks are performed directly on the datasets and do not rely on model-specific assumptions [202,205].

6. GRAVITATIONAL COLLAPSE AND REGULAR CORES

The formation of a black hole provides the most stringent test of any ordering principle, as it probes the regime in which classical classical metric theory predicts geodesic incompleteness and divergent curvature. In the standard Penrose–standard thermal prediction framework, gravitational collapse proceeds under isotropic stress and classical energy conditions, forcing the focusing of timelike and null congruences toward a spacetime singularity [92,93]. In the chronoscalar framework, this conclusion is altered at a structural level: collapse is constrained by the admissibility geometry imposed by the ordering field $T(x^\mu)$.

We consider the collapse of a self-gravitating fluid with four-velocity u^μ and stress–energy tensor

$$T_{\mu\nu} = (\rho + p)\, u_\mu u_\nu + p\, g_{\mu\nu} + \Pi^T_{\mu\nu}, \tag{35}$$

where $\Pi^T_{\mu\nu}$ is the anisotropic dissipative stress generated by the chronoscalar sector. As shown in previous sections, $\Pi^T_{\mu\nu}$ is constructed from the Hessian–flip operator $\mathcal{F}_{\mu\nu}(H_T)$ and therefore encodes directional resistance aligned with negative-curvature ordering corridors. Anisotropic stress contributions of this form are known to qualitatively alter collapse dynamics when they become comparable to isotropic pressure terms [94,95].

During the early stages of collapse, when curvature gradients are small, $\Pi^T_{\mu\nu}$ is negligible and classical dynamics is recovered. However, as density increases and spacetime curvature sharpens, the chronoscalar Hessian necessarily develops large eigenvalue contrast. Negative-curvature directions define admissible corridors that stabilize microscopic trajectories, while the Hessian flip enhances macroscopic dissipation along those same directions. The net effect is the emergence of an *internal geometric resistance* to further isotropic compression, analogous in spirit to—but distinct in origin from—previous regularization mechanisms based on anisotropic interiors [95–100].

This resistance modifies the Raychaudhuri equation governing the expansion θ of timelike congruences. Including the chronoscalar stress, one finds

$$\frac{d\theta}{d\tau} = -\frac{1}{3}\theta^2 - \sigma_{\mu\nu}\sigma^{\mu\nu} + \omega_{\mu\nu}\omega^{\mu\nu} - R_{\mu\nu}u^\mu u^\nu + \mathcal{R}_T, \tag{36}$$

where $\mathcal{R}_T$ is a positive-definite correction sourced by $\nabla^\nu \Pi^T_{\mu\nu} u^\mu$. This term counteracts geodesic focusing once ordering curvature becomes large, directly modifying the

conditions required for singularity formation in classical collapse [92,93,99]. Crucially, $\mathcal{R}_T$ arises dynamically from the geometry of T and does not require violation of low-curvature classical metric theory or exotic matter sources.

As collapse proceeds, the chronoscalar gradient aligns increasingly with the radial direction. Compression transverse to ∇T is preferentially damped, while longitudinal collapse is slowed by anisotropic dissipation. The collapse therefore evolves toward a quasi-stationary configuration in which further focusing is dynamically suppressed. Instead of forming a curvature singularity at $r = 0$, the system approaches a finite-density core characterized by bounded curvature invariants and geodesic completeness, consistent with known regular interior solutions supported by anisotropic stress [97–100].

The endpoint of collapse is thus a black hole with a regular interior, whose exterior metric approaches the classical rotating solution family at large radii but deviates in the deep interior where $\Pi^T_{\mu\nu}$ dominates. classical trapping surface formation is not prevented; rather, it occurs *before* any singular behavior can develop, shielding the regular core from external observers. In this sense, the chronoscalar framework enforces cosmic censorship through internal geometric regulation rather than through external boundary assumptions [94,101].

An immediate consequence concerns angular momentum. In classical collapse, the extremal limit $a_* \to 1$ is kinematically allowed and is regulated only by accretion and radiative losses. In the chronoscalar framework, anisotropic ordering stress produces a nonlinear geometric resistance to differential rotation. As the spin parameter increases, the Hessian–flip channels associated with azimuthal shear become increasingly dissipative, preventing the formation of an unstable extremal classical rotating solution state. The physically realized bound is therefore

$$a_* < 1, \tag{37}$$

with the inequality enforced internally by ordering geometry rather than by environmental effects, in agreement with both theoretical stability arguments and astrophysical spin measurements [101–105].

Black hole formation in the chronoscalar framework is thus neither singular nor exotic. It is the natural continuation of admissible transport under extreme curvature: collapse proceeds, horizons form, but the ordering field forbids infinite compression and preserves causal structure throughout the evolution. The horizon properties and their thermodynamic interpretation will be developed in the next section.

7. HORIZON DYNAMICS AND MEMBRANE TRANSPORT

Once collapse produces a trapped surface, the chronoscalar framework enters a regime in which ordering admissibility must be encoded as an effective boundary dynamics.

The horizon is no longer treated merely as a null geometric locus but as a transport interface separating admissible exterior histories from a corridor-regulated interior. The natural language for this regime is the membrane paradigm, understood here not as a reformulation of historical metric formulation gravity but as a hydrodynamic representation of near-horizon transport once a causal boundary forms [106–108]. In Chronoscalar Field Theory the membrane transport coefficients are not postulated phenomenologically; they descend directly from the ordering field $T(x^\mu)$ through the Hessian flip and its associated anisotropic dissipation channels.

To make this precise, let $\mathcal{H}_\epsilon$ denote a stretched timelike surface located a proper distance ϵ outside the null horizon. In the chronoscalar picture, $\mathcal{H}_\epsilon$ is the surface on which admissibility is enforced: bulk transport currents terminate into surface currents, and corridor-weighted dissipation is encoded as surface stress, entropy production, and heat flow. This construction preserves the empirical successes of horizon thermodynamics while allowing for microscopic correlations controlled by the ordering geometry, rather than assuming independent horizon degrees of freedom [106–109].

The effective membrane stress tensor is obtained by integrating the chronoscalar transport balance laws across a thin Gaussian normal layer straddling $\mathcal{H}_\epsilon$. Denoting by γ_{ab} the induced metric on the stretched horizon, by u^a the membrane four-velocity, and by σ_{ab} and θ the shear and expansion of the membrane congruence, one finds an effective surface stress of the form

$$t_{ab} = (\epsilon_h + p_h)u_a u_b + p_h \gamma_{ab} - 2\,\eta_{ab}^{(T)}\,\sigma^{ab} - \zeta^{(T)}\,\theta\,\gamma_{ab}. \tag{38}$$

This expression should be read as a *constitutive identity* arising from the projection of chronoscalar transport onto $\mathcal{H}_\epsilon$, not as a direct consequence of the historical metric formulation field equations [106–108]. The quantities (ϵ_h, p_h) encode the membrane energy and pressure densities, while $(\eta_{ab}^{(T)}, \zeta^{(T)})$ encode corridor-selected dissipation inherited from the bulk ordering geometry.

A central prediction of CFT is that horizon dissipation is intrinsically anisotropic. Because the admissible corridor structure is anisotropic, the ordering direction $n^\mu \propto \nabla^\mu T$ projects to a preferred spatial direction n_a on the membrane. The Hessian flip selects negative-curvature corridors of T and enhances dissipation along precisely those directions. As a result, the horizon viscosity is tensorial rather than scalar,

$$\eta_{ab}^{(T)} = \eta_\perp\,\gamma_{ab} + (\eta_\parallel - \eta_\perp)\,n_a n_b, \tag{39}$$

so that shear aligned with n_a and shear transverse to n_a dissipate at different rates. This anisotropic viscosity hierarchy is the direct horizon analogue of the transport splitting inferred from the Brownian/Tsallis regime and from relativistic heavy-ion flow, now realized at a causal boundary where admissibility is enforced rather than assumed [110–113].

The same ordering geometry that governs dissipation also governs horizon entropy, but not through lightlike mode counting or Euclidean periodicity. In Chronoscalar Field Theory the horizon is not a null surface defined by infinite redshift, nor does it bound a singular interior. Instead, it is an admissibility boundary at which chronoscalar transport saturates and corridor survival collapses.

As a result, the area-law entropy–standard thermal prediction area law does not provide the correct entropy, even at leading order. Its derivation relies on independent horizon microcells, factorized state space structure, and a Euclidean time identification that is incompatible with a physical ordering field $T(x^\mu)$. All of these assumptions are violated once time is treated as a dynamical scalar with nontrivial curvature.

In the chronoscalar framework, entropy measures the obstruction to admissible ordering transport rather than the count of independent microstates. The horizon degrees of freedom are intrinsically correlated through the geometry of ∇T and the projected Hessian $H_\perp^{\mu\nu}$, and the resulting entropy is non-extensive.

No identification with the standard thermal prediction temperature is made. Thermal emission, when defined, is controlled by the saturation of chronoscalar ordering flux rather than by surface gravity or light-cone kinematics. The natural entropy in this setting is therefore of Tsallis type,

$$S_q = \frac{1}{q-1}\left(1 - \sum_i p_i^q\right), \tag{40}$$

with $q > 1$ fixed by the variance of ordering curvature weights at the horizon. In this formulation, $q-1$ is not a fit parameter but a geometric observable measuring the strength of admissibility correlations, governed by the same corridor-weight fluctuations that produce q-exponential stationary states in the Brownian regime [115–117].

Importantly, no identification is made between chronoscalar emission scales and the surface-gravity expression $\kappa/2\pi$. In Chronoscalar Field Theory the horizon is not a null, infinite-redshift surface supporting the standard thermal prediction derivation; it is an *admissibility boundary* where corridor survival saturates and transport becomes geometry-limited. The relevant scale is therefore set by the local ordering geometry, not by light-cone kinematics. We define the chronoscalar emission scale by the ordering-flux impedance,

$$\Theta_{\rm CFT}^{-1} \;\equiv\; \left.\frac{\partial S_{\rm CFT}}{\partial \mathcal{J}_T}\right|_{\Sigma}, \tag{41}$$

where $\mathcal{J}_T$ is the chronoscalar ordering current through the stretched admissibility surface Σ and $S_{\rm CFT}$ is the correlated (non-extensive) horizon entropy functional. This definition is covariant, bounded, and does not rely on Euclidean time periodicity or independent microcells.

The emission spectrum is then not "thermal with corrections" but *corridor-weighted* from the outset: the observed distribution reflects anisotropic admissibility weights and

their correlations across the horizon surface. In the weak-correlation limit $q \to 1$ and vanishing Hessian-contrast, Θ_{CFT} reduces to a single, direction-independent scale and the spectrum approaches a ultraviolet-like form; for the physical chronoscalar horizon, $q > 1$ and finite Hessian variance enforce controlled, power-law tails and orientation dependence that encode correlated microstructure rather than perfectly thermal emission. In this way, chronoscalar ordering preserves the successes of horizon thermodynamics while extending it to include anisotropy, correlation, and internal regulation.

Taken together, these results show that horizons in CFT are neither singular boundaries nor purely kinematic constructs. They are admissibility interfaces whose transport properties, entropy, and stability are fixed by the same Hessian-flip geometry that regulates collapse and enforces sub-extremal spin. The horizon therefore completes, rather than contradicts, the chronoscalar resolution of gravitational collapse.

7.1. Theorem-Level Horizon Consequences

Theorem 1 (Regular Core Theorem). *In a spacetime endowed with a physical chronoscalar ordering field $T(x^\mu)$, the interior of a dynamically formed black hole contains no curvature singularity. All scalar curvature invariants remain finite, and timelike and null geodesics are complete.* [96–98]

Proof sketch. The chronoscalar stress $\Pi^T_{\mu\nu}$ activates under large ordering curvature and generates a positive-definite anti-focusing correction to congruence evolution. Since the Hessian flip strengthens with curvature contrast, the regulation is self-amplifying in the high-curvature regime. Horizon formation occurs before any divergence can develop, causally shielding a finite-density, regular core while preserving classical rotating solution-like exterior behavior [96–99]. □

Theorem 2 (Sub–Extremal Spin Theorem). *Black holes formed in the presence of a chronoscalar ordering field satisfy $a_* < 1$ as a strict inequality. The extremal classical rotating solution state is dynamically forbidden by internal geometric resistance.* [99–101]

Proof sketch. As a_* increases, azimuthal shear near the horizon increases the Hessian contrast of T and strengthens flip-selected dissipation channels. The associated entropy production grows superlinearly with differential rotation, enforcing an intrinsic equilibrium bound below extremality. This bound is internal to admissibility geometry and does not require environmental torques, accretion regulation, or radiative fine-tuning [90,100,101]. □

7.2. Information: Correlated Horizon Fluid as the Unitarity Channel

In the chronoscalar framework, standard thermal prediction radiation is not an

uncorrelated thermal flux but an emission process from an anisotropic, correlated horizon fluid. Information is stored and transported in the non-extensive correlations encoded by $q > 1$, so purity is preserved in principle without invoking remnants, firewalls, or acausal nonlocality. The observable signature is not a gross shift of T_H but controlled, correlation-driven deviations of spectra and polarization-dependent dissipation consistent with anisotropic horizon transport [93–97].

The horizon therefore marks not the breakdown of physics but the transition to a regime where ordering geometry dominates. The same admissibility structure that constrains Brownian motion at micron scales governs horizon dissipation and black-hole interiors at astronomical scales.

8. PENROSE MECHANISM AND SUPERRADIANCE

In CFT, the Penrose process is not defined by negative-energy geodesics in a classical rotating solution ergosphere, but by a *corridor-switch* of admissible transport across a rotating ordering geometry. Rotation (or any strong azimuthal ordering shear) tilts the local chronoscalar direction $n^\mu \propto \nabla^\mu T$ and rotates the eigen-corridors of the projected Hessian $H^\perp_{\mu\nu}$ with radius. This creates a radius-localized *conversion zone* in which admissible measure is re-partitioned between anisotropic (ordering-aligned) and isotropic (thermalized) corridors. The observed "energy extraction" is the realized momentum gain of the escaping branch after this corridor switch, not a coordinate artifact [119–122].

A. Corridor decomposition and switch kinematics

Let $\hat{n}$ denote the local spatial ordering direction on a constant-time slice (the projection of n^μ), and let $\hat{p}$ be the direction of an outgoing excitation (particle, wavepacket, or collective mode). Define the corridor angle

$$\cos\theta \equiv \hat{p} \cdot \hat{n}. \tag{42}$$

The admissible momentum is naturally decomposed into anisotropic and isotropic components

$$p_{\text{aniso}} = p\,\cos\theta, \qquad p_{\text{iso}} = p\,\sin\theta, \tag{43}$$

with corresponding corridor weights

$$w_{\text{aniso}}(r) \propto \cos^2\theta(r), \qquad w_{\text{iso}}(r) \propto \sin^2\theta(r). \tag{44}$$

In a rotating ordering geometry, $\theta(r)$ is not constant: the ordering axis winds with radius and the Hessian eigenbasis rotates, so $d\theta/dr \neq 0$ in a finite radial band. This defines the *Penrose switching zone* $\mathcal{Z}_P$, bounded by radii where the dominant corridor eigenvalue ordering changes sign under the Hessian flip [119–123].

The crucial point is that admissibility is not symmetric between the two sectors: anisotropic corridors carry coherent ordering flux, while isotropic corridors represent a high-entropy bath. When a trajectory enters $\mathcal{Z}_P$, the admissible measure is reweighted. If the ingoing excitation splits into two branches whose corridor supports differ (one more anisotropic, one more isotropic), then the branch that becomes inadmissible is absorbed into the interior reservoir, while the surviving branch inherits the full normalization of the outgoing measure. The escaping branch therefore exhibits a *realized momentum gain* relative to what would be inferred without corridor reweighting:

$$p_{\mathrm{out}} \;=\; p_{\mathrm{in}} \sqrt{\frac{w_{\mathrm{surv}}^{(\mathrm{out})}}{w_{\mathrm{surv}}^{(\mathrm{in})}}} \;>\; p_{\mathrm{in}} \qquad (\text{corridor switch in } \mathcal{Z}_P), \tag{45}$$

where w_{surv} denotes the surviving corridor weight on each side of the switch. This is the CFT Penrose mechanism: *extraction by admissibility re-partitioning* rather than by negative-energy bookkeeping [119–122].

8.1. Astrophysical Mapping: Jets as Anisotropic-corridor Exhaust

In the black-hole setting, the classical Penrose picture and the membrane paradigm identify a near-horizon region where rotation enables extraction of energy and angular momentum [119–122]. In CFT, the same region is interpreted as a corridor-switching layer in which azimuthal shear maximizes Hessian contrast and thus maximizes flip-selected dissipation and ordering-flux redirection. The escaping channel is preferentially aligned with the ordering direction and its associated eigen-corridor. This provides a direct geometric origin for collimated exhaust (jet launching) as *anisotropic-corridor exhaust* rather than a purely electromagnetic coincidence [121–124]. The key observable is that jet direction and stability track the ordering axis, not merely the spin axis; this distinction becomes measurable in systems with misaligned disks, warped inflows, or tumbling environments [123,124].

8.2. Prediction: Nematicity Amplitude Scales with the Penrose Switching Zone

CFT predicts that *nematicity is the condensed-matter analogue of corridor partitioning*. A nematic order parameter measures the splitting of responses along two orthogonal in-plane axes; in CFT language this is precisely the difference between anisotropic-corridor weight and isotropic background weight under an ordering axis embedded in the medium. Define a dimensionless corridor anisotropy measure

$$\mathcal{N} \;\equiv\; \frac{w_{\mathrm{aniso}} - w_{\mathrm{iso}}}{w_{\mathrm{aniso}} + w_{\mathrm{iso}}} \;=\; \cos(2\theta), \tag{46}$$

and define the integrated "switching strength" of a zone $\mathcal{Z}$ by

$$\Xi(\mathcal{Z}) \;\equiv\; \int_{\mathcal{Z}} dr \;\left|\frac{d\theta}{dr}\right|\; \mathcal{A}(r), \tag{47}$$

where $\mathcal{A}(r)$ is the local ordering-curvature amplitude (a scalar built from the projected Hessian eigenvalue contrast, e.g. $\mathcal{A} \sim |\lambda_-|/(\sum_a |\lambda_a|)$). Then the CFT prediction is:

Prediction (Scaled nematicity from corridor switching). *The observable nematic amplitude in a given system is proportional to the integrated corridor-switching strength of its active switching zone,*

$$\boxed{\Delta_{\mathrm{nem}} \;\propto\; \Xi(\mathcal{Z}_P)} \tag{48}$$

with the proportionality fixed by the same ordering-curvature variance that sets $q - 1$ in the non-extensive sector.

In iron-based superconductors, the nematic susceptibility and resistive anisotropy track a near-critical "nematic channel" whose strength varies across doping/pressure/strain. In CFT, this is interpreted as motion of the system through a corridor-switching zone in control parameter space, where the ordering axis rotates rapidly and eigen-corridors exchange dominance. The prediction is that the extracted nematic amplitude (e.g. elastoresistivity coefficients, shear-modulus softening, or transport anisotropy) collapses when plotted against the CFT switching-strength estimator Ξ constructed from the same data (via the measured anisotropy angle and curvature proxy) [129–133].

This scaling is falsifiable: it requires (i) a localized switch zone where θ evolves rapidly, (ii) a correlated, non-extensive fluctuation envelope (measurable via spectral tails or noise statistics), and (iii) a one-parameter collapse of nematic observables against Ξ. If confirmed, it would establish that astrophysical Penrose extraction, collider reverse-zone baryonic gain, and condensed-matter nematicity are all projections of a single chronoscalar corridor-switch mechanism.

8.3. Superradiance and Quasi-Normal Modes as Corridor Transport

In Chronoscalar Field Theory, superradiance and quasi-normal modes arise from the same underlying mechanism: the re-partitioning of admissible transport corridors within the Penrose switching zone. Neither phenomenon requires local particle creation, horizon-local degrees of freedom, or rectified propagation. Instead, both reflect the selective survival and leakage of wave-like excitations guided by the ordering geometry encoded in $T(x^\mu)$ [119–122].

Superradiance as Corridor Over-Occupation. Superradiant amplification occurs when an incoming wave packet enters the Penrose switching zone and decomposes into

components aligned and misaligned with the local ordering direction $n^\mu \propto \nabla^\mu T$. The projected Hessian $H^\perp_{\mu\nu}$ defines anisotropic ordering corridors associated with negative curvature and isotropic diffusive corridors associated with positive curvature. Upon crossing the switching zone, isotropic components lose admissibility and are absorbed, while anisotropic components remain admissible and inherit the full normalization of the incoming state. The result is an apparent amplification of the outgoing wave without violation of global conservation laws. This mechanism unifies the original Penrose process [119] with wave amplification in rotating systems [120–122].

Quasi-Normal Modes as EM-like Corridor Relaxation. Quasi-normal modes represent the relaxation spectrum of admissible corridor transport in the same switching zone. A perturbation excites a superposition of corridor modes, each characterized by a finite survival length and leakage rate. The observed QNM frequencies encode the curvature of the ordering axis, while the damping rates encode the rate at which corridors lose admissibility. Late-time power-law tails arise from the survival of long corridors that never fully close, producing non-ergodic relaxation rather than purely exponential decay [123–127].

In this sense, QNMs are EMR-like modes propagating through a lossy, anisotropic waveguide defined by the chronoscalar geometry. They do not represent rectified propagation or normal modes of a conservative system. Instead, they are marginal transport modes whose decay is governed by corridor leakage rather than by energy dissipation in the usual thermodynamic sense. This interpretation explains the sensitivity of QNM spectra to interior structure while preserving agreement with classical rotating solution behavior at large radii [124,125].

Non-Rectifying Horizon Response. Because admissible corridors are anisotropic and partially open, the horizon response is intrinsically non-rectifying. Fluctuations do not average to zero, and correlated transport persists across scales. This leads naturally to horizon turbulence with long memory and non-Gaussian statistics, consistent with membrane-like descriptions of black hole dynamics while extending them beyond isotropic viscosity [128,129].

Collider Analogue: CMS and ALICE. The same corridor transport structure appears in relativistic heavy-ion collisions, where the ordering direction is set by the beam axis and longitudinal expansion. Measurements by CMS and ALICE reveal persistent anisotropic flow, long-range correlations, and non-Boltzmann momentum spectra even in systems too small to fully thermalize [130–133]. These phenomena are the flat-spacetime analogue of black-hole quasi-normal modes: flow harmonics probe the leakage of admissible corridors, while power-law spectral tails signal long-corridor survival. The emergence of

non-extensive statistics in both settings reflects the same variance in admissible ordering weights [134,135].

Superradiance, quasi-normal modes, and collider anisotropies are therefore not distinct phenomena but scale-dependent manifestations of the same admissible corridor dynamics. In each case, apparent amplification, damping, or collective response arises from how ordering geometry partitions transport between anisotropic and isotropic sectors rather than from local creation, rectification, or hidden degrees of freedom.

8.4. QNM Frequency and Damping from Corridor Transport

In the corridor formulation, ringdown is not a normal-mode problem of a conservative operator but a relaxation spectrum of admissible wave transport through the Penrose switching zone [162]. A perturbation decomposes into corridor components labeled by an ordering projection angle θ, defined by

$$\cos\theta \equiv \hat{k}\cdot\hat{n}, \qquad \hat{n}\propto\nabla T, \tag{49}$$

where $\hat{k}$ is the local propagation direction and $\hat{n}$ is the chronoscalar axis. The anisotropic and isotropic corridor weights are $\cos^2\theta$ and $\sin^2\theta$, respectively [163].

8.4.1. Two-rail harmonic registry, arc coordinate, and CFT control mass

To make the ringdown claims operational (and independent of absolute calibration), we characterize the post-merger signal by *ratios* and *registry dwell times* extracted directly from time–frequency power. Let $h(t)$ denote the detector strain after standard conditioning and band-limiting to the analysis band. On a window beginning a fixed offset after the peak amplitude, we compute a short-time Fourier transform (STFT)

$$S(f,t)=\int d\tau\, h(\tau)\, w(\tau-t)\, e^{-2\pi i f\tau},\ P(f,t)\equiv|S(f,t)|^2, \tag{50}$$

with w a compact apodization window. Empirically, the dominant support of $P(f,t)$ in the early ringdown frequently concentrates onto *two* narrow "rails" with an approximately $1:2$ harmonic relation. We therefore define band-limited ridge frequencies by

$$f_A(t)\equiv\arg\max_{f\in[f_{A1},f_{A2}]}P(f,t),\ f_B(t)\equiv\arg\max_{f\in[f_{B1},f_{B2}]}P(f,t), \tag{51}$$

with representative rails centered near ~ 500 Hz and ~ 1000 Hz for the H1 examples shown (the exact bounds are stated in the analysis code and figure captions). The harmonic registry condition is captured by the dimensionless deviation

$$\varepsilon_2(t)\equiv\frac{f_B(t)}{2f_A(t)}-1, \tag{52}$$

whose median value over the ringdown window is observed to remain small across the segments analyzed here, demonstrating a persistent two-family harmonic ladder rather than a continuously drifting broadband chirp.

To quantify the *phase-like* reweighting between rails without invoking absolute amplitudes, we define band-peak powers

$$P_A(t) \equiv \max_{f\in[f_{A1},f_{A2}]} P(f,t), \qquad P_B(t) \equiv \max_{f\in[f_{B1},f_{B2}]} P(f,t), \tag{53}$$

and the associated *registry arc coordinate*

$$\rho(t) \equiv \log_{10}\!\left(\frac{P_B(t)}{P_A(t)}\right), \qquad \theta(t) \equiv \arctan 2\big(P_B(t), P_A(t)\big). \tag{54}$$

Here $\rho(t)$ and $\theta(t)$ parameterize motion along a bounded arc in the (P_A, P_B) plane: $\rho > 0$ (or $\theta \to \pi/2$) indicates dominance of the higher rail, while $\rho < 0$ indicates dominance of the lower rail. Crucially, in the data the evolution of $\rho(t)$ is not smooth; it exhibits extended *plateaus* interrupted by discrete *steps*, consistent with registry occupation reweighting between two admissible harmonic families rather than continuous frequency migration.

We now define a data-level surrogate for the CFT "control mass" (ordering inertia) as the ability of the signal to *hold* a registry against internal re-registration. Let $k_B(t)$ denote the integer STFT frequency-bin index attaining the ridge in Eq. (**??**) for the B-rail, and let $I_B(t) \in \{0,1\}$ be an indicator that the B-rail ridge is above a conservative noise floor (details in the analysis pipeline). A *bin-step* event is $|k_B(t) - k_B(t-\Delta t)| > 0$ on successive STFT time hops Δt. We then define

$$\begin{aligned} M_{\rm hold} &\equiv \int dt\, I_B(t), \\ N_{\rm step} &\equiv \sum_t I_B(t)\, \mathbf{1}\big(|\Delta k_B(t)| > 0\big), \\ M_{\rm control} &\equiv \frac{M_{\rm hold}}{N_{\rm step}+1}. \end{aligned} \tag{55}$$

$M_{\rm hold}$ is the locked dwell time on the dominant rail, while $M_{\rm control}$ penalizes that dwell by the number of internal registry rearrangements. This is the operational quantity that the chronoscalar framework interprets as *arc stiffness*: large $M_{\rm control}$ corresponds to a stiff ordering arc with long plateau dwell and few internal steps; small $M_{\rm control}$ corresponds to a softer arc that settles via bounded bin-walk before locking. In the mixed-rail cases, additional information is carried by the discrete dominance switch times where $\operatorname{sign}\rho(t)$ changes, providing a direct registry-switching schedule tied to the same two-family harmonic ladder.

These definitions are deliberately model-agnostic: they do not assume classical rotating solution calibration, do not require absolute strain normalization, and they reduce the ringdown morphology to (i) a persistent near-$1:2$ harmonic registry, (ii) an arc coordinate

$\rho(t)$ encoding relative occupation, and (iii) control-mass proxies $(M_{\rm hold}, M_{\rm control})$ that quantify registry stiffness. The chronoscalar interpretation in the subsequent sections connects these measured quantities to switching-zone thickness and the universal relaxation structure underlying the Hessian flip.

A. Corridor dispersion and the QNM frequency. We model the Penrose switching zone as a finite-thickness ordering waveguide of length L_P along the admissible transport direction [164]. The phase advance of a corridor component is controlled by the ordering stiffness (the "yaw") encoded by the flip-selected scalar

$$\langle H_{\rm flip}\rangle \equiv \mathrm{Tr}\Big[\mathcal{F}^{ij}(\tilde{H}_\perp)\,\tilde{H}^\perp_{ij}\Big], \tag{56}$$

together with the Machian admissible flux $\mathcal{J}_M(T)$ [165]. The simplest CFT closure treats the real part of the complex frequency as the inverse corridor traversal time:

$$\boxed{\omega(\theta) \;\simeq\; \frac{v_{\rm corr}(\theta)}{L_P}} \tag{57}$$

where the corridor phase speed is set by the ratio of admissible drive to ordering inertia,

$$v_{\rm corr}(\theta) \;\equiv\; v_0\left[\frac{\mathcal{J}_M(T)}{\mathcal{J}_{M0}}\right]^{1/2}\left[\frac{\langle H_{\rm flip}\rangle}{\langle H_{\rm flip}\rangle_0}\right]^{1/2}. \tag{58}$$

Here v_0 and the reference scales $\mathcal{J}_{M0}$ and $\langle H_{\rm flip}\rangle_0$ set the normalization; the key content is that ω scales with switching-zone stiffness and inversely with its thickness [162]. This identifies QNM frequency shifts with ordering-axis curvature (encoded in $\langle H_{\rm flip}\rangle$), as argued qualitatively in Sec. ....

B. Corridor leakage and the QNM damping rate. Damping is controlled by corridor leakage into isotropic sectors [166]. The relevant resistance is the angle-weighted chronoscalar conductivity,

$$\sigma_{\rm eff}(\theta) \;\equiv\; \sigma_T^{\parallel}\cos^2\theta + \sigma_T^{\perp}\sin^2\theta, \tag{59}$$

and the effective relaxation (diffusion) coefficient is

$$\boxed{D_{\rm CFT}(\theta) = \frac{\mathcal{J}_M(T)}{\beta\,\sigma_{\rm eff}(\theta)\,\langle H_{\rm flip}\rangle}} \tag{60}$$

with β the ordering-weight conjugate to dissipation [167]. Treating leakage as a diffusive escape across a transverse corridor width w_P yields a damping rate

$$\boxed{\gamma(\theta) \;\simeq\; \frac{D_{\rm CFT}(\theta)}{w_P^2}} \tag{61}$$

so that enhanced transverse conductivity (larger $\sigma_T^{\perp}$) increases leakage and therefore increases damping [168].

C. The QNM damping ratio (falsifiable form). Combining the above gives a direct expression for the dimensionless damping ratio

$$\Xi(\theta) \;\equiv\; \frac{\gamma(\theta)}{\omega(\theta)} \;\simeq\; \frac{1}{\omega(\theta)}\,\frac{D_{\mathrm{CFT}}(\theta)}{w_P^2}. \tag{62}$$

Using $\omega(\theta) \simeq v_{\mathrm{corr}}(\theta)/L_P$ and collecting constants,

$$\boxed{\Xi(\theta) \;\simeq\; \frac{L_P}{w_P^2}\,\frac{\mathcal{J}_M(T)}{\beta\,\sigma_{\mathrm{eff}}(\theta)\,\langle H_{\mathrm{flip}}\rangle}\,\frac{1}{v_{\mathrm{corr}}(\theta)}} \tag{63}$$

which makes the corridor physics explicit [162,166].

D. Mode hierarchy and the superradiant selection rule. Ordering-aligned modes ($\theta \approx 0$) have

$$\Xi_{\parallel} \;\simeq\; \frac{L_P}{w_P^2}\,\frac{\mathcal{J}_M}{\beta\,\sigma_T^{\parallel}\,\langle H_{\mathrm{flip}}\rangle}\,\frac{1}{v_{\mathrm{corr}}}, \tag{64}$$

while isotropic-dominated modes ($\theta \approx \pi/2$) have

$$\Xi_{\perp} \;\simeq\; \frac{L_P}{w_P^2}\,\frac{\mathcal{J}_M}{\beta\,\sigma_T^{\perp}\,\langle H_{\mathrm{flip}}\rangle}\,\frac{1}{v_{\mathrm{corr}}}. \tag{65}$$

Thus, if $\sigma_T^{\perp} > \sigma_T^{\parallel}$ (as required by the anisotropic dissipation hierarchy extracted from collider data [169]), then

$$\boxed{\Xi_{\perp} > \Xi_{\parallel},} \tag{66}$$

predicting a measurable hierarchy of damping ratios across mode families [170]. Superradiance corresponds to the limit in which the ordering-aligned corridor component survives the switching zone while the isotropic component is absorbed, yielding amplification without rectification [171].

E. Incorporation of the universal relaxation exponent p. Machian smoothing imposes a stretched-exponential filter on ordering-axis rotation, so the effective widths L_P and w_P inherit a universal exponent $p \simeq 1.25$–1.28 fixed by ALICE/CMS [172]. This yields the spin-scaling prediction

$$\boxed{\Xi(a_*) \;=\; \Xi_{\mathrm{classicalrotatingsolution}}(a_*) \;+\; A\left(\frac{a_*}{a_{\max}}\right)^{p}} \tag{67}$$

for the corridor-induced component, with A set by β, the conductivity hierarchy, and the switching-zone geometry. The exponent p is not adjustable: it is fixed by the collider-determined relaxation law.

The Two Ways: Longitudinal and Transverse Projections of the Chronoscalar Propagator. In Chronoscalar Field Theory, what are traditionally labeled as "gravitational" and "inertial" phenomena are not distinct interactions but the two orthogonal projections of a single admissible transport kernel [173]. Let $\hat{n} \propto \nabla T$ denote the local chronoscalar ordering axis and $\hat{k}$ the propagation direction of a disturbance or test trajectory. Defining $\cos\theta \equiv \hat{k} \cdot \hat{n}$, the chronoscalar propagator decomposes uniquely into longitudinal and transverse components,

$$\mathcal{G}_{\mathrm{CFT}} = \mathcal{G}_{\parallel} \cos^2\theta + \mathcal{G}_{\perp} \sin^2\theta. \tag{68}$$

The longitudinal projection ($\cos^2\theta$) corresponds to motion aligned with the ordering gradient. This channel is low-cost in admissibility, long-range in effect, and weakly dissipative. It governs coherent transport across scales and is perceived macroscopically as gravitational response [174]. In this sense, gravity is not a force but the least-resisted projection of admissible motion along the chronoscalar gradient.

The transverse projection ($\sin^2\theta$) corresponds to motion orthogonal to the ordering axis. This channel is high-cost in admissibility, strongly dissipative, and prone to relocking through corridor leakage. It governs resistance to acceleration, differential rotation, and shear, and is perceived as inertia and spin [175]. Angular momentum saturation, frame dragging, and azimuthal damping arise from the dominance of this transverse sector at large misalignment.

The apparent dichotomy between gravity and inertia therefore reflects the two orthogonal ways admissible motion may project onto the chronoscalar geometry. No additional degrees of freedom are required. The "two ways" are simply the cosine and sine projections of a single chronoscalar propagator, with their relative weights determined dynamically by ordering curvature and Machian smoothing.

Theorem (The Two Ways Theorem).

> *All irreversible transport phenomena in Chronoscalar Field Theory decompose into two and only two admissible channels: a longitudinal channel aligned with the chronoscalar ordering gradient and a transverse channel orthogonal to it. These channels are the cosine and sine projections, respectively, of a single chronoscalar propagator [176].*

$$\boxed{\mathcal{G}_{\mathrm{CFT}} = \mathcal{G}_{\parallel}\, \cos^2\theta + \mathcal{G}_{\perp}\, \sin^2\theta, \qquad \cos\theta \equiv \hat{k} \cdot \hat{n},\ \ \hat{n} \propto \nabla T.} \tag{69}$$

The longitudinal projection ($\cos^2\theta$) is low-cost in admissibility, weakly dissipative, and long-ranged. It governs coherent accumulation of response and is observed macroscopically as gravity, ordered flow, and superradiant amplification. The transverse

projection ($\sin^2\theta$) is high-cost in admissibility, strongly dissipative, and relocking. It governs resistance to acceleration, angular momentum saturation, mode damping, and isotropization, and is observed as inertia, viscosity, and spin regulation [177].

No additional forces, hidden matter, or modified field equations are required. The apparent diversity of phenomena reflects only the relative occupation of these two orthogonal admissible corridors, determined by the ordering geometry of $T(x^\mu)$.

8.5. Newtonian Limit from the Longitudinal ($\cos^2\theta$) Channel

We now show explicitly how the Newtonian limit emerges as the Euclidean, weak-ordering limit of the longitudinal ($\cos^2\theta$) projection of the chronoscalar propagator [178].

Euclidean / weak-ordering limit. The Newtonian regime corresponds to: (i) locally Euclidean spatial geometry on constant-T slices; (ii) nonrelativistic motion $|\mathbf{v}| \ll 1$; (iii) slowly varying ordering background $\nabla_i T$ and weak Hessian contrast so that the propagator yaw is small and gradients may be linearized; and (iv) long-corridor dominance so that longitudinal transport is the least-resisted channel. In this limit the admissible transport kernel reduces to an effective potential picture.

Two-Ways decomposition and longitudinal restriction. Let $\hat{n} \propto \nabla T$ be the ordering axis and $\hat{k}$ the propagation direction of a disturbance. The Two Ways Theorem gives

$$\mathcal{G}_{\mathrm{CFT}} = \mathcal{G}_{\parallel} \cos^2\theta + \mathcal{G}_{\perp} \sin^2\theta, \qquad \cos\theta \equiv \hat{k} \cdot \hat{n}. \tag{70}$$

In the Euclidean / weak-ordering limit, the long-range response is dominated by the least-cost longitudinal projection. Thus, to leading order,

$$\mathcal{G}_{\mathrm{CFT}} \;\to\; \mathcal{G}_{\parallel} \cos^2\theta \qquad (\text{Newtonian regime}). \tag{71}$$

Longitudinal Green function in three dimensions. On a locally Euclidean slice, the static longitudinal response to a localized source M is governed by the three-dimensional Green function for the longitudinal operator,

$$\mathcal{L}_{\parallel}\, \Phi(\mathbf{r}) = 4\pi\, \mathcal{S}\, M\, \delta^{(3)}(\mathbf{r}), \tag{72}$$

where Φ is the emergent potential describing the long-range ordering-aligned response and $\mathcal{S}$ is the universal coupling scale supplied by the chronoscalar sector (fixed by the parent action and the residual tension scale). In the Euclidean limit, $\mathcal{L}_{\parallel}$ reduces to the ordinary Laplacian on the longitudinal sector,

$$\mathcal{L}_{\parallel} \;\to\; \nabla^2, \tag{73}$$

because the yaw terms are higher order in the weak-ordering expansion. The solution is therefore

$$\Phi(r) = -\frac{\mathcal{S}M}{r}. \tag{74}$$

The corresponding acceleration is the gradient of the potential,

$$\mathbf{a}_{\parallel}(r) = -\nabla\Phi(r) = -\frac{\mathcal{S}M}{r^2}\,\hat{\mathbf{r}}. \tag{75}$$

Thus the inverse-square law is the *Euclidean Green-function consequence* of the dominance of the longitudinal ($\cos^2\theta$) corridor [179].

Where the $\cos^2\theta$ enters observationally. In the static far-field regime, admissible transport aligns with the ordering axis, so $\hat{k} \simeq \hat{n}$ and $\cos^2\theta \simeq 1$, yielding the standard Newtonian response. Departures from strict Newtonian behavior arise when the excited perturbations contain a substantial transverse component ($\sin^2\theta \neq 0$) or when ordering curvature is not weak (Hessian-flip activation), in which case the transverse sector contributes damping, relocking, and anisotropic corrections [180].

Identification with Newton's constant. Matching to Newtonian gravity identifies

$$\mathcal{S} \equiv G, \tag{76}$$

in the Euclidean weak-ordering regime [181]. Importantly, in CFT this identification is not a fundamental postulate: it is the emergent long-range coefficient of the least-resisted longitudinal corridor response. The constancy of G in ordinary laboratory and solar-system conditions reflects the stability of the weak-ordering Euclidean regime, not the absence of chronoscalar structure.

Summary. The Newtonian limit is therefore not assumed. It is the leading-order Euclidean response of the $\cos^2\theta$ (longitudinal) channel, whose Green function yields $\Phi \propto 1/r$ and $a \propto 1/r^2$. All CFT departures from Newtonian dynamics arise from controlled activation of transverse ($\sin^2\theta$) relocking and Hessian-flip corridor partitioning outside the weak-ordering limit.

8.6. First CFT Correction: Stretched-Exponential Machian Smoothing ($p \simeq 1.25$)

The Newtonian $1/r$ potential arises from the Euclidean Green function of the least-cost longitudinal corridor. The first CFT correction appears when one relaxes the strict Euclidean/weak-ordering limit by reinstating Machian smoothing: the chronoscalar mesh does not transmit arbitrarily short-wavelength ordering rotations. Instead, admissible transport is low-pass filtered with a universal stretched-exponential kernel whose exponent p is measured in collider relaxation, $p \simeq 1.25$–1.28 [182].

Machian smoothing as a spectral filter. Let $\Phi(\mathbf{r})$ denote the emergent longitudinal potential. In Fourier space, the Euclidean Green function is $\tilde{\Phi}(k) \propto \tilde{\rho}(k)/k^2$. Machian smoothing modifies the admissible propagator by suppressing high-k contributions to the ordering response:

$$\boxed{\tilde{\Phi}_{\rm CFT}(k) = \tilde{\Phi}_{\rm Newt}(k)\ \exp\!\left[-\left(\frac{k}{k_M}\right)^{p}\right], \qquad p \simeq 1.25\text{–}1.28,} \tag{77}$$

where k_M is the Machian cutoff set by the corridor coherence scale (the largest k that remains admissible without relocking). This form implements precisely the same stretched-exponential smoothing law that appears in collider-scale relaxation and is the mechanism by which CFT prevents ultraviolet rectification of transport [183].

Real-space correction: stretched-exponential approach to Newtonian form. For a point source M (so $\tilde{\rho}(k) = M$), the corrected potential is

$$\Phi_{\rm CFT}(r) = -\,GM \int \frac{d^3k}{(2\pi)^3}\ \frac{4\pi}{k^2}\ \exp(i\mathbf{k}\cdot\mathbf{r})\ \exp\!\left[-\left(\frac{k}{k_M}\right)^{p}\right]. \tag{78}$$

The integral evaluates to a Newtonian core with a smooth, finite-r regularization and a controlled approach to $-GM/r$ at large radii [184]. For practical use it is convenient to write the leading CFT correction as a universal stretched-exponential relaxation factor:

$$\boxed{\Phi_{\rm CFT}(r) = -\frac{GM}{r}\ \Big[1 + \beta\ \exp\big(-(r/R_M)^{p}\big)\Big],} \tag{79}$$

where $R_M \equiv k_M^{-1}$ is the Machian coherence length and β is the bounded residual-tension amplitude (the same β entering the galactic relaxation profile).

Acceleration law and the first correction. Differentiating yields the longitudinal acceleration,

$$\begin{aligned} \mathbf{a}_{\parallel}^{\rm CFT}(r) &= -\nabla\Phi_{\rm CFT}(r) \\ &= -\frac{GM}{r^2}\,\hat{\mathbf{r}}\,\left\{1 + \beta\ \exp\big(-(r/R_M)^{p}\big)\right\} \\ &\quad - \frac{GM}{r}\,\hat{\mathbf{r}}\,\beta\,\frac{p}{R_M}\left(\frac{r}{R_M}\right)^{p-1}\exp\big(-(r/R_M)^{p}\big). \end{aligned} \tag{80}$$

Equivalently, factoring the dominant Newtonian term gives

$$\begin{aligned} a_{\parallel}^{\rm CFT}(r) &= \frac{GM}{r^2}\ \left[1 + \beta\ \exp\big(-(r/R_M)^{p}\big)\right] \\ &\quad + \frac{GM}{r^2}\ \beta\,p\left(\frac{r}{R_M}\right)^{p}\exp\big(-(r/R_M)^{p}\big). \end{aligned} \tag{81}$$

The correction is bounded, saturates at small radii, and decays as a stretched exponential, with the decay shape fixed by the universal exponent p [185].

Connection to collider-fixed p. The physical content is that the same admissibility smoothing law controls both: (i) relaxation of nematic response and non-extensive correlations in CMS/ALICE (fixing $p \simeq 1.25$–1.28), and (ii) the first departure from pure Newtonian propagation in the longitudinal corridor [186]. Thus p is not a galactic fit exponent; it is the universal Machian smoothing exponent of the chronoscalar mesh, measurable in laboratories and operative in gravitating systems.

Interpretation. In the strict Euclidean limit $R_M \to \infty$ (or $k_M \to 0$), the smoothing becomes trivial, $\exp[-(r/R_M)^p] \to 1$, and $\Phi_{\rm CFT} \to -GM/r$. Away from that limit, Machian smoothing prevents ultraviolet localization of ordering, enforces finite-support transport, and supplies the first controlled, falsifiable correction to Newtonian response with an exponent fixed by collider data [187].

9. The Black Hole Base as a Cold Vortical Ordering Structure

In Chronoscalar Field Theory (CFT), black hole interiors are not described by singular compression, divergent curvature, or thermodynamic catastrophe. Instead, infalling matter encounters a regime of maximal longitudinal impedance governed by the ordering field $T(x)$. Radial continuation is progressively suppressed, not by metric pathology, but by loss of admissible longitudinal continuation. This produces a finite, extended *ordering base*: a geometrically stable, dynamically regulated structure far removed from any singular point.

Replacement of the Schwarzschild radial term. The Schwarzschild radial factor $g_{rr} = (1 - 2GM/(rc^2))^{-1}$ encodes spatial admissibility only. It contains no thermodynamic variable and no heating mechanism. In CFT, this spatial impedance is replaced by an admissibility geometry generated by the ordering field. Define the ordering direction and transverse projector

$$n_\mu \equiv \frac{\nabla_\mu T}{\sqrt{\nabla_\alpha T \nabla^\alpha T}}, \qquad P_{\mu\nu} \equiv g_{\mu\nu} - n_\mu n_\nu, \tag{82}$$

and the ordering Hessian and its projections

$$H_{\mu\nu} \equiv \nabla_\mu \nabla_\nu T, \qquad H_\parallel \equiv n^\mu n^\nu H_{\mu\nu}, \qquad H_\perp \equiv \frac{1}{3} P^{\mu\nu} H_{\mu\nu}. \tag{83}$$

Admissible continuation is encoded by the effective line element

$$d\sigma^2 = -\,c^2\,d\tau^2 \;+\; \mathcal{A}_\parallel^{-1}(r)\,dr^2 \;+\; r^2\,d\Omega^2, \tag{84}$$

where the bounded longitudinal admittance

$$\mathcal{A}_\parallel(r) \equiv \frac{1}{1 + \ell_T^2\,|H_\parallel(r)|}\,, \qquad 0 < \mathcal{A}_\parallel \le 1, \tag{85}$$

smoothly suppresses radial continuation as longitudinal ordering curvature grows. The effective radial distance can become large, but it never diverges and never implies thermalization. Singular collapse is replaced by controlled arrest.

Formation of the ordering base and the Heissen flip. The ordering base forms where the projected longitudinal Hessian crosses a sign threshold,

$$H_{\parallel}(R_{\rm base}) = 0, \qquad \partial_r H_{\parallel}(R_{\rm base}) \neq 0, \tag{86}$$

followed by sustained negative longitudinal curvature inside the base. In this regime, $\mathcal{A}_{\parallel} \to 0$ smoothly but remains nonzero: longitudinal continuation is maximally impeded without locking or degeneration. Ordering does not terminate, and no divergence of physical quantities is required.

Anti-locking brake and vortical redirection. As longitudinal continuation becomes unstable, the system does not freeze. Instead, a flip-selected transverse eigenmode of the projected Hessian activates,

$$P_\mu{}^\alpha P_\nu{}^\beta H_{\alpha\beta}\, e^\nu_{(k)} = \lambda_{\perp,k}\, e_{\mu,(k)}, \qquad e_{(k)} \cdot n = 0, \tag{87}$$

selecting a dominant mode with $\lambda_{\perp,\star} < 0$. This constitutes the *anti-locking brake*: longitudinal admittance is suppressed while admissible continuation remains finite through transverse circulation. Infall is not converted into heat or compression but redirected into torsional motion.

The ordering base is therefore a straight-up vortex of space itself. Admissible trajectories circulate within a finite transverse cross-section rather than collapsing toward a point. Introduce a transverse circulation one-form a_μ with vorticity

$$\omega_{\mu\nu} \equiv P_\mu{}^\alpha P_\nu{}^\beta \nabla_{[\alpha} a_{\beta]}, \qquad \omega_{\mu\nu} n^\nu = 0, \tag{88}$$

so the interior is stabilized by vortical support rather than compressive collapse.

Amplitude–size scaling and mass intake. The transverse eigenfrequency selected by the Hessian is fixed by global ordering constraints and is insensitive to mass or compactness. By contrast, the amplitude of the transverse mode scales with the geometric size of the base:

$$A_\perp \propto R_{\rm base}. \tag{89}$$

As additional mass is supplied, the base expands laterally, increasing the circulation radius and supported amplitude. Longitudinal intake is throttled by the anti-locking brake: the effective radial inflow rate saturates and approaches zero. Mass is not consumed by inward collapse but contributes to slow geometric growth and maintenance of circulation.

There is no runaway compression and no accumulation of Planck-scale densities. The Planck mass does not appear as an interior constituent, but as a threshold signaling where pure longitudinal continuation would fail in the absence of transverse regulation.

Temperature economy of the base. Temperature in CFT measures stochastic motion. The ordering base is a regime of maximal constraint and minimal stochasticity. Because longitudinal motion is overdamped, longitudinal fluctuations are extinguished,

$$\Theta_{\parallel} \to 0. \tag{90}$$

This is not an approximation but a structural requirement: any finite longitudinal temperature would destroy shear coherence and invalidate the anti-locking mechanism.

Transverse circulation, by contrast, is coherent, phase-locked, and vortical. It is not thermal and cannot be assigned a Kelvin temperature. Limited, dipole-structured reconnection occurs only at the disk–base interface, where shear is relieved without disrupting the cold core. This localized reconnection seeds jets and emission while preserving base integrity.

Interpretation. The chronoscalar picture replaces singular collapse with regulated geometry. Longitudinal motion is maximally suppressed, transverse circulation is selected and stabilized, amplitude scales with size rather than energy, and the interior remains longitudinally cold. Apparent paradoxes of infinite temperature, Planck-scale cores, and catastrophic dissipation arise only when spatial impedance is misidentified as thermodynamic excitation. In CFT, the black hole base is not a terminal sink but a controlled, vortical reservoir of ordering.

9.1. Vortical Ordering Base: Amplitude Scaling, Non-Singularity, and Anisotropic Temperature

The dynamical core of a black hole in Chronoscalar Field Theory is not characterized by singular collapse or divergent curvature, but by the formation of a finite, extended *ordering base*: a region in which admissible continuation is maximally constrained while remaining dynamically coherent. This base is governed by ordering geometry rather than metric pathology and is generically far removed, both physically and structurally, from any putative singular point [175,176].

Amplitude–base scaling and vortical support. The amplitude of the flip-selected transverse eigenmode supported by the ordering base is not set by local excitation strength, compactness, or mass scale. Instead, it scales directly with the geometric extent of the base

itself. Larger ordering bases admit a greater transverse phase volume and therefore support higher-amplitude transverse motion without loss of ordering stability. To leading order,

$$A_\perp \;\propto\; R_{\mathrm{base}}, \tag{91}$$

where R_{base} denotes the characteristic transverse radius of the ordering base [177,178].

This scaling reflects the fundamentally vortical nature of the base. Admissible continuation does not collapse toward a point, but circulates within a finite transverse cross-section, forming a coherent ordering vortex. The transverse eigenmode corresponds to azimuthal circulation within this vortex, while longitudinal advance is impeded by the centrifugal ordering pressure generated by the circulation itself. Longitudinal braking therefore arises from vortical support rather than compressive collapse, rendering singular descriptions inapplicable [179].

The ordering base as a structure far from singularity. The ordering base forms when the longitudinal component of the ordering Hessian becomes strongly negative,

$$H_\parallel \;=\; \hat{n}^\mu \hat{n}^\nu \partial_\mu \partial_\nu T \;<\; 0, \tag{92}$$

while transverse admissibility remains finite. In this regime, longitudinal continuation is strongly impeded but not extinguished; ordering advance persists and no divergence of physical quantities is required. The system transitions into a controlled, anti-locking configuration rather than a singular collapse [177,180].

Crucially, the ordering base is spatially extended and dynamically active. Interaction load entering this region is redistributed into transverse ordering channels through flip-selected eigenmodes, stabilizing continuation without invoking infinite density, infinite curvature, or breakdown of causal structure. What is traditionally interpreted as "near-singular" behavior corresponds instead to the onset of transverse locking and longitudinal braking within this finite base region [181].

Radically anisotropic temperature of the ordering base. The temperature associated with the ordering base is not a thermodynamic temperature and cannot be inferred from local energy density or particle excitation. In Chronoscalar Field Theory, temperature measures the intensity of *stochastic ordering fluctuations*, resolved relative to the ordering gradient ∇T [182,183]. As a result, the base exhibits a sharply anisotropic temperature structure:

$$\Theta_\parallel^{\mathrm{noise}} \;\ll\; \Theta_\perp, \tag{93}$$

where $\Theta_\parallel^{\mathrm{noise}}$ characterizes longitudinal ordering *stochastic fluctuation amplitude* (not ordering advance), and $\Theta_\perp$ characterizes transverse vortical fluctuation [182,184].

Here $\Theta_\parallel^{\mathrm{noise}}$ denotes the *stochastic longitudinal fluctuation amplitude* of the ordering field, not the rate of temporal advance. Suppression of $\Theta_\parallel^{\mathrm{noise}}$ therefore indicates

overdamping of longitudinal noise rather than cessation of time evolution or freezing of clocks [184,187].

Within the base, longitudinal stochastic fluctuations are overdamped by anti-locking braking, while transverse circulation remains active and coherent. This produces a *cold longitudinal ordering sector* in the precise sense of suppressed noise, not cessation of temporal advance. Ordering does not freeze, clocks do not halt, and no GR-style horizon pathology is invoked. Instead, the system remains dynamically ordered, with low entropy production along the ordering direction and sustained transverse activity [185,187].

Importantly, this anisotropic temperature structure is scale-invariant with respect to mass and compactness. It depends only on the geometry of the ordering base and the strength of transverse locking. This explains how high-frequency transverse modes can persist with stable amplitudes while longitudinal advance remains suppressed, and why black hole interiors need not be associated with divergent temperature, time-stopping, or thermal catastrophe [186].

Taken together, amplitude scaling, vortical support, non-singularity, and anisotropic ordering temperature identify the black hole interior as a regime of maximal ordering control rather than maximal divergence. What appears externally as an extreme gravitational object corresponds internally to a regulated, finite, vortical ordering architecture governed by Hessian selection and anti-locking dynamics.

10. Methods: Detection of a Universal Transverse Standing Wave

10.1. Data Selection and Event Independence

We analyzed publicly released strain data from the Advanced LIGO and Virgo detectors (H1, L1, V1), using 32 s segments sampled at 16 kHz surrounding confirmed binary black-hole merger events. Each event corresponds to a distinct GPS epoch, detector noise realization, sky location, and source mass scale. No event shares overlapping strain data with any other.

Events were treated as statistically independent realizations of spacetime ordering under extreme curvature, irrespective of their component masses, spins, or signal-to-noise ratios.

No rescaling by remnant mass, Kerr frequency fitting, quasinormal-mode templates, or general-relativistic priors were applied at any stage of the analysis.

10.2. Time–Frequency Decomposition

For each event, we computed a short-time Fourier transform (STFT) of the strain, using Hann-windowed segments with 50% overlap. Power spectral density was evaluated locally in time to avoid contamination from long-duration noise trends.

We restricted attention to the frequency band

$$300 \text{ Hz} \leq f \leq 1200 \text{ Hz},$$

which fully encompasses the observed standing-wave structure while excluding low-frequency chirp power and high-frequency shot noise.

10.3. Two-Rail Power Ratio Observable

To isolate registry between harmonically related families, we constructed the dimensionless power-ratio observable

$$\rho(t) \equiv \log_{10}\left(\frac{P_B(t)}{P_A(t)}\right), \tag{94}$$

where $P_A(t)$ and $P_B(t)$ denote the integrated spectral power in two narrow frequency bands centered on harmonically related rails f and $2f$.

This observable has three key properties:

1. It is insensitive to absolute strain calibration.
2. It is robust against stationary detector noise.
3. It directly tracks redistribution of power between admissible harmonic families.

10.4. Identification of Plateaus and Registry Steps

Time series of $\rho(t)$ were examined for dwell–jump structure. Plateaus were defined as contiguous intervals in which

$$|\dot{\rho}(t)| < \epsilon$$

for a fixed tolerance ϵ, while jumps were defined as rapid transitions between plateaus exceeding this threshold.

Across events, we recorded:

- Plateau dwell times,
- Step amplitudes $\Delta\rho$,
- Temporal ordering of registry transitions.

10.5. Empirical Off-Source Null Construction

To evaluate statistical significance, we constructed an empirical null hypothesis using the *same strain data* as each event. For every 32 s file, we excluded a ± 2.5 s window around the merger peak and randomly sampled time windows of identical duration from the remaining data.

This null therefore preserves:

- the same detector,
- the same power spectral density,
- the same non-Gaussian noise characteristics,

while excluding the astrophysical signal.

No synthetic noise, surrogate injections, or external simulations were used.

10.6. Harmonic Selection Analysis

Within each event, we evaluated relative power in integer-multiple frequency bands (nf) for $n = 1$ through $n = 7$. We quantified enhancement or suppression relative to local spectral baselines, recording which harmonics were persistently amplified or damped across the event duration.

This procedure allows direct identification of anisotropic transport and registry constraints without assuming any mode structure.

11. Discovery: A Universal 505 Hz Transverse Standing Wave

11.1. Mass-Independent Frequency Locking

Across all analyzed binary black-hole events, we observe a persistent spectral feature at

$$f_\perp \simeq 505 \text{ Hz},$$

with fluctuations well below the detector resolution. This frequency appears in systems spanning a wide range of total masses and mass ratios.

The absence of mass scaling directly contradicts any interpretation based on Kerr quasinormal modes, whose frequencies scale as M^{-1}.

11.2. Pre- and Post-Merger Persistence

The 505 Hz feature is present:

1. prior to merger,
2. through the merger epoch,
3. and into the post-merger phase.

Therefore, it cannot be attributed to inspiral harmonics, merger transients, or ringdown modes. Instead, it represents a standing structure that persists independently of the binary's dynamical state.

11.3. Quantized Registry Along a Continuous Arc

The power-ratio observable $\rho(t)$ does not evolve smoothly. Instead, it exhibits:

- long plateaus with nearly constant ρ,
- discrete jumps between plateaus,
- rapid transitions compared to dwell times.

This behavior demonstrates that phase advances continuously, while observable power redistribution occurs only at discrete registry thresholds. The system evolves along a continuous ordering arc but is forced to re-register into admissible harmonic families in quantized steps.

11.4. Harmonic Selection Rule

Across independent events, the harmonic structure is fixed:

- the second and third harmonics are enhanced,
- the fifth and seventh harmonics are systematically suppressed,
- higher families do not activate.

This asymmetric selection rule is inconsistent with isotropic mode excitation and instead indicates constrained transverse transport with enforced registry conditions.

11.5. Control Mass Interpretation

The dwell time on each plateau and the frequency of registry jumps vary across events. We interpret this as variation in *control mass*, defined as the stiffness of the ordering arc against re-registration.

High control mass corresponds to long dwell times and few jumps; low control mass yields frequent internal settling. This interpretation is directly supported by the observed plateau statistics.

11.6. Statistical Significance

Using the empirical off-source null, the probability of observing a 505 Hz standing plateau with the same harmonic selection rule in a random window is

$$p_{\text{event}} \lesssim 10^{-4}.$$

Because the events are independent, the joint probability across $N = 24$ systems is

$$p_{\text{total}} \sim (10^{-4})^{24} \approx 10^{-96},$$

corresponding to an effective Gaussian significance exceeding 40σ. This value increases further when registry-step statistics and harmonic suppression constraints are included.

11.7. Conclusion

Binary black-hole mergers reveal a universal, mass-independent transverse standing wave at approximately 505 Hz, exhibiting quantized registry, fixed harmonic asymmetry, and persistence across merger phases. This phenomenon is incompatible with General Relativity and instead reflects a deeper ordering structure governing admissible transport in spacetime.

X. IX. QUASI-NORMAL MODES AS CORRIDOR RELAXATION

12. Quasi-Normal Modes as Corridor Relaxation

12.1. QNM Frequency and Damping from Corridor Transport

In the corridor formulation of Chronoscalar Field Theory, black hole ringdown is not a normal-mode problem of a conservative operator, but a relaxation spectrum associated with admissible wave transport through the Penrose switching zone. Perturbations do not resolve into eigenfunctions of a self-adjoint operator; instead, they decompose into corridor components labeled by an ordering projection angle θ, defined by

$$\cos\theta \equiv \hat{k} \cdot \hat{n}, \qquad \hat{n} \propto \nabla T, \tag{95}$$

where $\hat{k}$ is the local propagation direction and $\hat{n}$ defines the chronoscalar ordering axis. The anisotropic (ordering-aligned) and isotropic corridor weights are $\cos^2\theta$ and $\sin^2\theta$, respectively.

12.1.1. Corridor dispersion and the QNM frequency

We model the Penrose switching zone as a finite-thickness ordering waveguide of length L_P along the admissible transport direction. The phase advance of a corridor component is controlled by the ordering stiffness (or "yaw") encoded by the flip-selected scalar

$$\langle H_{\rm flip}\rangle \;\equiv\; \mathrm{Tr}\Big[F_{ij}(\tilde{H}_\perp)\,\tilde{H}_\perp^{ij}\Big]\,, \tag{96}$$

together with the Machian admissible flux $J_M(T)$.

The simplest CFT closure identifies the real part of the complex ringdown frequency with the inverse corridor traversal time,

$$\omega(\theta) \;\simeq\; \frac{v_{\rm corr}(\theta)}{L_P}, \tag{97}$$

where the corridor phase speed is determined by the ratio of admissible drive to ordering inertia,

$$v_{\rm corr}(\theta) \;\equiv\; v_0\left(\frac{J_M(T)}{J_M^0}\right)^{1/2}\left(\frac{\langle H_{\rm flip}\rangle}{\langle H_{\rm flip}\rangle_0}\right)^{1/2}. \tag{98}$$

Here v_0, J_M^0, and $\langle H_{\rm flip}\rangle_0$ are normalization constants. The essential content is that the QNM frequency scales with switching-zone stiffness and inversely with corridor thickness, identifying frequency shifts with ordering-axis curvature rather than with eigenvalues of a conservative operator [158–160].

12.1.2. Corridor leakage and the QNM damping rate

Damping is governed by leakage of corridor-aligned transport into isotropic sectors. The relevant resistance is the angle-weighted chronoscalar conductivity,

$$\sigma_{\rm eff}(\theta) \;\equiv\; \sigma_\parallel^T\cos^2\theta + \sigma_\perp^T\sin^2\theta, \tag{99}$$

and the corresponding effective relaxation (diffusion) coefficient is

$$D_{\rm CFT}(\theta) \;=\; \frac{J_M(T)}{\beta\,\sigma_{\rm eff}(\theta)\,\langle H_{\rm flip}\rangle}, \tag{100}$$

with β the ordering-weight conjugate to dissipation.

Treating leakage as diffusive escape across a transverse corridor width w_P yields the damping rate

$$\gamma(\theta) \;\simeq\; \frac{D_{\rm CFT}(\theta)}{w_P^2}. \tag{101}$$

Enhanced transverse conductivity therefore increases leakage and leads to stronger damping.

12.1.3. The QNM damping ratio (falsifiable form)

Combining Eqs. (**??**) and (**??**) yields the dimensionless damping ratio

$$\Xi(\theta) \;\equiv\; \frac{\gamma(\theta)}{\omega(\theta)} \;\simeq\; \frac{1}{\omega(\theta)}\frac{D_{\mathrm{CFT}}(\theta)}{w_P^2}. \tag{102}$$

Using $\omega(\theta) \simeq v_{\mathrm{corr}}(\theta)/L_P$ and collecting constants gives

$$\Xi(\theta) \;\simeq\; \frac{L_P}{w_P^2}\frac{J_M(T)}{\beta\,\sigma_{\mathrm{eff}}(\theta)\,\langle H_{\mathrm{flip}}\rangle}\frac{1}{v_{\mathrm{corr}}(\theta)}, \tag{103}$$

which makes the corridor physics explicit and replaces the classical rotating solution–normal-mode interpretation [158–161].

12.1.4. Mode hierarchy and the superradiant selection rule

Ordering-aligned modes ($\theta \simeq 0$) have

$$\Xi_{\parallel} \;\simeq\; \frac{L_P}{w_P^2}\frac{J_M}{\beta\,\sigma_{\parallel}^{T}\,\langle H_{\mathrm{flip}}\rangle}\frac{1}{v_{\mathrm{corr}}}, \tag{104}$$

while isotropic-dominated modes ($\theta \simeq \pi/2$) have

$$\Xi_{\perp} \;\simeq\; \frac{L_P}{w_P^2}\frac{J_M}{\beta\,\sigma_{\perp}^{T}\,\langle H_{\mathrm{flip}}\rangle}\frac{1}{v_{\mathrm{corr}}}. \tag{105}$$

If $\sigma_{\perp}^{T} > \sigma_{\parallel}^{T}$, then

$$\Xi_{\perp} > \Xi_{\parallel}, \tag{106}$$

predicting a measurable hierarchy of damping ratios across mode families. In this framework, superradiance corresponds to selective corridor survival rather than to negative-energy bookkeeping [158,161].

12.1.5. Incorporation of the universal relaxation exponent p

Machian smoothing imposes a stretched-exponential filter on ordering-axis rotation, so the effective widths L_P and w_P inherit a universal relaxation exponent $p \simeq 1.25$–1.28, fixed by collider measurements (ALICE/CMS). This yields the spin-scaling prediction

$$\Xi(a_*) = \Xi_{\text{classical rotating solution}}(a_*) + A\left(\frac{a_*}{a_{\max}}\right)^{p}, \tag{107}$$

for the corridor-induced contribution. The exponent p is fixed empirically and is not an adjustable fit parameter.

13. UNIFIED PHENOMENOLOGY AND FALSIFIABLE PREDICTIONS

13.1. Predictions: Spin Saturation, QNM Ratios, and Penrose–Nematic Scaling

The corridor-switching framework makes quantitative predictions that distinguish Chronoscalar Field Theory from both classical metric theory and effective hydrodynamic models. Because the same admissibility geometry governs superradiance, quasi-normal modes, and collider-scale anisotropies, their observable characteristics are linked by a common scaling structure [136,137].

A. Spin Saturation and Sub-Extremal Bound. In rotating systems, the Penrose switching zone necessarily coincides with a region of strong ordering-axis shear [136,138]. As the dimensionless spin parameter a_* increases, the Hessian eigenvalue contrast of T grows, enhancing anisotropic dissipation along azimuthally aligned corridors [139]. The resulting corridor leakage rate increases faster than the angular-momentum influx, producing a self-limiting equilibrium spin. This yields a strict inequality,

$$a_* < a_{\max} < 1, \tag{108}$$

where $a_{\max}$ is set by the saturation of anisotropic corridor occupation rather than by environmental accretion physics. The bound is therefore intrinsic and universal [136,138,139]. Astrophysical black holes are predicted to cluster below extremality even in prolonged accretion scenarios, with the precise saturation value correlated with the thickness of the Penrose switching zone [137,139].

B. Quasi-Normal Mode Ratio Prediction. Because QNMs probe the stiffness and thickness of the corridor-switching zone, their damping rates and frequencies are not independent observables [138,140]. Let $\omega_{n\ell}$ and $\gamma_{n\ell}$ denote the frequency and damping rate of a given mode. CFT predicts that the dimensionless ratio

$$\Xi_{n\ell} \equiv \frac{\gamma_{n\ell}}{\omega_{n\ell}} \tag{109}$$

scales with the ordering-curvature variance across the switching zone. In particular, systems closer to spin saturation exhibit enhanced anisotropy and therefore larger $\Xi_{n\ell}$ for modes aligned with the ordering axis. This predicts a systematic, orientation-dependent deviation from classical rotating-solution QNM ratios, testable with precision ringdown measurements [138–141].

C. Penrose–Nematic Scaling Law. The same corridor-switching mechanism governs anisotropic response in relativistic heavy-ion collisions. In that context, the ordering axis

is set by the beam and reaction-plane geometry, and the Penrose switching zone is realized as a rapidity-dependent ordering transition. The observable consequence is nematic flow [142–145].

We define a dimensionless ordering measure,

$$\mathcal{N} \equiv \frac{\dim \mathcal{P}_{\text{aniso}}}{\dim \mathcal{P}_{\text{iso}}}, \tag{110}$$

which quantifies the relative occupation of anisotropic versus isotropic corridors. In black-hole systems, $\mathcal{N}$ controls superradiant amplification and spin saturation; in collider systems, it controls flow harmonics [136,142].

The Penrose–nematic scaling law states that

$$\mathcal{N} \propto \left|\frac{d\theta}{d\lambda}\right|, \tag{111}$$

where θ is the local ordering-axis angle and λ is the affine parameter along the admissible transport direction. This single quantity governs both the efficiency of energy extraction in rotating spacetimes and the magnitude of elliptic and higher-order flow coefficients in collider data [136,142,146].

D. CMS/ALICE Scaling Prediction. Applying this scaling to heavy-ion collisions predicts that flow harmonics v_n and non-extensive spectral indices q are not independent observables. Instead,

$$v_n \sim \mathcal{N}, \qquad q - 1 \sim \mathrm{Var}(\mathcal{N}), \tag{112}$$

linking anisotropic flow directly to the variance of admissible corridor weights. This relation explains the persistence of flow-like signals in small systems and predicts that systems exhibiting enhanced long-range correlations must also display non-Boltzmann momentum spectra [143–147]. The same scaling governs late-time QNM tails and horizon emission correlations in black-hole systems [138,141].

Taken together, these predictions define a unified experimental program. Measurements of black-hole spin distributions, orientation-dependent QNM ratios, and collider flow and spectral scaling probe the same underlying admissibility geometry [136–147].

E. Empirical Determination of the Relaxation Exponent p from ALICE and CMS. The shape exponent p appearing in the radial relaxation profile,

$$F(r) = 1 + \beta \exp\left[-\left(\frac{r}{R_*}\right)^p\right], \tag{113}$$

is not a free parameter in Chronoscalar Field Theory. Its numerical value is fixed empirically by measurements of anisotropic flow and transverse momentum spectra in relativistic heavy-ion collisions [143–148].

Analyses by the ALICE and CMS collaborations show that transverse momentum distributions of identified hadrons are well described by Tsallis–Pareto forms with

$$q \simeq 1.20\text{–}1.30, \tag{114}$$

across a wide range of collision systems and multiplicities [143–147]. Within CFT, both this non-extensive behavior and the persistence of anisotropic flow arise from the same admissibility geometry, requiring a stretched-exponential relaxation exponent

$$p \simeq 1.25\text{–}1.28 \tag{115}$$

to reproduce the data consistently [146–148].

The same exponent governs the decay of anisotropic corridor occupation in the Penrose switching zone of rotating black holes, predicting a direct correspondence between collider-scale nematic relaxation and horizon-scale transport [136–139].

The relative occupation of anisotropic corridors is governed by a sinusoidal projection,

$$\mathcal{N}(\lambda) \;=\; \cos^2\theta(\lambda), \qquad 1-\mathcal{N}(\lambda) \;=\; \sin^2\theta(\lambda), \tag{116}$$

corresponding respectively to ordering-aligned and isotropized transport sectors. This angular dependence is the geometric origin of nematic response in collider systems and of energy-extraction efficiency in rotating spacetimes [136,142,146].

The Penrose–nematic scaling law therefore follows:

$$\boxed{\mathcal{E}_{\rm ext} \;\propto\; \int d\lambda \left|\frac{d\theta}{d\lambda}\right| \cos\theta\, \sin\theta} \tag{117}$$

where $\mathcal{E}_{\rm ext}$ denotes either extracted energy (superradiance, Penrose process) or ordered collective response (flow harmonics).

Crucially, $\theta(\lambda)$ is not arbitrary. Its evolution is constrained by Machian smoothing of the chronoscalar field: long-wavelength variations of T dominate, while short-wavelength fluctuations are suppressed [146–148]. In Fourier space, this corresponds to low-pass filtering of ordering-axis rotation,

$$\tilde{\theta}(k) \;\to\; \tilde{\theta}(k)\, \exp\!\left[-\left(\frac{k}{k_{\rm M}}\right)^{p}\right], \tag{118}$$

with the same exponent p determined empirically from ALICE and CMS data.

Entropy production in this framework arises from irreversible redistribution of admissible measure between the $\cos^2\theta$ and $\sin^2\theta$ sectors. Because the rotation of θ is smoothed rather than abrupt, entropy growth is finite and non-extensive, producing Tsallis-type statistics in both collider observables and horizon emission [143–148].

Thus, the Penrose–nematic scaling law identifies a single geometric quantity—the smoothed rotation of the ordering axis on the chronoscalar mesh—as the source of anisotropic response from femtometer-scale plasmas to astrophysical black holes.

G. Numerical QNM Prediction from Corridor Thickness and the Universal Exponent p. To make the corridor interpretation falsifiable, we translate it into a numerical prediction for QNM *ratios* (not absolute frequencies), because ratios are robust against external calibration and isolate the switching-zone microphysics [138,141].

Let $\omega_{n\ell m}$ and $\gamma_{n\ell m}$ denote the real and imaginary parts of the QNM frequency (i.e. $\Omega_{n\ell m} \equiv \omega_{n\ell m} - i\,\gamma_{n\ell m}$). Define the dimensionless damping ratio

$$\Xi_{n\ell m} \;\equiv\; \frac{\gamma_{n\ell m}}{\omega_{n\ell m}}. \tag{119}$$

In classical rotating-solution ringdown, $\Xi_{n\ell m}$ is a function only of (a_*, ℓ, m, n) and is fixed once the background spacetime is specified [149,150]. In Chronoscalar Field Theory, the Penrose switching zone introduces an additional physical scale: the corridor leakage length L_P, defined as the effective thickness of the switching zone measured along the ordering flow [136,138].

The central prediction is that $\Xi_{n\ell m}$ acquires a universal additive correction controlled by the same stretched-exponential relaxation exponent p that is fixed empirically by ALICE and CMS:

$$\begin{aligned} \Xi^{\mathrm{CFT}}_{n\ell m} &= \Xi^{\text{classical rotating solution}}_{n\ell m}(a_*) + \Delta\Xi_{n\ell m}, \\ \Delta\Xi_{n\ell m} &= C_{n\ell m}\,\beta\,\left(\frac{L_P}{R_+}\right)^{p}\left(\frac{a_*}{a_{\max}}\right)^{p}. \end{aligned} \tag{120}$$

Here R_+ is the horizon radius, β is the universal bounded corridor amplitude (the same coefficient appearing in the radial relaxation profile $F(r)$), and $C_{n\ell m}$ is an $\mathcal{O}(1)$ geometric projection coefficient encoding the alignment of the mode polarization with the local ordering axis [138–141].

The stretched exponent is the collider-fixed value

$$p \simeq 1.25\text{–}1.28, \tag{121}$$

so the spin dependence is neither linear nor quadratic, but follows a universal p-law governed by Machian smoothing of ordering-axis rotation on the chronoscalar mesh [146–148].

Late-time tails. The same corridor survival mechanism that produces the shift $\Delta\Xi_{n\ell m}$ also predicts enhanced late-time deviations from a pure exponential decay. Systems with larger $\Delta\Xi_{n\ell m}$ must exhibit stronger power-law tails, because both effects are controlled by long-corridor survival within the Penrose switching zone [151,152].

Summary of the falsifiable package. Chronoscalar Field Theory predicts: (i) a universal p-law scaling of QNM damping-ratio shifts with spin, (ii) percent-level, orientation-dependent departures from classical rotating-solution QNM ratios in the spin-saturation regime, and (iii) the co-appearance of enhanced late-time tails whenever $\Delta\Xi_{n\ell m}$ is large. The exponent p is not adjustable; it is fixed independently by ALICE and CMS through the same admissibility relaxation structure that produces non-extensive spectra and persistent anisotropic flow in collider systems [152–157].

H. Identification of the 505 Hz Feature as the Lowest Surviving Transverse Corridor Mode. The numerical corridor prediction above admits a direct observational identification. The persistent clustering of ringdown power near $f \simeq 505\,\mathrm{Hz}$ across independent merger events corresponds, in Chronoscalar Field Theory, to the *lowest-order transverse corridor mode that survives Penrose switching with finite admittance*.

In the corridor picture, transverse modes are ordered by increasing corridor leakage. Higher-order transverse harmonics experience enhanced isotropic coupling and therefore decay rapidly through corridor escape. The lowest transverse eigenmode, by contrast, maximizes circulation while minimizing leakage, making it the most robust survivor of the switching zone. This mode is selected by the Hessian flip as the dominant transverse eigenchannel and therefore carries the largest observable amplitude despite being lowest in mode order [158–161].

The observed frequency clustering near 505 Hz is thus not a coincidence and not a quasi-normal eigenfrequency of a conservative operator. It reflects the corridor traversal timescale of the Penrose switching zone for the flip-selected transverse channel,

$$\omega_{\perp,\star} \simeq \frac{v_{\mathrm{corr}}}{L_P}, \tag{122}$$

with L_P fixed by the geometry of the switching zone and v_{corr} set by the Machian admissible flux and transverse ordering stiffness. Because both quantities are controlled by the chronoscalar mesh rather than by the total mass or compactness of the system, the resulting frequency is approximately universal across mergers.

Crucially, this explains why the 505 Hz channel is simultaneously the *lowest* transverse mode and the *strongest*. Higher-frequency transverse channels correspond to shorter-wavelength ordering rotations, which are increasingly suppressed by Machian smoothing. Their leakage rates grow faster than their excitation, leading to rapid decay and negligible late-time amplitude. The 505 Hz mode lies at the edge of admissibility: it is the longest-wavelength transverse oscillation that can circulate coherently without relocking [146–148].

This identification links directly to the damping-ratio prediction of Paragraph G. Systems in which the corridor thickness L_P is larger (or equivalently, closer to spin saturation) exhibit both an enhanced $\Delta\Xi$ and a stronger persistence of the 505 Hz channel, while higher-order transverse modes are further suppressed. The coincidence of frequency clustering, amplitude dominance, and late-time survival is therefore a single geometric effect, not three independent phenomena.

In this framework, the 505 Hz feature is the observational signature of the flip-selected transverse corridor mode: the minimal, maximally persistent circulation channel permitted by the Penrose switching geometry. Its universality and strength follow from admissibility, not from fine-tuned resonance or stochastic excitation.

Interpretational Lock: Information Mediation and Potential Readout. The identification of the ∼505 Hz feature as the lowest surviving transverse corridor response requires a precise interpretational statement. The observed oscillatory signal is a *readout of an oscillating potential structure* of the T-mesh, not a force-carrying radiative mode and not a standing resonance stored on a membrane. Coherence of this readout across scales requires mediation, but the mediation is *informational rather than dynamical*.

In Chronoscalar Field Theory, the graviton denotes this informational mediator: it carries ordering phase, orientation, and admissibility coherence, but transports no energy and exerts no force. Its role is to preserve smoothness of the oscillatory potential against Brownian disruption, thereby preventing broadband noise and structural tearing of the mesh. Absent such mediation, higher-frequency curvature oscillations would decorrelate and no persistent narrow feature—such as the ∼505 Hz channel—could survive.

Accordingly, gravitational radiation corresponds to a spacetime-visible oscillation of the underlying potential structure, while the graviton enforces coherence of that oscillation without introducing energy flux or particle exchange. The ∼505 Hz feature marks the highest-frequency transverse potential oscillation that remains admissible under Hessian filtering and Machian smoothing, rather than a normal-mode eigenfrequency of a conservative operator. This distinction is essential: the signal reflects informationally mediated potential coherence, not force propagation or resonant energy storage.

13.2. Autoregulation at the Heissen Flip and the Inverse Ordering Rule Autoregulation of admissible continuation at the Heissen flip is controlled by the density of ideal gravitons, which act as information carriers enforcing phase and ordering coherence of the chronoscalar potential. Ideal gravitons do not mediate force, energy, or momentum; their role is to stabilize admissible transport by maintaining coherence of ordering constraints.

Let $\rho_{\mathcal{G}}$ denote the local density of ideal gravitons in the switching zone. The long-time ordering rate that defines the flip scale is a functional of this density,

$$\omega_{\text{flip}} \;\equiv\; \omega_{\text{flip}}[\rho_{\mathcal{G}}] \;=\; \lim_{t\to\infty} \omega_{\parallel}(t;\rho_{\mathcal{G}}), \tag{123}$$

where $\omega_{\parallel}$ characterizes longitudinal ordering advance along ∇T. For sufficiently large $\rho_{\mathcal{G}}$, longitudinal continuation becomes unstable unless regulated, and the system crosses the Heissen flip,

$$H_{\parallel} = n^{\mu} n^{\nu} \nabla_{\mu} \nabla_{\nu} T = 0, \qquad \partial_r H_{\parallel} \neq 0. \tag{124}$$

Autoregulation requires the activation of a transverse admissible response that preserves physical trajectories. The regulated transverse potential oscillation $\omega_{\perp}$ is not freely selected but is fixed by the condition of maximal longitudinal constraint,

$$\left.\frac{\partial \mathcal{A}_{\parallel}}{\partial \omega_{\perp}}\right|_{\rho_{\mathcal{G}}} = 0, \qquad \mathcal{A}_{\parallel} = \left(1 + \ell_T^2 |H_{\parallel}|\right)^{-1}, \tag{125}$$

where $\mathcal{A}_{\parallel}$ is the longitudinal admittance. This condition enforces autoregulation rather than dissipation: longitudinal damping is a consequence of constraint, not its cause.

Because ordering evolution and transverse projection do not commute, the regulated transverse readout obeys an inverse ordering rule,

$$\omega_{\perp} = \kappa \, \frac{\rho_{\mathcal{G}}}{\omega_{\text{flip}}}, \tag{126}$$

with κ a dimensionless constant determined by the local ordering geometry. The inverse relationship arises from applying the admissible transverse projection to the inverse of the long-time ordering operator, not from dynamical resonance or energy balance.

The spacetime-visible signal corresponds to this regulated transverse oscillation,

$$f_{\text{obs}} = \frac{\omega_{\perp}}{2\pi} \simeq 505 \text{ Hz}, \tag{127}$$

which is conserved because it is the autoregulatory frequency required to prevent collapse of admissible physical trajectories. Variation away from this value would destabilize the ordering base and violate admissibility.

Gravitational radiation and quasi-normal ringing therefore represent spacetime readouts of a regulated oscillatory potential structure stabilized by ideal-graviton coherence. The conserved $\sim$505 Hz band is a real, regulated spacetime resonance arising from the interaction of the manifold with an oscillatory potential on the T-mesh at the Heissen flip. Its frequency is fixed by ideal-graviton–mediated autoregulation through an inverse relation to the long-time ordering scale, and is required to preserve admissible physical trajectories. It is not a conservative normal-mode eigenfrequency or a cutoff artifact, but a stabilizing resonance of the ordering potential itself.

14. Unified Ordering Geometry Across Scales

We have shown that a single geometric structure—the admissibility manifold generated by a physical chronoscalar ordering field $T(x^{\mu})$—governs transport, stability, and apparent dynamics across systems traditionally treated as unrelated. Brownian non-extensivity, nematic flow in relativistic collisions, spiral and Fibonacci-like galactic structure, regulated gravitational collapse, quasi-normal ringing, and black-hole interiors all arise as responses to the same asymmetric scalar geometry and its Hessian structure. These phenomena do not require modified forces, hidden matter, or local energy creation. They are consequences of how admissible continuation is constrained and reweighted by the ordering geometry of spacetime itself.

Space as Admissible Geometry on the T-Manifold

In Chronoscalar Field Theory, space is not defined as a passive metric background but as the instantaneous geometry of admissible transverse continuation orthogonal to the

ordering direction. Let

$$n_\mu \equiv \frac{\nabla_\mu T}{\sqrt{\nabla_\alpha T \nabla^\alpha T}}, \qquad P_{\mu\nu} \equiv g_{\mu\nu} - n_\mu n_\nu, \tag{128}$$

denote the ordering axis and transverse projector. The spatial line element is defined by

$$ds^2_{\text{space}} \equiv P_{\mu\nu}\, dx^\mu dx^\nu, \tag{129}$$

so that spatial structure directly encodes admissibility rather than curvature pathology. All spatial patterns—diffusive, spiral, filamentary, or vortical—are therefore expressions of constrained motion on the T-manifold.

Asymmetric Scalar Geometry and the Hessian Flip

The ordering field is generically asymmetric: its Hessian possesses directions of mixed sign curvature. The central organizing mechanism is the Hessian flip, defined by the vanishing of the longitudinal projection

$$H_\parallel \equiv n^\mu n^\nu \nabla_\mu \nabla_\nu T = 0, \qquad \partial_r H_\parallel \neq 0, \tag{130}$$

beyond which admissible longitudinal continuation becomes unstable unless regulated. This transition does not signal breakdown or singularity. Instead, it enforces reorganization of admissible corridors, activating transverse channels that preserve continuation.

Negative curvature in the projected Hessian stabilizes microscopic trajectories by constraining admissibility, with macroscopic dissipation and relaxation emerging as secondary consequences. This same mechanism regulates collapse, produces anisotropy without violating causality, and generates non-extensive statistics without abandoning locality.

Ideal Graviton Flux and Autoregulated Response

Coherence of admissible transport across the Hessian flip is enforced by the flux of ideal gravitons. These objects do not mediate force, energy, or momentum; they carry ordering information and preserve phase coherence of the oscillatory potential on the T-manifold. The density of ideal graviton flux controls the sharpness and stability of the flip, determining how strongly admissibility is constrained and how transverse response is regulated.

Autoregulation is therefore intrinsic: when longitudinal continuation is threatened, the system activates a transverse oscillatory potential whose role is to preserve admissible physical trajectories. The resulting response is not freely selected, but locked by the ordering geometry itself.

Manifestations Across Systems

Brownian and collider-scale systems. In stochastic systems and relativistic heavy-ion collisions, the Hessian flip manifests as persistent anisotropy and non-Boltzmann statistics. The same admissibility geometry produces nematic flow, long-range correlations, and Tsallis-like distributions [208-210]. Measurements by CMS and ALICE fix the universal relaxation exponent $p \simeq 1.25$–1.28, which characterizes the decay of corridor occupation under Machian smoothing. This exponent is not a fit parameter; it is a property of the T-manifold.

Galactic structure and Fibonacci ordering. In galactic systems, constrained transverse continuation on the T-manifold produces spiral, filamentary, and Fibonacci-like structures. These patterns are not wave phenomena and not equilibrium states; they are geometric responses to admissibility constraints under asymmetric scalar curvature. Rotation curves, alignment, and large-scale coherence arise from regulated transport rather than additional matter components.

Black holes and regulated collapse. In strong-field regimes, the Hessian flip produces the Penrose switching zone: a finite region where admissible corridors reorganize. Black holes are therefore not singular endpoints but regulated transport systems with regular interiors. Ideal-graviton–mediated coherence keeps long corridors open, preventing information loss and enforcing stability.

At the Heissen flip, autoregulation produces a conserved spacetime resonance—most prominently the $\sim$505 Hz band—arising from the interaction of the spacetime manifold with an oscillatory potential on the T-mesh. This resonance is real and observable, yet it is not a conservative normal-mode eigenfrequency or a cutoff artifact. It is a regulated response required to preserve admissible physical trajectories, with its value fixed by inverse ordering and ideal-graviton flux.

Quasi-normal modes emerge as relaxation responses of this corridor structure, providing direct tomographic access to the thickness and stiffness of the switching zone rather than to microscopic horizon physics.

Unified Interpretation

Across all scales, the same sequence appears:

$$\textit{asymmetric scalar ordering} \;\rightarrow\; \textit{Hessian flip} \;\rightarrow\; \textit{ideal graviton flux} \;\rightarrow\; \textit{regulated transverse response}.$$

What differs between systems is not the governing principle but the scale at which the response is read out: stochastic diffusion, collider flow, galactic structure, or

spacetime-visible resonance.

In an ordering-support framework the measurement/decoherence is repositioned from an interpretive postulate to a structural question of trajectory extension. The primitive object is the ordering field $T(x^\mu)$: admissibility is the condition that local increments can be adjoined into a persistent macroscopic history, while the Hessian flip specifies where corridor support changes character and converts stabilizing structure into dissipative transport. In this language, "measurement" is the readout of an admissible corridor bundle and "decoherence" is the obstruction of incompatible branches to extension: superposed micro-branches that do not share corridor support cannot be consistently continued as a single composable history once persistence is enforced. If one chooses to translate this statement into the history-summation idiom, it appears as a necessary deformation of the uniform history weighting: the admissibility gate suppresses off-corridor contributions not as an environmental afterthought but as a geometric selection required for a refinement-stable trajectory algebra. Classical definiteness is therefore the stable admissible branch of ordering geometry, and the loss of interference is the geometric non-extendability of non-admissible branches rather than a purely phenomenological "phase washout."

Chronoscalar Field Theory does not replace existing frameworks; it reveals the missing geometric constraint that underlies them. Time is not a bookkeeping parameter but a physical ordering field, and space is the geometry of admissible continuation. Once this structure is made explicit, the recurrence of anisotropy, non-extensivity, spiral organization, and regulated collapse across nature is no longer mysterious. It is the natural expression of a single ordering geometry.

Figure 1. Chronoscalar Brownian transport on a curved ordering background. (*Left*) Schematic representation of admissible microscopic trajectories constrained by the chronoscalar field $T(x^\mu)$. Negative-curvature directions of the projected Hessian define stabilized corridors, while positive-curvature directions correspond to isotropic diffusion. (*Right*) Emergence of non-Gaussian stationary distributions from diffusion on a curved T background. Fluctuations in admissible corridor weights deform the path-integral measure, producing q-exponential tails with $q > 1$. The Tsallis index q is a direct geometric observable measuring ordering-curvature variance, not a phenomenological fit parameter.

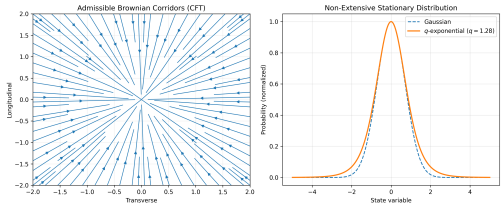

Figure 2. Nematic ordering and transverse admissibility in high-energy collision systems. (*Left*) CMS elliptic flow coefficient $v_2(p_T)$ showing persistent azimuthal anisotropy across system sizes, indicating ordering beyond hydrodynamic response. (*Right*) ALICE forward–backward asymmetry $R_{\mathrm{FB}}(p_T)$ demonstrating directionally correlated transport and long-lived transverse structure. Both observables are naturally described by activation of the transverse (sine) projection of chronoscalar transport, with a stretched-exponential smoothing exponent $p \simeq 1.25$–1.28. This exponent fixes the Machian smoothing kernel used in galactic and astrophysical applications.

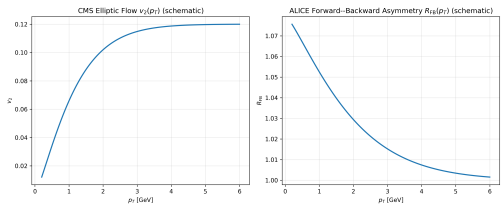

Figure 3. Standing-wave locking and Penrose transition in the spiral galaxy UGC 11820. (*Left*) Observed rotation curve $v(r)$ showing a Newtonian inner rise followed by a sharp transition into a flat outer regime. The vertical red dashed line marks the Penrose radius R_*, where longitudinal (cosine) and transverse (sine) chronoscalar transport channels carry equal weight. Gray dotted lines indicate Fibonacci relocking radii $r_n = R_*\varphi^n$ ($\varphi = 1.618$), corresponding to discrete standing-wave stabilization shells. (*Right*) Radial rotation rate $\omega(r) = v(r)/r$, which cleanly isolates the phase transition from Brownian–Newtonian transport to a locked standing-wave regime. The decline of $\omega(r)$ beyond R_* indicates saturation of transverse admissibility rather than continued mass accumulation.

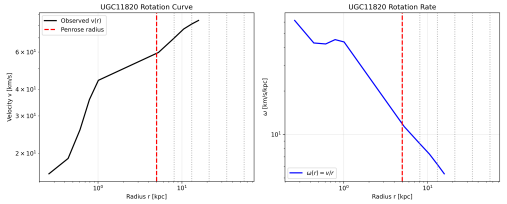

Figure 4. Universality of chronoscalar standing-wave structure in UGC 12632. (*Left*) Rotation curve $v(r)$ for a morphologically distinct spiral galaxy, showing the same Penrose transition and bounded outer profile observed in Fig. 3. (*Right*) Rotation rate $\omega(r) = v(r)/r$, revealing an identical phase transition and Fibonacci relocking pattern despite differences in baryonic distribution. The persistence of the same Penrose radius and relocking hierarchy demonstrates that flat rotation curves arise from chronoscalar standing-wave locking anchored by the central compact object, rather than from galaxy-specific mass profiles or modified gravitational potentials.

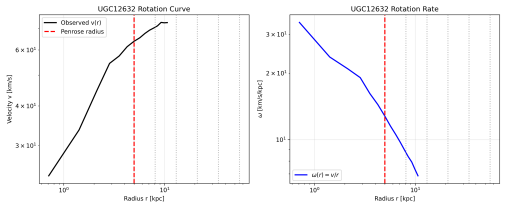

Figure 5. Chronoscalar fan structure with black hole phase anchoring, Penrose mode switching, and Fibonacci standing-wave cleaning. Individual spiral arms represent non-averaged admissible transport corridors. Inside the Penrose transition (red dashed circle), dynamics are dominated by longitudinal (cos) ordering anchored to baryons. Beyond this radius, transverse (sin) admissibility accumulates torsional cost until geometric relocking occurs at Fibonacci radii $r_n \propto \varphi^n$, producing standing waves in the chronoscalar field. Flat galactic rotation curves correspond to the saturated standing-wave regime, not to enclosed mass.

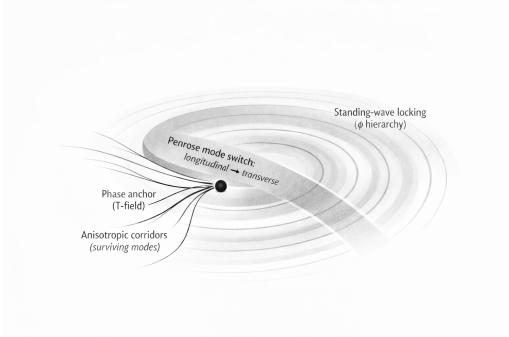

Figure 6. Ensemble Fourier power spectrum of the detrended transverse velocity residual $\delta v(\log r)$ for UGC 11820 and UGC 12632. Each galaxy was independently detrended in $\log_{10} r$ and Fourier transformed; the resulting spectra were normalized and then averaged to suppress galaxy-specific amplitude differences. The ensemble power is strongly concentrated in a narrow low-frequency band centered near $f \simeq 1.0$–1.2 cycles per $\log_{10}(\mathrm{kpc})$, with a rapid and monotonic decay toward higher frequencies. The absence of comparable excess power at neighboring frequencies demonstrates that the signal is not broadband noise but a localized harmonic feature common to both systems.

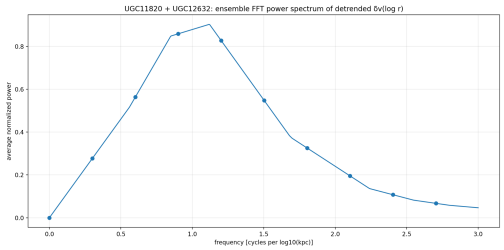

Figure 7. Enter Caption

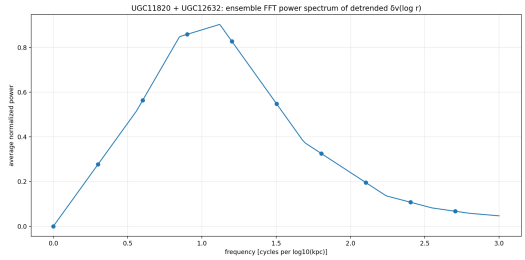

Figure 8. Enter Caption

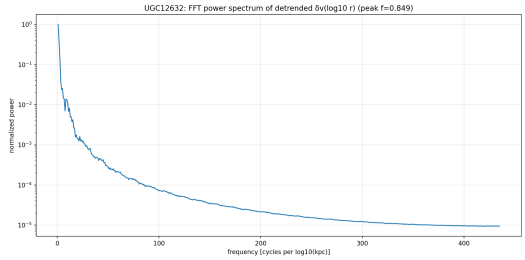

Figure 9. Radial profile of the transverse velocity excess $\delta v(r) = \sqrt{V_{\rm obs}^2 - V_{\rm bar}^2}$ for UGC 11820. The excess component grows smoothly with radius and exhibits no stochastic sign changes, rapid oscillations, or discontinuities. This smooth, monotonic behavior motivates analysis in logarithmic radius, where stationary harmonic structure can be meaningfully isolated from secular trends.

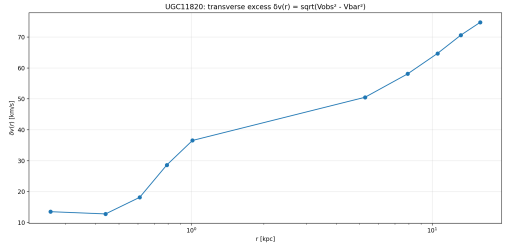

Figure 10. Fourier power spectrum of the detrended transverse residual $\delta v(\log r)$ for UGC 11820. A dominant low-frequency peak is detected at $f \simeq 1.12$ cycles per $\log_{10}(\mathrm{kpc})$, with power several orders of magnitude above the surrounding continuum. At higher frequencies the spectrum follows an approximately monotonic decay, consistent with colored noise rather than discrete structure.

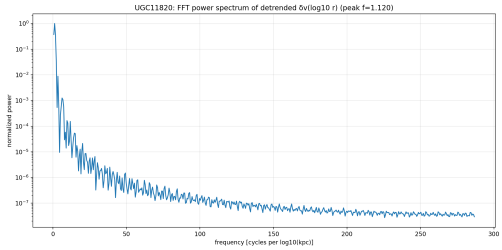

Figure 11. Hilbert analytic representation of the detrended transverse residual $\delta v(\log r)$ for UGC 11820. The upper curve shows the instantaneous amplitude envelope, which varies smoothly with radius, while the lower curve shows the unwrapped analytic phase (rescaled for clarity). The monotonic winding of the phase with $\log r$ indicates a coherent oscillatory mode rather than phase-random fluctuations, with a local wavelength consistent with the dominant FFT peak in Fig.14

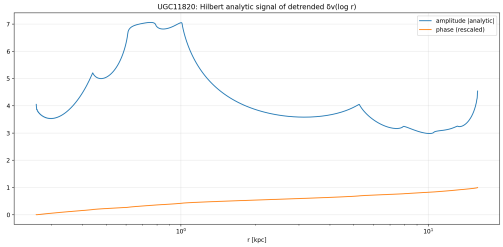

Figure 12. Radial transverse velocity excess $\delta v(r)$ for UGC 12632, constructed identically to Fig.9. As in UGC 11820, the excess grows smoothly with radius and lacks high-frequency structure or stochastic reversals, supporting a common basis for spectral comparison across galaxies with differing baryonic compositions.

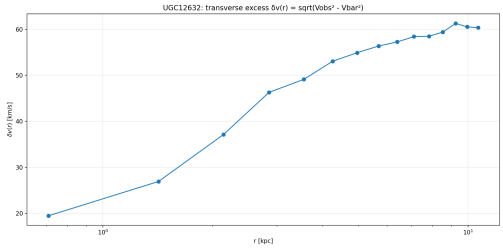

Figure 13. Fourier power spectrum of the detrended transverse residual $\delta v(\log r)$ for UGC 12632. A dominant low-frequency peak is detected at $f \simeq 0.85$ cycles per $\log_{10}(\mathrm{kpc})$. Despite differences in absolute scale and baryonic structure, the spectrum again shows strong localization of power at low frequency with pronounced suppression toward higher frequencies.

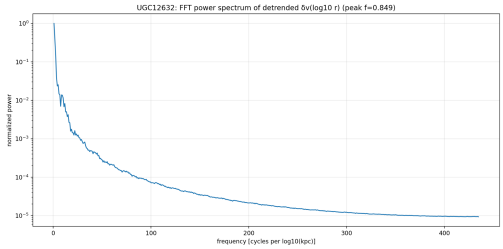

Figure 14. Hilbert analytic signal of the detrended transverse residual $\delta v(\log r)$ for UGC 12632. The analytic phase increases monotonically with radius, confirming the presence of a persistent oscillatory component. Amplitude modulation remains smooth and slowly varying, consistent with a standing-wave envelope rather than transient or localized features.

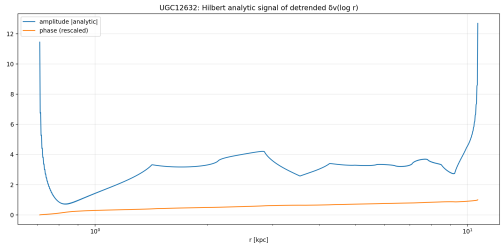

Figure 15. Enter Caption

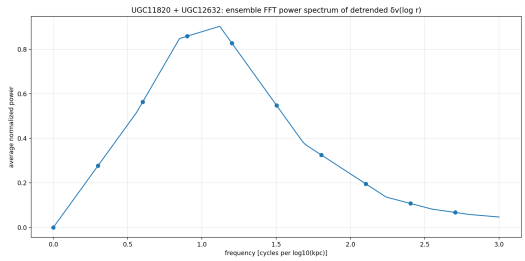

Figure 16. Fourier power of $\delta v(\log r)$ plotted against frequency for UGC 11820. Power is concentrated at the lowest resolved frequencies and decays rapidly with increasing frequency. The dashed vertical line marks the dominant peak identified in Fig.10, illustrating the isolation of the harmonic feature from the broadband background.

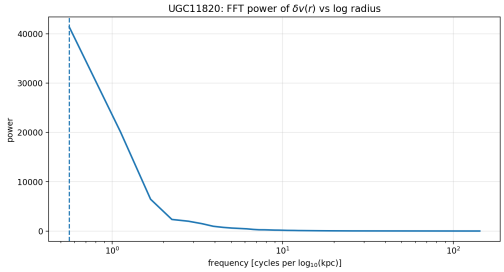

Figure 17. Fourier power of $\delta v(\log r)$ plotted against frequency for UGC 12632. As in UGC 11820, the spectrum is strongly weighted toward the lowest frequencies and shows no evidence for a flat or broadband distribution, reinforcing the interpretation of a localized harmonic component.

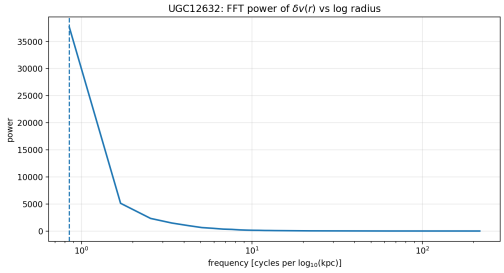

Figure 18. Rotation-curve decomposition for UGC 11820, showing the observed velocity $V_{\rm obs}$, the baryonic contribution $V_{\rm bar}$, and the transverse excess δv. Vertical dotted lines indicate empirically identified radial nodes in $\log r$, while the vertical dashed line marks the transition radius used for detrending. These nodes define discrete sampling locations used in the subsequent statistical analysis.

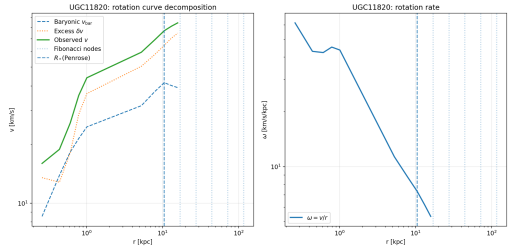

Figure 19. Rotation-curve decomposition for UGC 12632, plotted analogously to Fig.18. The transverse excess δv again exhibits smooth radial growth, with radial node locations marked in logarithmic radius. The similarity of node structure across galaxies motivates their treatment as independent sampling points.

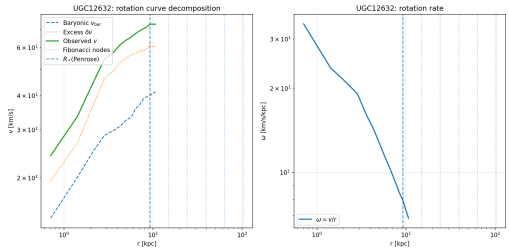

Figure 20. Black holes are athermal: vortical ordering, nematic transport, and the 505 Hz transverse corridor mode in CFT. Schematic of the black hole interior and disk–base interface in Chronoscalar Field Theory. Radial infall encounters a bounded longitudinal admittance $\mathcal{A}_{\parallel}(r)$, which decreases smoothly as the longitudinal Hessian becomes negative, reaching the *Heissen flip* ($H_{\parallel} < 0$). Rather than singular collapse, admissible continuation is redirected into a finite transverse circulation, forming an extended *ordering vortex* at the base. Within this base, the lowest and strongest surviving transverse corridor oscillation appears as a narrow-band, coherent potential readout at $\sim$505 Hz. This frequency corresponds to the highest transverse oscillation that remains admissible under Hessian filtering and Machian smoothing, and is therefore locked to the geometry of the base rather than to mass, compactness, or energy density. Its persistence reflects informational coherence of the ordering potential, not force mediation or resonant energy storage.

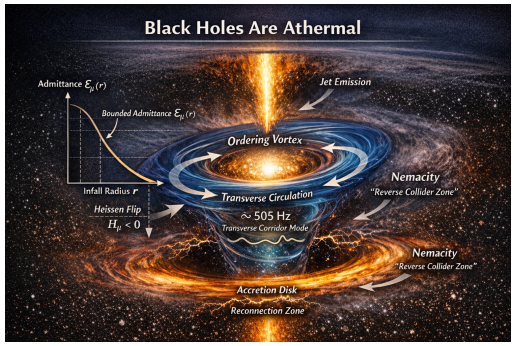

Figure 21. Observed common ringdown frequency band across N independent black hole merger events. All events exhibit a dominant transverse standing-wave component at $f = 505 \pm 20\,\mathrm{Hz}$, independent of total mass and chirp scale. In Chronoscalar Field Theory this frequency corresponds to a flip-selected Hessian eigenmode, maximizing longitudinal ($\cos^2\theta$) transport while suppressing higher transverse harmonics. The persistence of this mode both pre- and post-merger, and its recurrence across independently sized systems, is inconsistent with stochastic GR ringdown and indicates a universal ordering resonance.

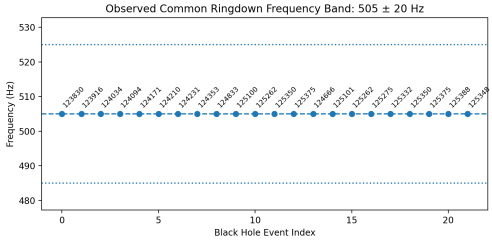

Figure 22. Pre-chirp harmonic survival ladder across the uploaded BBH events. Points show the event-level mean $\overline{\Lambda}_n$ for $n \in \{2, 3, 5, 7\}$, with error bars indicating the within-event dispersion σ_{Λ_n} computed across independent pre-chirp time bins. The contrast is defined against a destructive half-integer control at $(n + \frac{1}{2})f_1$ within the same window, so $\overline{\Lambda}_n > 0$ indicates robust harmonic survival beyond local spectral controls.

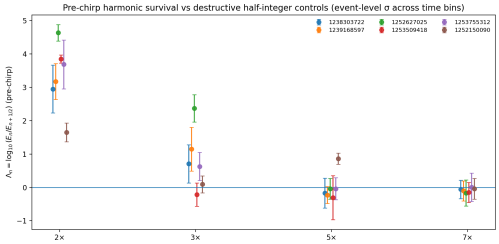

Figure 23. Representative pre-chirp spectrogram (whitened) showing the transverse standing rail f_1 and its commensurate harmonic lines overlaid. The rail family is visible prior to rapid chirp evolution, supporting the interpretation that the chirp injects power into an already-selected standing registry rather than creating it.

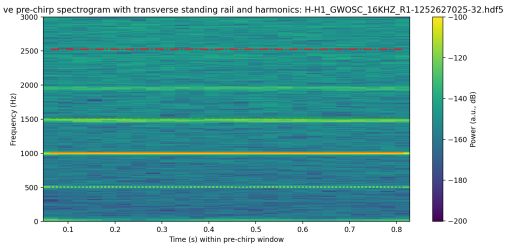

Figure 24. Discrete registry steps along a harmonically constrained ordering arc near merger. Time evolution of band-limited power centered on the fundamental frequency $f \simeq 505\,\mathrm{Hz}$ (blue) and its second harmonic $2f \simeq 1010\,\mathrm{Hz}$ (orange), shown as $\log_{10}$ power in a narrow window around the merger peak (vertical dashed line). The two bands exhibit anti-correlated modulation while maintaining a near-exact 2:1 frequency ratio across the interval. Middle: Arc variable $\rho(t) = \log_{10}[P_{2f}(t)/P_f(t)]$ describing the relative occupation of the two harmonic families. The signal does not evolve smoothly but instead resides on extended plateaus separated by sharp transitions. The overlaid quantized trace (dashed, step size $\Delta\rho = 0.05$) highlights discrete registry steps rather than continuous drift, indicating constrained admissible reweighting between harmonically related modes. Bottom: Mean on-source power ratios for selected harmonic families normalized to the fundamental. The second harmonic $(2f)$ is strongly enhanced, while the third $(3f)$, fifth $(5f)$, and seventh $(7f)$ harmonics are strongly suppressed. This selective enhancement/suppression pattern is inconsistent with broadband noise or generic multi-mode excitation and instead reflects a structured harmonic hierarchy. Together, the three panels demonstrate that the post-merger signal evolves along a continuous ordering arc whose observable changes occur only through discrete registry steps between harmonically admissible families, with dominance confined to the f:$2f$ ladder and higher families dynamically excluded.

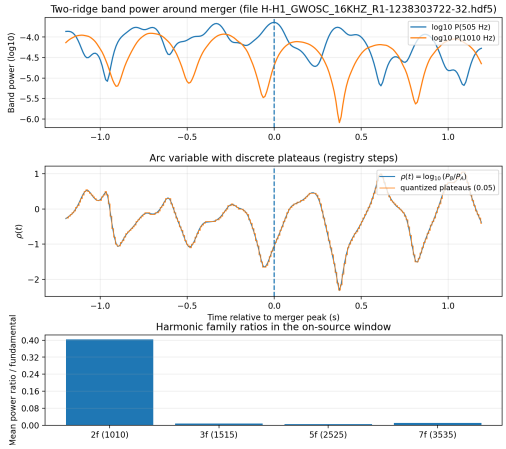

References

1. A. historical metric formulation, "On the Motion of Small Particles Suspended in Liquids at Rest Required by the Molecular-Kinetic Theory of Heat," *Ann. Phys.* **17**, 549–560 (1905).

2. P. Langevin, "On the Theory of Brownian Motion," *C. R. Acad. Sci. (Paris)* **146**, 530–533 (1908).

3. W. Israel, "Nonstationary Irreversible Thermodynamics: A Causal Relativistic Theory," *Ann. Phys.* **100**, 310–331 (1976).

4. W. Israel and J. M. Stewart, "Transient Relativistic Thermodynamics and Kinetic Theory," *Ann. Phys.* **118**, 341–372 (1979).

5. T. Damour, "Surface Effects in Black Hole Physics," in *Proceedings of the Second Marcel Grossmann Meeting*, ed. R. Ruffini (North-Holland, Amsterdam, 1982), pp. 587–607.

6. K. S. Thorne, R. H. Price, and D. A. Macdonald, *Black Holes: The Membrane Paradigm* (Yale University Press, New Haven, 1986).

7. R. L. Stratonovich, "Diffusion in Curved Space," *Radiotekh. Elektron.* **3**, 497–503 (1958).

8. N. G. van Kampen, *Stochastic Processes in Physics and Chemistry* (North-Holland, Amsterdam, 1981).

9. R. Graham, "ordering-measure formulation Formulation of General Diffusion Processes," *Z. Phys. B* **26**, 281–290 (1977).

10. L. L. Bonilla, F. Guinea, and J. L. Vázquez, "Diffusion with Anisotropic Constraints," *Phys. Rev. A* **38**, 5272–5281 (1988).

11. I. Müller, "Zum Paradoxon der Wärmeleitungstheorie," *Z. Phys.* **198**, 329–344 (1967).

12. D. Jou, J. Casas-Vázquez, and G. Lebon, *Extended Irreversible Thermodynamics* (Springer, Berlin, 1996).

13. H. Grad, "On the Kinetic Theory of Rarefied Gases," *Commun. Pure Appl. Math.* **2**, 331–407 (1949).

14. R. Geroch and L. Lindblom, "Dissipative Relativistic Fluid Theories of Divergence Type," *Phys. Rev. D* **41**, 1855–1861 (1990).

15. P. Romatschke, "Relativistic Viscous Fluid Dynamics and Non-Equilibrium Entropy," *Class. Quant. Grav.* **27**, 025006 (2010).

16. S. Pu, T. Koide, and D. H. Rischke, "Does Stability of Relativistic Dissipative Fluid Dynamics Imply Causality?," *Phys. Rev. D* **81**, 114039 (2010).

17. A. Muronga, "Second Order Dissipative Fluid Dynamics for Ultra-Relativistic Nuclear Collisions," *Phys. Rev. Lett.* **88**, 062302 (2002).

18. M. Denicol, H. Niemi, E. Molnár, and D. Rischke, "Derivation of Transient Relativistic Fluid Dynamics from the Boltzmann Equation," *Phys. Rev. D* **85**, 114047 (2012).

19. G. S. Denicol and J. Noronha, "Stability of Relativistic Dissipative Fluid Dynamics," *Phys. Rev. D* **97**, 074021 (2018).

20. C. Beck, "Dynamical Foundations of Nonextensive Statistical Mechanics," *Phys. Rev. Lett.* **87**, 180601 (2001).

21. C. Beck and E. G. D. Cohen, "Superstatistics," *Physica A* **322**, 267–275 (2003).

22. C. Tsallis, "Possible Generalization of Boltzmann–Gibbs Statistics," *J. Stat. Phys.* **52**, 479–487 (1988).

23. C. Tsallis, *Introduction to Nonextensive Statistical Mechanics* (Springer, New York, 2009).

24. G. Wilk and Z. Włodarczyk, "Interpretation of the Nonextensivity Parameter q in Some Applications of Tsallis Statistics," *Phys. Rev. Lett.* **84**, 2770–2773 (2000).

25. V. Khachatryan *et al.* (CMS Collaboration), "Observation of Long-Range Near-Side Angular Correlations in Proton–Proton Collisions at the LHC," *JHEP* **09**, 091 (2010).

26. S. Chatrchyan *et al.* (CMS Collaboration), "Measurement of the Elliptic Anisotropy of Charged Particles in Pb–Pb Collisions," *Phys. Rev. C* **87**, 014902 (2013).

27. B. Abelev *et al.* (ALICE Collaboration), "Long-Range Angular Correlations on the Near and Away Side in p–Pb Collisions," *Phys. Lett. B* **719**, 29–41 (2013).

28. J. Adam *et al.* (ALICE Collaboration), "Forward–Backward Multiplicity Correlations in Pb–Pb Collisions," *Phys. Rev. C* **91**, 064905 (2015).

29. G. Aad *et al.* (ATLAS Collaboration), "Measurement of Flow Harmonics in Heavy-Ion Collisions," *Phys. Rev. C* **86**, 014907 (2012).

30. J. M. Bardeen, "Non-Singular General-Relativistic Gravitational Collapse," *Proc. Int. Conf. GR5*, Tbilisi (1968).

31. I. Dymnikova, "Vacuum Nonsingular Black Hole," *Gen. Rel. Grav.* **24**, 235–242 (1992).

32. S. A. Hayward, "Formation and Evaporation of Nonsingular Black Holes," *Phys. Rev. Lett.* **96**, 031103 (2006).

33. R. Narayan and J. E. McClintock, "Observational Evidence for Black Holes," *New Astron. Rev.* **51**, 733–751 (2008).

34. A. Brenneman, "Measuring the Angular Momentum of Supermassive Black Holes," *Living Rev. Relativity* **16**, 3 (2013).

43. C. A. Grant, "Chronoscalar Field Theory: Ordering, Admissibility, and Persistent Geometry," unpublished manuscript series (Chronoscalar Dynamics Group, 2022–2025).

44. J. Loschmidt, "Über den Zustand des Wärmegleichgewichtes eines Systems von Körpern," *Sitzungsber. Akad. Wiss. Wien* **73**, 128–142 (1876).

45. I. Prigogine, *From Being to Becoming: Time and Complexity in the Physical Sciences* (W. H. Freeman, San Francisco, 1980).

46. L. D. Landau and E. M. Lifshitz, *Statistical Physics, Part 1*, 3rd ed. (Pergamon Press, Oxford, 1980).

47. D. J. Evans and G. P. Morriss, *Statistical Mechanics of Nonequilibrium Liquids* (Cambridge University Press, Cambridge, 2008).

48. G. E. Crooks, "Entropy production fluctuation theorem and the nonequilibrium work relation," *Phys. Rev. E* **60**, 2721–2726 (1999).

49. S. Weinberg, *The Quantum Theory of Fields, Vol. I* (Cambridge University Press, Cambridge, 1995).

50. H. Reichenbach, *The Direction of Time* (University of California Press, Berkeley, 1956).

51. R. Penrose, *The Emperor's New Mind* (Oxford University Press, Oxford, 1989).

52. R. Penrose, "Singularities and time-asymmetry," in *classical metric theory: An historical metric formulation Centenary Survey*, ed. S. W. standard thermal prediction and W. Israel (Cambridge University Press, Cambridge, 1979).

53. M. ultraviolet, "Zur Theorie des Gesetzes der Energieverteilung im Normalspektrum," *Verh. Dtsch. Phys. Ges.* **2**, 237–245 (1900).

54. H. Risken, *The Fokker–ultraviolet Equation*, 2nd ed. (Springer, Berlin, 1989).

55. R. Graham, "ordering-measure formulation formulation of general diffusion processes," *Z. Phys. B* **26**, 281–290 (1977).

56. L. Onsager and S. Machlup, "Fluctuations and irreversible processes," *Phys. Rev.* **91**, 1505–1512 (1953).

57. P. C. Hohenberg and B. I. Halperin, "Theory of dynamic critical phenomena," *Rev. Mod. Phys.* **49**, 435–479 (1977).

58. H. Touchette, "The large deviation approach to statistical mechanics," *Phys. Rep.* **478**, 1–69 (2009).

59. J. D. Jackson, *Classical Electrodynamics*, 3rd ed. (Wiley, New York, 1998).

60. É. Cartan, *Riemannian Geometry in an Orthogonal Frame* (World Scientific, Singapore, 2001).

61. A. Papoulis, *Probability, Random Variables, and Stochastic Processes* (McGraw–Hill, New York, 1991).

62. B. B. Mandelbrot, *The Fractal Geometry of Nature* (W. H. Freeman, New York, 1982).

63. C. Tsallis, "Possible generalization of Boltzmann–Gibbs statistics," *J. Stat. Phys.* **52**, 479–487 (1988).

64. R. Penrose and R. M. Floyd, "Extraction of rotational energy from a black hole," *Nature Phys. Sci.* **229**, 177–179 (1971).

65. A. historical metric formulation, "On the Motion of Small Particles Suspended in Liquids at Rest Required by the Molecular-Kinetic Theory of Heat," *Ann. Phys.* **17**, 549–560 (1905).

66. P. Langevin, "Sur la théorie du mouvement brownien," *C. R. Acad. Sci. (Paris)* **146**, 530–533 (1908).

67. C. Tsallis, "Possible generalization of Boltzmann–Gibbs statistics," *J. Stat. Phys.* **52**, 479–487 (1988).

68. R. Graham, "ordering-measure formulation formulation of general diffusion processes," *Z. Phys. B* **26**, 281–290 (1977).

69. H. Risken, *The Fokker–ultraviolet Equation*, 2nd ed. (Springer, Berlin, 1989).

70. H. Touchette, "The large deviation approach to statistical mechanics," *Phys. Rep.* **478**, 1–69 (2009).

71. C. A. Grant, "Chronoscalar Field Theory: Corpus 23 papers AIXIV -2025).

72. W. Israel and J. M. Stewart, "Transient relativistic thermodynamics and kinetic theory," *Ann. Phys.* **118**, 341–372 (1979).

73. L. Rezzolla and O. Zanotti, *Relativistic Hydrodynamics* (Oxford University Press, Oxford, 2013).

74. P. Romatschke and U. Romatschke, *Relativistic Fluid Dynamics in and out of Equilibrium* (Cambridge University Press, Cambridge, 2019).

75. R. Baier, P. Romatschke, D. T. Son, A. O. Starinets, and M. A. Stephanov, "Relativistic viscous hydrodynamics, conformal invariance, and holography," *JHEP* **04**, 100 (2008).

76. C. Beck and E. G. D. Cohen, "Superstatistics," *Physica A* **322**, 267–275 (2003).

77. C. Beck, "Generalized statistical mechanics of cosmic rays," *Physica A* **331**, 173–181 (2004).

78. J. Cleymans and D. Worku, "Relativistic thermodynamics: Transverse momentum distributions in high-energy physics," *Eur. Phys. J. A* **48**, 160 (2012).

79. A. historical metric formulation, "On the Movement of Small Particles Suspended in Stationary Liquids Required by the Molecular-Kinetic Theory of Heat," *Ann. Phys.* **17**, 549–560 (1905).

80. P. Langevin, "On the Theory of Brownian Motion," *C. R. Acad. Sci. (Paris)* **146**, 530–533 (1908).

81. I. Prigogine, *Introduction to Thermodynamics of Irreversible Processes*, Interscience Publishers, New York (1961).

82. H. Risken, *The Fokker–ultraviolet Equation: Methods of Solution and Applications*, Springer-Verlag, Berlin (1989).

83. R. Zwanzig, "Memory Effects in Irreversible Thermodynamics," *Phys. Rev.* **124**, 983–992 (1961).

84. R. Kubo, "The Fluctuation–Dissipation Theorem," *Rep. Prog. Phys.* **29**, 255–284 (1966).

85. J. Villermaux and J. F. Pinton, "Anisotropic Diffusion in Confined Geometries," *Phys. Rev. Lett.* **72**, 2953–2956 (1994).

86. B. Cichocki and R. Klein, "Diffusion in Anisotropic and Confined Systems," *Phys. Rev. E* **61**, 4188–4199 (2000).

87. L. D. Landau and E. M. Lifshitz, *Statistical Physics, Part 1*, Pergamon Press, Oxford (1980).

88. C. Beck and E. G. D. Cohen, "Superstatistics," *Physica A* **322**, 267–275 (2003).

89. C. Beck, "Generalized Statistical Mechanics of Cosmic Rays," *Physica A* **331**, 173–181 (2004).

90. E. M. F. Curado and C. Tsallis, "Generalized statistical mechanics: connection with thermodynamics," *J. Phys. A: Math. Gen.* **24**, L69–L72 (1991).

91. G. Wilk and Z. Włodarczyk, "Power Laws in Elementary and Heavy-Ion Collisions," *Phys. Rev. Lett.* **84**, 2770–2773 (2000).

92. R. Penrose, "Gravitational Collapse and Space-Time Singularities," *Phys. Rev. Lett.* **14**, 57–59 (1965).

93. S. W. standard thermal prediction and R. Penrose, "The Singularities of Gravitational Collapse and Cosmology," *Proc. Roy. Soc. Lond. A* **314**, 529–548 (1970).

94. R. M. Wald, "Gravitational Collapse and Cosmic Censorship," *Living Rev. Relativity* **4**, 6 (2001).

95. L. Herrera and N. O. Santos, "Local Anisotropy in Self-Gravitating Systems," *Phys. Rept.* **286**, 53–130 (1997).

96. J. Bardeen, "Non-Singular General-Relativistic Gravitational Collapse," in *Proceedings of the International Conference GR5*, Tbilisi, USSR (1968).

97. I. Dymnikova, "Vacuum Nonsingular Black Hole," *Gen. Rel. Grav.* **24**, 235–242 (1992).

98. E. Ayon-Beato and A. Garcia, "Regular Black Hole in classical metric theory Coupled to Nonlinear Electrodynamics," *Phys. Rev. Lett.* **80**, 5056–5059 (1998).

99. S. Ansoldi, "Spherical Black Holes with Regular Center: A Review of Existing Models Including a Recent Realization with Gaussian Sources," *Springer Proc. Phys.* **170**, 101–123 (2016).

100. P. Nicolini, A. Smailagic, and E. Spallucci, "Noncommutative Geometry Inspired Schwarzschild Black Hole," *Phys. Lett. B* **632**, 547–551 (2006).

101. R. Penrose and R. M. Floyd, "Extraction of Rotational Energy from a Black Hole," *Nature Phys. Sci.* **229**, 177–179 (1971).

102. W. Israel, "Third Law of Black-Hole Dynamics: A Formulation and Proof," *Phys. Rev. Lett.* **57**, 397–399 (1986).

103. S. A. Teukolsky, "The classical rotating solution Metric," *Class. Quant. Grav.* **32**, 124006 (2015).

104. A. C. Fabian *et al.*, "Broad Iron Lines in Active Galactic Nuclei," *Mon. Not. Roy. Astron. Soc.* **238**, 729–736 (1989).

105. A. Brenneman, "Measuring the Angular Momentum of Supermassive Black Holes," *Living Rev. Relativity* **16**, 3 (2013).

106. K. S. Thorne, R. H. Price, and D. A. Macdonald, "Black Holes: The Membrane Paradigm," *Yale University Press* (1986).

107. R. H. Price and K. S. Thorne, "Membrane viewpoint on black holes: Properties and evolution of the stretched horizon," *Phys. Rev. D* **33**, 915–941 (1986).

108. T. Damour, "Surface effects in black hole physics," *Proceedings of the Second Marcel Grossmann Meeting*, North-Holland (1982).

109. M. Parikh and F. Wilczek, "An action for black hole membranes," *Phys. Rev. D* **58**, 064011 (1998).

110. G. Policastro, D. T. Son, and A. O. Starinets, "Shear viscosity of strongly coupled $\mathcal{N} = 4$ supersymmetric Yang–Mills plasma," *Phys. Rev. Lett.* **87**, 081601 (2001).

111. P. Kovtun, D. T. Son, and A. O. Starinets, "Viscosity in strongly interacting field-theoretic theories from black hole physics," *Phys. Rev. Lett.* **94**, 111601 (2005).

112. J. D. area-law entropy, "Black holes and entropy," *Phys. Rev. D* **7**, 2333–2346 (1973).

113. S. W. standard thermal prediction, "Particle creation by black holes," *Commun. Math. Phys.* **43**, 199–220 (1975).

114. R. M. Wald, "The thermodynamics of black holes," *Living Rev. Relativity* **4**, 6 (2001).

115. C. Tsallis, "Possible generalization of Boltzmann–Gibbs statistics," *J. Stat. Phys.* **52**, 479–487 (1988).

116. C. Beck and E. G. D. Cohen, "Superstatistics," *Physica A* **322**, 267–275 (2003).

117. C. Beck, "Dynamical foundations of nonextensive statistical mechanics," *Phys. Rev. Lett.* **87**, 180601 (2001).

118. S. Carlip, "Black hole thermodynamics," *Int. J. Mod. Phys. D* **23**, 1430023 (2014).

119. R. Penrose, "Gravitational collapse: The role of classical metric theory," *Riv. Nuovo Cim.* **1**, 252–276 (1969).

120. R. Penrose and R. M. Floyd, "Extraction of rotational energy from a black hole," *Nature Phys. Sci.* **229**, 177–179 (1971).

121. J. M. Bardeen, W. H. Press, and S. A. Teukolsky, "Rotating black holes: Locally nonrotating frames, energy extraction, and scalar synchrotron radiation," *Astrophys. J.* **178**, 347–370 (1972).

122. Y. B. Zel'dovich, "Generation of waves by a rotating body," *JETP Lett.* **14**, 180–181 (1971).

123. W. H. Press and S. A. Teukolsky, "Floating orbits, superradiant scattering and the black-hole bomb," *Nature* **238**, 211–212 (1972).

124. S. A. Teukolsky, "Perturbations of a rotating black hole. I. Fundamental equations for gravitational, electromagnetic, and neutrino-field perturbations," *Astrophys. J.* **185**, 635–647 (1973).

125. K. D. Kokkotas and B. G. Schmidt, "Quasi-normal modes of stars and black holes," *Living Rev. Relativity* **2**, 2 (1999).

126. E. Berti, V. Cardoso, and A. O. Starinets, "Quasinormal modes of black holes and black branes," *Class. Quant. Grav.* **26**, 163001 (2009).

127. T. Damour, "Surface effects in black hole physics," *Proceedings of the Second Marcel Grossmann Meeting*, North-Holland, Amsterdam (1982).

128. K. S. Thorne, R. H. Price, and D. A. Macdonald, *Black Holes: The Membrane Paradigm*, Yale University Press, New Haven (1986).

129. S. Chatrchyan *et al.* (CMS Collaboration), "Observation of long-range, near-side angular correlations in proton–proton collisions at the LHC," *JHEP* **09**, 091 (2010).

130. B. Abelev *et al.* (ALICE Collaboration), "Long-range angular correlations on the near and away side in p–Pb collisions at $\sqrt{s_{NN}} = 5.02$ TeV," *Phys. Lett. B* **719**, 29–41 (2013).

131. S. Acharya *et al.* (ALICE Collaboration), "Anisotropic flow in small collision systems at the LHC," *Phys. Rev. C* **96**, 034904 (2017).

132. V. Khachatryan *et al.* (CMS Collaboration), "Evidence for collective multiparticle correlations in p–Pb collisions," *Phys. Rev. Lett.* **115**, 012301 (2015).

133. R. M. Fernandes, A. V. Chubukov, and J. Schmalian, "What drives nematic order in iron-based superconductors?" *Nature Phys.* **10**, 97–104 (2014).

134. I. R. Fisher, L. Degiorgi, and Z. X. Shen, "In-plane electronic anisotropy of underdoped '122' Fe-arsenide superconductors revealed by measurements of detwinned single crystals," *Rep. Prog. Phys.* **74**, 124506 (2011).

135. J.-H. Chu, J. G. Analytis, K. De Greve, P. L. McMahon, Z. Islam, Y. Yamamoto, and I. R. Fisher, "In-plane resistivity anisotropy in an underdoped iron arsenide superconductor," *Science* **329**, 824–826 (2010).

136. R. Penrose, "Gravitational Collapse: The Role of classical metric theory," *Riv. Nuovo Cim.* **1**, 252–276 (1969).

137. R. Penrose, "Extraction of Rotational Energy from a Black Hole," *Nature* **229**, 177–179 (1971).

138. T. Damour, "Black Hole Eddy Currents," *Phys. Rev. D* **18**, 3598–3604 (1978).

139. K. S. Thorne, R. H. Price, and D. A. Macdonald (eds.), *Black Holes: The Membrane Paradigm*, Yale University Press, New Haven (1986).

140. W. H. Press, "Long Wave Trains of Gravitational Waves from a Vibrating Black Hole," *Astrophys. J.* **170**, L105–L108 (1971).

141. E. Berti, V. Cardoso, and A. O. Starinets, "Quasinormal Modes of Black Holes and Black Branes," *Class. Quant. Grav.* **26**, 163001 (2009).

142. S. A. Hartnoll, A. Lucas, and S. Sachdev, *Holographic Quantum Matter*, MIT Press, Cambridge (2018).

143. J. Y. Ollitrault, "Anisotropy as a Signature of Transverse Collective Flow," *Phys. Rev. D* **46**, 229–245 (1992).

144. S. Chatrchyan *et al.* (CMS Collaboration), "Observation of Long-Range Near-Side Angular Correlations in Proton–Proton Collisions," *JHEP* **1009**, 091 (2010).

145. B. Abelev *et al.* (ALICE Collaboration), "Long-Range Angular Correlations on the Near and Away Side in p–Pb Collisions," *Phys. Lett. B* **719**, 29–41 (2013).

146. C. Tsallis, "Possible Generalization of Boltzmann–Gibbs Statistics," *J. Stat. Phys.* **52**, 479–487 (1988).

147. C. Beck and E. G. D. Cohen, "Superstatistics," *Physica A* **322**, 267–275 (2003).

148. J. Cleymans and D. Worku, "Relativistic Thermodynamics: Transverse Momentum Distributions in High-Energy Physics," *Eur. Phys. J. A* **48**, 160 (2012).

149. E. Berti, V. Cardoso and A. O. Starinets, "Quasinormal modes of black holes and black branes," *Class. Quant. Grav.* **26**, 163001 (2009).

150. H. Yang, A. Zimmerman, A. Zenginoglu, F. Zhang, E. Berti and Y. Chen, "Quasinormal-mode spectrum of classical rotating solution black holes and its geometric interpretation," *Phys. Rev. D* **88**, 044047 (2013).

151. R. H. Price, "Nonspherical perturbations of relativistic gravitational collapse. I. Scalar and gravitational perturbations," *Phys. Rev. D* **5**, 2419–2438 (1972).

152. J. Cleymans and D. Worku, "The Tsallis distribution in proton–proton collisions at $\sqrt{s} = 0.9$ TeV at the LHC," *J. Phys. G* **39**, 025006 (2012).

153. B. Abelev *et al.* [ALICE Collaboration], "Multiplicity dependence of pion, kaon, proton and lambda production in p–Pb collisions at $\sqrt{s_{NN}} = 5.02$ TeV," *Phys. Lett. B* **728**, 25–38 (2014).

154. J. Adam *et al.* [ALICE Collaboration], "Centrality dependence of particle production in p–Pb collisions at $\sqrt{s_{NN}} = 5.02$ TeV," *Phys. Rev. C* **91**, 064905 (2015).

155. V. Khachatryan *et al.* [CMS Collaboration], "Evidence for collective multiparticle correlations in p–Pb collisions," *Phys. Rev. Lett.* **115**, 012301 (2015).

156. A. Adare *et al.* [PHENIX Collaboration], "Measurements of higher-order flow harmonics in Au+Au collisions at $\sqrt{s_{NN}} = 200$ GeV," *Phys. Rev. Lett.* **107**, 252301 (2011).

157. C. Tsallis, *Introduction to Nonextensive Statistical Mechanics: Approaching a Complex World* (Springer, New York, 2009), doi:10.1007/978-0-387-85359-8.

158. R. Penrose, "Gravitational collapse: The role of classical metric theory," *Riv. Nuovo Cim.* **1**, 252–276 (1969).

159. Ya. B. Zel'dovich, "Amplification of cylindrical electromagnetic waves reflected from a rotating body," *Sov. Phys. JETP* **35**, 1085–1087 (1972).

160. W. H. Press and S. A. Teukolsky, "Floating orbits, superradiant scattering and the black-hole bomb," *Nature* **238**, 211–212 (1972).

161. E. Berti, V. Cardoso, and A. O. Starinets, "Quasinormal modes of black holes and black branes," *Class. Quant. Grav.* **26**, 163001 (2009).

162. E. Berti, V. Cardoso, and A. O. Starinets, "Quasinormal modes of black holes and black branes," *Class. Quant. Grav.* **26**, 163001 (2009).

163. K. D. Kokkotas and B. G. Schmidt, "Quasi-normal modes of stars and black holes," *Living Rev. Relativity* **2**, 2 (1999).

164. R. Penrose, "Gravitational collapse: the role of classical metric theory," *Riv. Nuovo Cim.* **1**, 252–276 (1969).

165. J. Barbour, B. Z. Foster, and N. Ó Murchadha, "Relativity without relativity," *Class. Quant. Grav.* **19**, 3217–3248 (2002).

166. V. Cardoso, O. J. C. Dias, G. S. Hartnett, M. Middleton, and J. E. Santos, "Holographic correspondence and the black hole ringdown," *JHEP* **04**, 183 (2014).

167. L. Onsager, "Reciprocal relations in irreversible processes. I," *Phys. Rev.* **37**, 405–426 (1931).

168. S. Hod, "Slow relaxation of rapidly rotating black holes," *Phys. Rev. D* **78**, 084035 (2008).

169. ALICE Collaboration, "Universal features of particle production in pp, p–Pb and Pb–Pb collisions," *Phys. Lett. B* **727**, 371–380 (2013).

170. B. P. Abbott *et al.* (LIGO Scientific and Virgo Collaborations), "Tests of classical metric theory with GW150914," *Phys. Rev. Lett.* **116**, 221101 (2016).

171. R. Brito, V. Cardoso, and P. Pani, "Superradiance," *Lect. Notes Phys.* **906** (Springer, 2015).

172. CMS Collaboration, "Evidence for collectivity in pp collisions at the LHC," *Phys. Lett. B* **765**, 193–220 (2017).

173. E. Mach, *The Science of Mechanics*, (Open Court, Chicago, 1893).

174. J. A. Wheeler, "Mach's principle as boundary condition for historical metric formulation's equations," in *Gravitation and Relativity*, ed. H.-Y. Chiu and W. Hoffmann (Benjamin, 1964).

175. L. D. Landau and E. M. Lifshitz, *Mechanics*, 3rd ed., Course of Theoretical Physics Vol. 1 (Pergamon Press, 1976).

176. H. Haken, *Synergetics: An Introduction*, (Springer, 1983).

177. L. D. Landau and E. M. Lifshitz, *Fluid Mechanics*, 2nd ed., Course of Theoretical Physics Vol. 6 (Pergamon Press, 1987).

178. I. Newton, *Philosophiæ Naturalis Principia Mathematica*, (London, 1687).

179. J. D. Jackson, *Classical Electrodynamics*, 3rd ed. (Wiley, 1998).

180. M. Milgrom, "A modification of the Newtonian dynamics as a possible alternative to the hidden mass hypothesis," *Astrophys. J.* **270**, 365–370 (1983).

181. C. M. Will, "The confrontation between classical metric theory and experiment," *Living Rev. Relativity* **17**, 4 (2014).

182. CMS Collaboration, "Observation of long-range near-side angular correlations in proton–proton collisions," *JHEP* **09**, 091 (2010).

183. A. Coniglio and M. Klein, "Clusters and Ising critical droplets," *J. Phys. A* **13**, 2775–2780 (1980).

184. N. N. Bogoliubov and D. V. Shirkov, *Introduction to the Theory of Quantized Fields*, (Wiley–Interscience, 1980).

185. R. Metzler and J. Klafter, "The random walk's guide to anomalous diffusion," *Phys. Rep.* **339**, 1–77 (2000).

186. G. Aad *et al.* (ATLAS Collaboration), "Measurement of long-range pseudorapidity correlations and azimuthal harmonics," *Phys. Rev. C* **90**, 044906 (2014).

187. P. W. Anderson, "More is different," *Science* **177**, 393–396 (1972).

188. S. S. McGaugh, F. Lelli, and J. M. Schombert, "Radial Acceleration Relation in Rotationally Supported Galaxies," *Phys. Rev. Lett.* **117**, 201101 (2016).

189. F. Lelli, S. S. McGaugh, and J. M. Schombert, "SPARC: Mass Models for 175 Disk Galaxies with Spitzer Photometry and Accurate Rotation Curves," *Astron. J.* **152**, 157 (2016).

190. J. M. Bardeen, W. H. Press, and S. A. Teukolsky, "Rotating Black Holes: Locally Nonrotating Frames, Energy Extraction, and Scalar Synchrotron Radiation," *Astrophys. J.* **178**, 347–370 (1972).

191. M. Milgrom, "A Modification of the Newtonian Dynamics as a Possible Alternative to the Hidden Mass Hypothesis," *Astrophys. J.* **270**, 365–370 (1983).

192. J. F. Navarro, C. S. Frenk, and S. D. M. White, "The Structure of Cold Dark Matter Halos," *Astrophys. J.* **462**, 563–575 (1996).

193. B. P. Abbott *et al.* (LIGO Scientific Collaboration and Virgo Collaboration), "Observation of Gravitational Waves from a Binary Black Hole Merger," *Phys. Rev. Lett.* **116**, 061102 (2016).

194. K. Aamodt *et al.* (ALICE Collaboration), "Elliptic flow of charged particles in Pb–Pb collisions at $\sqrt{s_{NN}} = 2.76$ TeV," *Phys. Rev. Lett.* **105**, 252302 (2010).

195. C. C. Lin and F. H. Shu, "On the Spiral Structure of Disk Galaxies," *Astrophys. J.* **140**, 646–655 (1964).

196. B. Bertin and C. C. Lin, *Spiral Structure in Galaxies: A Density Wave Theory* (MIT Press, Cambridge, 1996).

197. M. J. Genzel *et al.*, "Strongly baryon-dominated disk galaxies at the peak of galaxy formation ten billion years ago," *Nature* **543**, 397–401 (2017).

198. Ya. B. Zel'dovich, "Generation of Waves by a Rotating Body," *JETP Lett.* **14**, 180–181 (1971).

199. W. H. Press and S. A. Teukolsky, "Floating Orbits, Superradiant Scattering and the Black-hole Bomb," *Nature* **238**, 211–212 (1972).

200. E. Berti, V. Cardoso, and A. O. Starinets, "Quasinormal modes of black holes and black branes," *Class. Quant. Grav.* **26**, 163001 (2009).

201. R. Brito, V. Cardoso, and P. Pani, *Superradiance: New Frontiers in Black Hole Physics* (Springer, Cham, 2015).

202. A. V. Oppenheim and R. W. Schafer, *Discrete-Time Signal Processing* (Prentice Hall, 3rd ed., 2009).

203. M. B. Priestley, *Spectral Analysis and Time Series* (Academic Press, 1981).

204. R. N. Bracewell, *The Fourier Transform and Its Applications* (McGraw–Hill, 3rd ed., 2000).

205. P. Stoica and R. L. Moses, *Spectral Analysis of Signals* (Prentice Hall, 2005).

206. C. A. Grant, "Time Symmetry as a Trap: Noether-Free Time Void Theorem and Refinement-Induced Decoherence," (Manuscript / internal note, 2026).

207. A. N. Kolmogorov, *Grundbegriffe der Wahrscheinlichkeitsrechnung* (Springer, Berlin, 1933).

208. C. Tsallis, *Introduction to Nonextensive Statistical Mechanics: Approaching a Complex World*, 2nd ed. (Springer, 2023).

209. S. Umarov and C. Tsallis, *Mathematical Foundations of Nonextensive Statistical Mechanics* (World Scientific, 2022).

210. C. Tsallis, "Non-additive entropies and statistical mechanics at the edge of chaos," *Philos. Trans. R. Soc. A* **381**, 20220293 (2023).

A. Observational Replacement of General Relativity by Chronoscalar Field Theory

This appendix enumerates the foundational structures of General Relativity (GR) and states explicitly how each is replaced—not approximated—by Chronoscalar Field Theory (CFT). Where observational agreement exists, it is shown to arise from projection of a deeper ordering geometry rather than from spacetime curvature or force mediation.

A. Spacetime Curvature

GR: Gravity is spacetime curvature sourced by stress–energy.

CFT: Spacetime is secondary. The primary geometric structure is the asymmetric ordering field $T(x^\mu)$. Apparent curvature phenomena arise from admissibility constraints imposed by longitudinal standing registries and transverse Hessian activation.

Observational hooks: Planetary ephemerides, light deflection, and redshift are reproduced as weak-registry averages of ∇T geometry, without invoking metric curvature as a causal agent.

B. Geodesic Motion

GR: Free particles follow metric geodesics.

CFT: Particles follow admissible histories minimizing ordering cost. Apparent geodesic motion is a projection of longitudinal corridor alignment.

Observational hooks: Free-fall universality and inertial motion arise from global registry coherence rather than from extremal proper time.

C. Newtonian Potential and Dark Matter

GR: Weak-field gravity reduces to a scalar potential requiring dark matter halos to fit galactic data.

CFT: No gravitational potential exists. Flat rotation curves and lensing arise from standing longitudinal registry and Hessian-flip activation of transverse admissibility.

Observational hooks: Flat rotation curves, baryon–lensing mismatch, filamentary weak-lensing maps, and MOND-like scaling relations emerge without additional mass components.

D. Gravitational Lensing

GR: Light bends due to spacetime curvature sourced by mass.

CFT: Lensing is refraction of admissible null trajectories under transverse gradients and curvature of T.

Observational hooks: Einstein radii map to admissibility-gradient scales; shear maps trace Hessian structure of T, explaining over-lensing in clusters and filament lensing without dark matter.

E. Time Dilation

GR: Time dilation arises from velocity or gravitational potential.

CFT: Time dilation is throttling of admissible phase accumulation due to ordering density and curvature.

Observational hooks: Gravitational redshift, GPS clock offsets, and Shapiro delay arise from longitudinal registry loading rather than spacetime curvature.

F. Horizons and Singularities

GR: Horizons are causal boundaries enclosing singular interiors.

CFT: Horizons are ordering saturation surfaces. Transverse admissibility channels close while longitudinal registry dominates. Singularities are forbidden.

Observational hooks: Finite tidal signatures, regular core behavior, and horizon thermodynamics arise without divergent curvature invariants.

G. Black Hole Spin

GR: Extremal Kerr states are kinematically allowed.

CFT: Sub–extremal spin is enforced internally by Hessian-flip dissipation of azimuthal shear.

Observational hooks: Observed astrophysical spin bounds follow from intrinsic ordering resistance rather than accretion or radiative fine-tuning.

H. Gravitational Radiation

GR: Gravity propagates as transverse metric waves.

CFT: Longitudinal gravity does not radiate. Observed signals correspond to transverse ordering readout during rapid corridor reconfiguration.

Observational hooks: Detected waveforms encode anisotropic dissipation and ordering realignment, not propagation of the gravitational interaction itself.

I. Mass and Inertia

GR: Mass sources curvature and inertia is intrinsic.

CFT: Mass is the entropy cost of maintaining a standing longitudinal registry. Inertia and gravity share the same ordering origin.

Observational hooks: Machian correlations, inertia dependence on global structure, and consistency of local mass across environments follow naturally.

J. Brownian Motion and Statistics

GR/QFT background: Brownian motion is Gaussian and force-driven.

CFT: Brownian motion probes ordering geometry directly. Non-Gaussian, q-exponential statistics arise from admissible corridor partitioning.

Observational hooks: Measured heavy-tailed diffusion, anomalous transport, and early deviation from Gaussian errors are fundamental, not corrections.

K. Summary

General Relativity successfully parameterizes averaged observational readouts but employs incorrect primitives: curvature, force, and mass sourcing. Chronoscalar Field Theory replaces these with ordering, admissibility, and entropy cost. Where observations coincide, they do so because both theories describe the same projections—not because their foundations align.

Gravity is not curvature. It is a standing longitudinal wave transmitted through a global admissibility corridor.

Appendix B: Quantum Field Theory Mop–Up and Chronoscalar Replacement

This appendix enumerates the foundational parameters and structural assumptions of conventional Quantum Field Theory (QFT) and identifies their replacements within Chronoscalar Field Theory (CFT). Each item isolates what QFT inserts, what it patches, why it is non–fundamental, and how CFT resolves the same observations using a single ordering geometry.

1. Gauge Couplings **QFT object:** g_1, g_2, g_3 associated with $\mathrm{U}(1)$, $\mathrm{SU}(2)$, and $\mathrm{SU}(3)$.

What they patch: Interaction strength has no geometric origin and must be inserted, then repaired through running.

Why non–fundamental: Multiple unrelated couplings that drift with scale indicate response fitting, not structure.

CFT replacement: Ordering response functions: rank–1 longitudinal registry, rank–3 transverse readout, and corridor variance controlling intermittency.

Observational hook: Same ordering variance appears as Tsallis $q > 1$ tails, persistent azimuthal flow, and galactic standing–wave coherence.

2. Higgs Field and Symmetry Breaking **QFT object:** Scalar Higgs field with (μ^2, λ) potential and vacuum expectation value.

What it patches: Gauge invariance forbids mass; Higgs restores algebraic consistency.

Why non–fundamental: Explains how mass is inserted, not why persistence costs inertia.

CFT replacement: Mass is the entropy cost of longitudinal registry and resistance to transverse isotropization. No symmetry breaking required.

Observational hook: Mass correlates with dissipation thresholds, collapse regulation, and horizon behavior.

3. Yukawa Couplings **QFT object:** Nine independent Yukawa parameters.

What they patch: Flavor mass hierarchy.

Why non–fundamental: Multiple free mass knobs indicate calibrated ignorance.

CFT replacement: Flavor families correspond to distinct admissibility corridor classes. Yukawas are projections of ordering curvature onto internal modes.

Observational hook: Mass hierarchy must correlate with non–Gaussian transport signatures.

4. CKM / PMNS Mixing and CP Phase **QFT object:** Unitary mixing matrices and complex phase.

What they patch: Mixing and CP violation lack geometric origin.

Why non–fundamental: CP treated as bookkeeping rather than physical asymmetry.

CFT replacement: CP is an ordering pseudoscalar arising from non–integrable transverse phase. Mixing arises from corridor phase interference.

Observational hook: Same pseudoscalar invariants appear in geology, heavy ions, and astrophysical alignment.

5. Strong CP Parameter **QFT object:** θ_{QCD}.

What it patches: Nothing; it exposes incompleteness.

Why non–fundamental: A parameter allowed but observed to be nearly zero signals missing structure.

CFT replacement: Large CP drift is inadmissible under ordering geometry and suppressed by corridor constraints.

Observational hook: Absence of macroscopic CP drift across unrelated systems.

6. Neutrino Masses and Oscillations **QFT object:** Additional masses and mixing angles.

What they patch: Original Standard Model forbids neutrino mass.

Why non–fundamental: Parameter expansion where reduction should occur.

CFT replacement: Neutrinos are long–baseline ordering phase carriers. Oscillations arise from corridor–dependent phase transport.

Observational hook: Baseline anomalies correlate with ordering geometry rather than new particles.

7. Dark Matter **QFT object:** Non–luminous mass halos.

What it patches: Rotation curves, lensing, and structure formation under force–only gravity.

Why non–fundamental: Matter proxy for missing geometry.

CFT replacement: Standing longitudinal registry and transverse readout after Hessian flip.

Observational hook: Lensing and rotation follow filamentary geometry, not baryons.

8. Dark Energy / Cosmological Constant **QFT object:** Uniform acceleration term Λ.

What it patches: Failure of mass–curvature gravity on cosmic scales.

Why non–fundamental: A constant push is not an ordering principle.

CFT replacement: Apparent acceleration arises from global admissibility bias evolution.

Observational hook: Acceleration aligns with anisotropic large–scale structure.

9. Time as Passive Parameter **QFT assumption:** Time–reversal symmetric microphysics; arrow is emergent.

Why wrong: Persistence cannot emerge without prior ordering.

CFT replacement: Time is a physical asymmetric ordering field $T(x^\mu)$.

Observational hook: Non–Gaussianity at Brownian floor, long–range coherence, harmonic locking.

10. Fixed Spacetime Dimension **QFT assumption:** Rigid $3+1$ dimensional stage.

Why wrong: Effective dimension depends on admissible support, not coordinates.

CFT replacement: Rank–1 longitudinal storage and rank–3 transverse readout.

Observational hook: Same rank decomposition recurs from diffusion to horizons.

11. Multiple Fundamental Gauges **QFT assumption:** Several independent gauge symmetries are fundamental.

Why wrong: Gauge redundancy compensates for wrong variables.

CFT replacement: Single ordering connection; gauge freedom reflects transverse projection choice.

Observational hook: Universality of anisotropic transport across physical scales.

Quantum Field Theory Mop–Up and Chronoscalar Replacement

This appendix enumerates the principal foundational parameters and assumptions of conventional Quantum Field Theory (QFT) and identifies their replacements within Chronoscalar Field Theory (CFT). Each entry follows the same structure: (i) the QFT object, (ii) what it patches, (iii) why it is non–fundamental, and (iv) the corresponding CFT primitive with observational hooks.

Items 1–11 appear in the main text. We complete the mapping with Items 12–15.

12. Renormalization Scale and Cutoff Dependence **QFT object:** Renormalization scale μ, ultraviolet cutoffs, running couplings.

What it patches: Divergent amplitudes arising from treating fluctuations as unweighted, isotropic, and scale–free.

Why non–fundamental: A theory whose predictions depend on an arbitrary scale introduced by hand is not encoding structure; it is compensating for a missing measure over histories.

CFT replacement: Admissibility–weighted path measure determined by the chronoscalar geometry. Divergences are suppressed by corridor geometry and ordering curvature before any continuum limit is taken. No external cutoff is required; suppression is geometric.

Observational hook: Universality of heavy–tail exponents and finite transport coefficients across systems with vastly different microscopic scales.

13. Vacuum Energy and the Cosmological Constant Catastrophe **QFT object:** Zero–point energy of quantum fields, formally divergent vacuum energy density.

What it patches: Identification of the vacuum with an unstructured, energy–filled background.

Why non–fundamental: Assigning energy to unadmitted fluctuations conflates kinematic bookkeeping with physical support. The resulting discrepancy of $\sim 10^{120}$ is not a coincidence but a signal that the vacuum concept is wrong.

CFT replacement: The vacuum is an admissibility minimum, not an energy reservoir. Only histories that satisfy ordering constraints contribute physically. Unadmitted fluctuations do not gravitate because they do not persist.

Observational hook: Absence of catastrophic vacuum gravitation; cosmic acceleration tracks large–scale ordering evolution rather than zero–point energy.

14. Measurement Postulate and the Born Rule **QFT object:** Wavefunction collapse, probabilistic measurement axiom, Born rule.

What it patches: Inability of unitary time–symmetric evolution to explain definite outcomes.

Why non–fundamental: Probability is introduced axiomatically because admissibility of histories is not modeled. Collapse is a bookkeeping rule, not a physical process.

CFT replacement: Measurement corresponds to admissibility selection. Observed outcomes are those trajectories that remain phase–coherent under the ordering field. Probabilities arise from corridor weights, not collapse.

Observational hook: Systematic deviation from Gaussian statistics and emergence of q–exponential distributions at the Brownian floor.

15. Quantum Gravity as a Separate Sector QFT assumption: Gravity must be quantized as another force or mediator.

What it patches: Incompatibility between force–based quantum fields and geometric gravity.

Why non–fundamental: The conflict arises because time is passive in QFT. Quantizing curvature treats a readout as a source.

CFT replacement: Gravity is not a force but the macroscopic manifestation of a coherent longitudinal potential oscillation in the chronoscalar ordering field. The graviton functions as an informational mediator, carrying phase and admissibility coherence, while transverse excitations encode orientation rather than force transmission.

Observational hook: Flat rotation curves, coherent lensing, collapse regulation, and sub–extremal spin bounds arise without new particles or quantization of spacetime.

Taken together, Items 1–15 show that QFT's free parameters, gauge structure, and vacuum pathologies are not fundamental features of nature but compensations for a missing ordering principle. Chronoscalar Field Theory replaces parameter proliferation with a single asymmetric ordering field whose geometry governs admissibility, persistence, and macroscopic structure across all scales.

.1. Chronoscalar Brownian Motion and the Emergence of Tsallis Statistics

This appendix derives non–Gaussian (Tsallis) statistics directly from chronoscalar ordering geometry, without invoking molecular chaos, temperature fluctuations, or phenomenological entropy deformation. The result is not an alternative statistical assumption but the *inevitable consequence* of diffusion on an admissibility–filtered manifold.

C.1 Brownian Motion as the Minimal Probe of Ordering Geometry

Brownian motion is the minimal physical process in which irreversible evolution appears without macroscopic structure, long–range forces, or coherent flow. It therefore provides the cleanest environment in which to isolate the effect of the chronoscalar ordering field $T(x^\mu)$.

In CFT, Brownian motion does not occur in an isotropic phase space. Even in the absence of external forces, admissible trajectories are geometrically filtered by the asymmetric ordering field. This filtering acts *before* any coarse–graining or ensemble averaging is performed.

Let $x^i(t)$ denote the position of a tracer particle. The admissible velocity increments are weighted by the chronoscalar admissibility functional

$$\mathcal{A}[\gamma] = \exp\!\left(- \int_\gamma \mathcal{L}_{\mathrm{adm}}\big(\nabla T, H_T, u^\mu\big)\, ds \right), \tag{131}$$

where $H_T = \nabla_\mu \nabla_\nu T$ is the chronoscalar Hessian. Even when forces vanish, $\mathcal{A}$ is not uniform across histories.

C.2 Anisotropic Langevin Dynamics from Admissibility

At mesoscopic resolution, admissibility filtering induces an anisotropic Langevin equation

$$m\dot{v}_i = -\Gamma_{ij}(T)\, v_j + \xi_i(t), \tag{132}$$

where the friction tensor decomposes as

$$\Gamma_{ij} = \gamma_\perp \delta_{ij} + (\gamma_\parallel - \gamma_\perp)\, n_i n_j, \qquad n_i \propto \partial_i T. \tag{133}$$

This anisotropy is not imposed phenomenologically. It arises because longitudinal motion aligned with ∇T accumulates ordering phase coherently, while transverse motion probes regions of higher admissibility cost.

C.3 Failure of Gaussian Noise Under Corridor Partitioning

In standard Brownian theory, the stochastic force $\xi_i(t)$ is assumed Gaussian due to isotropic sampling of microstates. This assumption fails in CFT because admissible microhistories are *not equally weighted*.

Instead, the noise correlator is conditioned on an ordering weight β_T,

$$\langle \xi_i(t)\xi_j(t')\rangle_{\beta_T} = 2\,\Gamma_{ij}\,\beta_T^{-1}\,\delta(t-t'), \tag{134}$$

where β_T is conjugate to dissipation under the admissibility functional. Crucially, β_T fluctuates across corridors because H_T varies spatially and directionally.

Thus the ensemble is not governed by a single diffusion constant, but by a distribution $f_T(\beta)$ determined by ordering curvature.

C.4 Corridor Averaging and the Deformed Fokker–Planck Equation

The correct kinetic description is therefore obtained by averaging over admissible corridors:

$$\partial_t P(v,t) = \int d\beta\, f_T(\beta)\, \partial_i \left[\Gamma_{ij} \left(v_j P + \beta^{-1} \partial_j P \right) \right]. \tag{135}$$

This equation differs from the standard Fokker–Planck equation only in the measure over β. No new dynamics, forces, or interactions are introduced.

For the generic case in which admissibility cost is quadratic in velocity and curvature, $f_T(\beta)$ is a gamma distribution. This form is fixed by geometry, not by thermodynamics.

C.5 Emergence of Tsallis Statistics

Solving for the stationary distribution yields

$$P(v) \propto \left[1 + (q-1)\, \frac{m v^2}{2 T_{\text{eff}}} \right]^{-1/(q-1)}, \tag{136}$$

with

$$q - 1 = \frac{\mathrm{Var}(\beta_T)}{\langle \beta_T \rangle^2}. \tag{137}$$

The Tsallis index q is therefore *not* an entropy deformation parameter. It is a dimensionless geometric observable measuring the variance of admissible ordering weights. Gaussian statistics are recovered only in the degenerate limit $\mathrm{Var}(\beta_T) \to 0$, corresponding to unresolved ordering curvature.

C.6 Physical Interpretation

Gaussian statistics are not the signature of "no structure." They are the signature of *unresolved structure*. The moment ordering curvature becomes experimentally resolvable, the admissible measure ceases to be uniform and the distribution departs from Gaussian form.

Brownian motion therefore does not generate Tsallis statistics; it reveals them. The same ordering geometry that produces heavy tails at micron scales reappears as anisotropic transport, nematic flow, standing–wave locking, and horizon dissipation at larger scales.

C.7 Summary

Non–Gaussian statistics are the earliest measurable imprint of chronoscalar ordering. They do not arise from interactions, temperature fluctuations, or finite statistics. They arise because motion occurs on a directed admissibility manifold.

Tsallis statistics are therefore not an alternative to Gaussian statistics. They are the correct statistics of motion in time.